

In-silicA Protein Engineering: Tuning the Properties of Natural Enzymes

Inauguraldissertation

zur

Erlangung der Würde eines Doktors der Philosophie

vorgelegt der

Philosophisch-Naturwissenschaftlichen Fakultät

der Universität Basel

von

Carolina Ilenia Giunta

Basel, 2021

Originaldokument gespeichert auf dem Dokumentenserver der Universität Basel

<https://edoc.unibas.ch>

Genehmigt von der Philosophisch-Naturwissenschaftlichen Fakultät

auf Antrag von

Prof. Dr. Patrick Shahgaldian

Prof. Dr. Thomas R. Ward

Prof. Dr. Peter Walde

Basel, 17 November 2020

The Dean of Faculty
Prof. Dr. Martin Spiess

A me

Per non essermi mai arresa

ACKNOWLEDGEMENTS

Long term and intensive research studies, as demonstrated from my PhD project involved the priceless contribution and the support of a long list of people. I sincerely acknowledge all of them.

My special thanks go to Prof. Patrick Shahgaldian. Beside carefully supervising my PhD project, he has been an excellent coach in the past four years. With patience and always high motivation he guided me through this unique life experience. It has been a pleasure to learn from him and to be part of his research group.

I would like to extend my acknowledgements to my doctor father at the University of Basel, Prof. Thomas Ward for his support, trust, and the freedom he allowed me. I'm thankful to Prof. Peter Walde for allowing me to share with him my last experimental findings. I thank my doctoral committee for reading and revising my thesis manuscript.

Thanks to Prof. Oliver Wenger and Dr. Christoph Kerzig for granting me the use of their laser. Without their support a part of the main findings of this thesis would not have been possible.

I'm thankful to Prof. Manuel Ferrer and to his research group, at the CSIC Madrid, and to Prof. Philippe Corvini for the extremely motivating scientific collaboration which was established in those years.

I would like to thank Ana Bela for her support, advises, for revising a part of this manuscript, and Riccardo (Richi) for visiting me from time to time in my office during the writing of my thesis manuscript, to make sure that I was doing fine. I thank them both for being great friends to me.

Of course, my thanks go to Shahgaldian group. Here I have to distinguish between the super (super) old Shahgaldian group including Alessandro and Negar, the old Shahgaldian group

including Mina, Moha and Sabine, and finally the new Shahgaldian group including Manon, Jenny, Magda, Amir, Congyu and Tala. Additionally, a special thanks goes to INOFEA and PERSEO including Rita who made me feel at home when I joined the group and helped me doing my first steps in our lab, and Federica who was essential for achieving any of my successes. I thank Emilie for her “Caro you can do it!” and Lars and Anna with who I shared interesting scientific discussions and nice moments (e.g. desserts prepared by Anna). I had the pleasure to meet all of them and I consider you all friends, more than colleagues. Shahgaldian group has changed a lot in the last years, however this research group, my group, was always centred on the asset that *people support each other*. My colleagues/ friends allowed me to share my frustration along with my happiness, revised this manuscript and were on my side all the time. This manuscript contains a part of all of you, therefore I would like to say Grazie, Merci, Danke, 谢谢, Dziękuję, ممنون, Tack, شكرًا to all of you.

My deep gratitude goes to the Brian family, my second family, for taking care of me, for always listening, for providing solutions to my problems and for their priceless support every day in the past three years.

I am especially thankful to my parents and my two little sisters, Stefy e Luce, for being always my shield. I thank them especially for supporting any choice of my life, also when it was painful for them. All my successes are yours. Grazie per tutto.

Last but not least, I would like to thank Niels for being my “schutzengel” during all this time, for handling my panic attacks and celebrating my successes, and always believing in me. His presence was pivotal for the success of my PhD.

TABLE OF CONTENTS

Abstract.....	1
List of figures.....	3
List of tables.....	9
Abbreviations.....	10
Chapter 1 Introduction.....	11
1 Methods for the modification of enzyme properties.....	12
2 Enzyme immobilization onto solid supports.....	15
Enzyme adsorption.....	17
Covalent immobilization and cross-linking of enzyme.....	19
Enzyme encapsulation.....	23
Surface properties of support materials for enzyme immobilization.....	25
Silica based materials.....	29
3 Modification of the environment of immobilized enzymes.....	32
Interfacial environment.....	33
Enzyme environment inside a 3D network.....	35
Chapter 2 Objectives of the research.....	37
Chapter 3 Tuning the enantioselectivity of natural promiscuous enzymes.....	40
Summary.....	41
1 Enzyme promiscuity.....	42
2 Abstract.....	45
3 Introduction.....	46
4 Results and discussion.....	48
Synthesis and structural study.....	48
Substrate specificity and catalytic turnover study.....	52
Enantioselectivity study.....	56
Solvent stability study.....	59
On the reproducibility of the method.....	60
On the versatility of the method.....	61
5 Conclusions.....	66
Chapter 4 Aurozyme: towards the engineering of artificial cold active nanobiocatalysts.....	70
Summary.....	71

1	Cold active enzymes (CAEs).....	72
2	Gold nano-structures	73
3	Results and discussion.....	77
	Aurozyme design	77
	AuNPs synthesis and characterization	79
	AuNPs electrostatic immobilization and enzyme co-immobilization	82
	AuNPs covalent immobilization	84
	Enzyme bioconjugation with AuNPs-SPs	88
	Shielding of co-immobilized AuNPs-enzyme-SPs with organosilanes.....	89
	Enzymes Activity characterization	94
4	Conclusions	102
	Chapter 5 Conclusions and outlook	103
1	Conclusion.....	104
2	Outlook.....	105
	Chapter 6 Experimental methods.....	107
	Materials Synthesis	108
1	Silica particles Synthesis (SPs)	108
2	Gold Nanoparticles Synthesis (AuNPs)	108
3	Gold Nanoparticles immobilization on SPs	109
4	β -galactosidase and lipase B immobilization on AuNPs-SPs	110
5	AuNPs-CalB-SPs shielding.....	110
	Characterization Methods	112
6	Scanning electron microscopy and particle size measurement	112
7	Cryo-transmission electron microscopy (cryo-TEM)	112
8	Enzyme activity assay and irradiation of Gold Nanoparticles	112
	Chapter 7 Annex	115
	References.....	154

ABSTRACT

Due to their excellent catalytic properties, enzymes are highly efficient tools for performing a wide variety of (bio)chemical transformation. However, the relative fragility of enzymes and their fast aging in non-physiological environments is a major limit for their further implementation in biocatalysis.

The bioconjugation of enzymes to a wide range of materials provides a facile, yet sophisticated strategy for tuning enzyme properties. Specifically, the immobilization of enzymes onto solid supports was proven to be effective in improving the stability of enzymes and in enhancing their catalytic properties. This strategy provides, also, the advantage of producing reusable catalysts, thus increasing the cost-effectiveness of their applications, e.g. in continuous flow processes. The local environment of enzymes greatly affects several of its properties including structure, turnover number, selectivity, specificity, promiscuity, and stability in harsh conditions. Therefore, the rational engineering of the local enzyme environment can be applied for tuning properties of enzymes. A brief state of the art of the methods used for the modification of properties of enzymes, including enzyme immobilization strategies and enzyme environment modification approaches, is provided in the introduction (Chapter 1).

The research carried out in the frame of this doctoral thesis combines the advantages of the enzyme bioconjugation to solid materials with the benefits of tuning the enzyme local environment, using a protein supramolecular engineering approach (Chapter 2). The design of the enzyme environment aimed at the improvement of the enzyme enantioselectivity and at the enhancement of the activity of enzymes at low temperatures and in organic solvent (i.e., acetonitrile).

Specifically, the synthesis of a nanobiocatalyst by shielding an immobilized ester hydrolase within an organosilica material of different compositions, is described (Chapter 3). The composition of the shielding material was modified to locally tune the enzyme nanoenvironment. Employing this method, the substrate promiscuous and not enantioselective ester hydrolase was endowed with enantioselectivity yet, conserving its high promiscuity. Furthermore, this nanobiocatalyst showed remarkably improved solvent stability when submitted to high solvent concentrations (i.e. acetonitrile). The versatility of this approach was proven with three structurally different ester hydrolases.

Furthermore, a novel synthetic method to produce nanobiocatalysts artificially endowed with cryophilic properties, is described (Chapter 4). The nanobiocatalysts, later called Aurozyme, consists of gold nanoparticles (AuNPs) and enzyme molecules co-immobilized onto a silica scaffold and shielded within a nanometer-thin organosilica protective layer. To produce such a hybrid structure, a method allowing the covalent immobilization of AuNPs on the surface of the silica nanoparticles (SPs) was developed and optimized. This method enables reaching a dense and homogeneous AuNPs surface coverage of SPs. After enzyme co-immobilization, a nanometer-thin protective organosilica layer was grown at the surface of the SPs. This layer was designed to fulfill the dual function of protecting the enzyme from the surrounding environment and allowing the confinement, at the nanometer scale, of the heat diffusing from the surface of AuNPs to the enzyme environment after surface plasmon resonance (SPR) activation. To establish a proof of concept, we used a lipase (i.e. lipase B from *Candida Antarctica*) and the β -galactosidase from *Kluyveromyces lactis*; enzymes extensively used in a wide range of industrial applications. We demonstrated a drastic biocatalytic activity improvement at temperatures ranging from 20°C to -10°C.

Keywords: enzyme immobilization, biocatalysis, organosilica, gold nanoparticles, enantioselectivity, promiscuity, cold active enzymes.

LIST OF FIGURES

Figure 1. Protein engineering and artificial metalloenzyme methods. (a) Schematic depiction of the protein engineering process. The protein with desired properties (e.g. enhanced catalytic activity, increased stability in extreme conditions) can be selected among a library of variants and further analyzed. Reproduced with permission from reference 8. Copyright (2019) Elsevier Ltd.; (b) the complex [Cp*Ir(biot- <i>p</i> -L)Cl], including biotin and the iridium catalyst (TM catalyst) within streptavidin (Sav) allowed the production of a transfer-hydrogenase (ATHase), an artificial metalloenzyme. Reproduced with permission from reference 17, Copyright (2012), Springer Nature.....	14
Figure 2. Enzymatic reaction in continuous flow reactors using supported enzymes. (a) Conversion of 1-phenoxypropan-2-one with 2-propylamine into the (<i>R</i>)-aminated derivative using ω -Transaminases immobilized on a porous support, namely EziG; (b) conversion of edible oils contained in waste stream at 30°C using a lipase immobilized onto a carbon support.	16
Figure 3. Enzyme immobilization onto a solid support. Enzyme (green) (a) adsorption; (b) covalent immobilization and (c) encapsulation/entrapment onto a solid support (cyan and grey).	17
Figure 4. Interfacial activation of lipases. Schematic depiction of interfacial activation upon immobilization on a hydrophobic surface (a-b). The hydrophobic lid of the lipase is orientated towards the active site when the enzyme is in an aqueous environment (a), rendering the enzyme inactive. The lipase absorption onto a hydrophobic support stabilizes the open conformation of the lid (b), activating the enzyme. Crystalline structure of <i>Candida antarctica</i> Lipase B with (c) closed state (occurs when the random coil, in magenta, closes the active site) and (d) open state showing a α -helix (yellow) at the place of the random coil (see (c)). The image was created with PyMOL (PDB 5A6V).....	18
Figure 5. Number of reports on selective bioconjugation based on amino acid chains. Adapted with permission from reference 41. Copyright (2020) American Chemical Society.....	20
Figure 6. Enzyme cross-linking reactions. Crosslinking of lysine residue (red) with glutaraldehyde forms an imine bond, whereas with NHS ester it results in the formation of an amide bond; the thiol moiety of cysteine (magenta) with the maleimide reagent forms a thioether bond; the carboxylic acid moiety of glutamic/aspartic acid (blue/green) and the C-terminus reacted with the carbodiimide reagents form an imine bond that is then converted into an amide bond upon reaction with primary amines. Representative amino acid residues were selected. The image was created with PyMOL and using lipase B (from <i>Candida antarctica</i>) as a template (PDB code: 1TCA).	21
Figure 7. Molecular dynamics (MD) simulations of site directed immobilization of an engineered β-galactosidase. Crystalline structure of an engineered β -galactosidase; (a) cysteines were introduced at positions 227 and 308 in the soluble enzyme structure; (b) their immobilization on a maleimide support, directed the active site toward the support. The simulation indicated that no substantial conformational changes were caused upon immobilization of both mutants. Adapted with permission from reference 51. Copyright (2017) Royal Society of Chemistry.....	22
Figure 8. Structural characterization of MOFs and encapsulated catalase. Transmission electron microscopy (TEM) micrographs of encapsulated catalase in (a–b) solid and (c–d) hollow MOFs. Schematic illustration of catalase encapsulated in (e) solid and (f) hollow MOFs. Adapted with permission from reference 54. Copyright (2020) American Chemical Society.....	23
Figure 9. Model of peptide anchoring mechanism on the surface of a solid support. Firstly the peptide diffuses toward the solid surface. Secondly, due to hydrophobic interactions with the surface or to hydrophilic interactions with the second water layer (WL) the peptide diffuses to the first WL. Finally, structural rearrangements of the peptide allow the adsorption of the peptide onto the solid surface. Reproduced with permission from reference 80. Copyright (2017) Royal Society of Chemistry.	26

Figure 10. Silica particles in various morphologies. Schematic representations (left column) of silica particles and their characterization with scanning (middle columns) and transmission (right column) electron microscopy (SEM and TEM). The morphology nomenclature for these particles is defined as (a) nonporous/dense; (b) hollow; (c) ordered mesoporous; (d) multi-shell; (e) core in hollow (rattle/egg yolk); (f) hollow with hierarchical pores; (g) core-shell. Adapted with permission from reference 91. Copyright (2016) American Chemical Society..... 29

Figure 11. Stöber synthesis scheme. The hydrolysis of tetraethoxysilane (TEOS) is followed by the polycondensation of the hydrolyzed TEOS. 30

Figure 12. Schematic depiction of cascade reaction inside hollow silica nanoparticles (HSNPs). The cascade reaction involving the glucose oxidase (GOx) and the magnetite nanoparticles was performed inside hollow silica nanoparticles, where both the enzyme and the inorganic catalyst were confined. The catalytic constant k_{cat} was 14 times higher when the two catalyst were confined inside the HSPs in comparison to the soluble counterparts. Adapted with permission from reference 99. Copyright (2020) American Chemical Society..... 31

Figure 13. schematic depiction on catalytic pocket of α -chymotrypsin (ChT) immobilized on gold nanoparticles (AuNPs). The charged substrate enters in the catalytic pocket (Asp102-Hys57-Ser195) only if its charge is positive (red circle) due to attraction with the charges on the surface of AuNPs. Adapted with permission from reference 114. Copyright 2006, American Chemical Society..... 34

Figure 14. β -galactosidase encapsulated in an organosilica layer. (a) Kinetic of organosilica layer growth on a shielded β -galactosidase (white squares) and on bare SPs (black squares). The layer thickness was measured from SEM micrographs (b) of the shielded particles (scale bar is 200 nm). Increase of layer thickness of 1.2 nm h^{-1} was calculated. (c) A Michaelis-Menten study of the shielded β -galactosidase. Adapted with permission from reference 74. Copyright (2016) John Wiley and Sons. 36

Figure 15. Schematic depiction of the strategy used to modify the enantioselectivity of esterases. While the (a) soluble esterase does not show enantioselectivity in the conversion of the methyl (*R/S*)-2-phenyl propanoate. (b) The immobilized and shielded enzyme shows improved enantioselectivity. In the box: Tetraethoxysilane TEOS (1), (3-aminopropyl) triethoxysilane APTES (2); 1-[3-(trimethoxysilyl)propyl]urea (3); benzyltriethoxysilane (4); hydroxymethyltriethoxysilane (5); and n-butyltriethoxysilane (6)..... 41

Figure 16. Crystal structure of EH₃. (a) Folding of the subunit showing the catalytic α/β hydrolase domain (orange), comprising six α -helices and eight β -strands, of which only β 2 is antiparallel. The cap domain (purple) involves five α -helices: α 1 (Pro17–Ala25), α 2 (Arg37–Asn45), α 3 (Pro47–Met63), α 7 (Pro234–Asn239) and α 8 (Gln250–Tyr255) (b) The channels providing access to the catalytic Ser192, as calculated with CAVER.¹⁴⁶ The acyl and alcohol binding sites are labelled. A third channel can be occupied by substrates with branched acyls. The polypeptide chain is colored in a rainbow code according to the B-factor values, from blue (low) to red (high); a very flexible loop linking α 1 to α 2 is essential in delineating the binding channels. The view is rotated 180° with respect to the view shown in (a) for a better view of the channels. (c) Homodimer, with the same coloring as in (a), showing the catalytic triad as sticks. Interaction between subunits occurs mostly through β 8, with additional contributions from the preceding and following helices (α 10, α 11). Both subunits are related by a two-fold axis that is perpendicular to the view shown and situates the two active sites on opposite faces of the dimer. 49

Figure 17. Nanobiocatalyst design, synthesis and characterization. (a) Schematic representation of EH₃ immobilization and protection in an organosilica layer of controlled thickness. The growth of this layer occurs through self-sorting and poly-condensation of hydrolyzed tetraethyl orthosilicate (TEOS) and organosilanes. (b) Molecular structures of the building blocks used in the protection layer formed by TEOS (1) (denoted as T); (3-aminopropyl)triethoxysilane (2) (APTES; denoted as A); 1-[3-(trimethoxysilyl)propyl]urea (3) (Ur); benzyltriethoxysilane (Bz) (4); hydroxymethyltriethoxysilane (Hm) (5); and n-butyltriethoxysilane (Bu) (6). Scanning electron microscopy (SEM) micrographs of (c) bare silica particles (SPs), (d) EH₃-T/A_[1/1], (e) EH₃-T/A_[4/1], (f) EH₃-T/A_[6/1], (g) EH₃-T/A_[10/1], (h) EH₃-

TBz/A_[4/1], (i) EH₃-TUr/A_[4/1], (j) EH₃-TBu/A_[4/1], (k) EH₃-THm/A_[4/1], and (l) EH₃-TBzUrBuHm/A_[4/1]. Scale bars of SEM micrographs represent 200 nm. Cryo-EM micrographs of (m) bare SPs used as support for the biocatalyst, (n) EH₃-SPs, and (o) EH₃-T/A_[4/1]. Scale bars of cryo-EM micrographs represent 100 nm. (p) Shield thicknesses (nm) ± standard error and polydispersity indices (PDI). PDI was calculated as the ratio of the standard deviation σ and the diameter mean (d) of the shielded particles (σ/d). Standard error is calculated as $\sigma ((d_{\text{bare}}-d_{\text{shield}})/2)/n$ where n is the number of measured particles. * is referred to 3h layer growth. 51

Figure 18. Substrate specificity study. Catalytic efficiency (k_{cat} , in s⁻¹) of soluble EH₃ versus k_{cat} of (a) EH₃-T/A_[1, /1], EH₃-T/A_[4/1], EH₃-T/A_[6/1], EH₃-T/A_[10/1] and (b) EH₃-TBz/A_[4/1], EH₃-TUr/A_[4/1], EH₃-TBu/A_[4/1], EH₃-THm/A_[4/1] and EH₃-TBzUrBuHm/A_[4/1] measured for 53 esters found to be hydrolyzed by any of the preparations (shown at the left side of a-panel). (c) Substrate repertoire and the k_{cat} (s⁻¹) measured for all TEOS/APTES compositions of the shield (a-panel) and for different silane compositions of the shield (b-panel). Hydrophobicity ($\log P$) and volume (Å³) of each of the esters are specifically indicated in the columns on the right. For activity determination, calculated on a continuous pH indicator assay.¹⁴³ The k_{cat} values are indicated by the size of the circles, according to the scale shown at right (for raw data, see **Table 6** Annex). Abbreviations as follows: BFPME: benzoic acid, 4-formyl-, phenylmethyl ester; BHPP: benzyl (R)-2-hydroxy-3-phenylpropionate. The substrates are ranked based on their volume (Å³). In red color, example of large and small volume substrates discussed in the text, are highlighted. 53

Figure 19. Enantioselectivity study. (a) Diagram of the specific activities of all preparations tested, with nine pairs of chiral substrates shown as a function of their hydrophobicity ($\log P$) and volume (Å³). In the left part of the diagram, the activities for the TEOS/APTES shield compositions are reported. In the right part, the activities for the silane compositions of the shield are reported. The panel was constructed as described in **Figure 18**. 57

Figure 20. Solvent stability study. Conversion of α -naphthyl acetate in the presence of increasing proportions of acetonitrile, by EH₃ (black), EH₃-T/A_[1/1] (red), EH₃-T/A_[4/1] (blue), EH₃-T/A_[6/1] (green) and EH₃-T/A_[10/1] (purple). Reactions were assayed using HPLC. 59

Figure 21. Enantioselectivity study. Kinetic conversion of ethyl (R)-4-chloro-3-hydroxybutyrate (E(R)CHB) and ethyl (S)-4-chloro-3-hydroxybutyrate (E(S)CHB) by EH_{1A1}, EH_{1A1}-TBu/A_[4/1], EH₇ and EH₇-TBu/A_[4/1], and a control reaction without enzymatic preparation added. The kinetics of the hydrolysis of separate enantiomers are shown, followed by recordings of the absorbance at 550 nm. At each data point, enantiomeric excess (*e.e.*%) was determined by HPLC using a racemic mixture of ethyl 4-chloro-3-hydroxybutyrate, as described previously. 64

Figure 22. Solvent stability study. Conversion of α -naphthyl acetate in the presence of increasing proportions of acetonitrile, by EH_{1A1} (black full squares), EH_{1A1}-T/A_[1/1] (black empty squares), EH₇ (red full triangles), EH₇-T/A_[4/1] (red empty triangles). 65

Figure 23. Schematic depiction of photothermal activation of enzymes in the Aurozyme. The Image was created with BioRender. The enzyme crystalline structure reported is that of the Lipase B from *Candida Antarctica* (CalB). 71

Figure 24. AuNPs properties. (a) TEM micrographs illustrating a library of different gold NPs with regular geometrical shapes and (b) branched shapes. Scale bars represent 100 nm. Figures adapted with permission from reference 169. Creative Common CC BY licence. (c) Schematic depiction of localized surface plasmon resonance (LSPR) typical on AuNPs. (d) LSPR absorbance of spherical silver and gold, branched gold and gold nanorods. Adapted with permission from reference 170, Copyright (2012) Royal Society of Chemistry. 74

Figure 25. Photothermal enhancement of enzyme activity. (a-b) Temperature increase upon irradiation of AuNPs and AuNRs measured with an IR camera; (c) increase in relative activity for the enzyme immobilized on AuNRs and on (d) AuNPs. Reprinted (adapted) with permission from reference 182. Copyright (2017) American Chemical Society. 77

- Figure 26. Synthesis of the nanobiocatalyst.** Schematic representation of AuNPs (1) and enzyme (2) immobilization and protection (3) in an organosilica layer of controlled thickness. 78
- Figure 27. Structural details of β -gal and CalB.** Crystal structures of (a) β -gal from *K. lactis* and of (b) CalB. (c) Summary of structural details of the two enzymes (PDB 3OBA for β -gal and 1TCA for CalB). 78
- Figure 28. Synthesis of AuNPs with citrate as reducing agent and capping material.** Au³⁺ are firstly reduced to Au⁰ at 90°C and then stabilized by the citrate (8), in water. 79
- Figure 29. AuNPs characterization.** (a) TEM micrographs; (b) statistical analysis based on TEM micrographs (a); (c) SEM micrographs and (d) AFM image of AuNPs-citrate. (e) Calibration line of absorbance at 520 nm vs. concentrations of a solution of commercial AuNPs citrate; (f) absorption spectra of AuNPs-citrate solution before (red line) and after freeze-drying, in presence of sucrose 5% w/v, diluted 10 x (blue line). 81
- Figure 30. Characterization of AuNPs-citrate electrostatic immobilization on SPs.** SEM micrographs after AuNPs immobilization on SPs functionalized with (a) 2.6 mM; (b) 7.8 mM and (c) 26 mM of APTES (2). Scale bars represent 200 nm. 83
- Figure 31. Characterization of AuNPs-SPs after enzyme immobilization.** SEM micrographs of SPs amino modified with 26 mM APTES before (a) and after (b) enzyme-glutaraldehyde crosslinking. Scale bars represent 200 nm. 84
- Figure 32. Characterization of AuNPs covalent immobilization on SPs.** (a) Structures of L-cysteine (9) and cysteamine (10); (b) SEM micrograph of AuNPs with cysteine as capping material immobilized on amino modified SPs; (c) structure of 3-(mercaptopropyl)trimethoxysilane (MPTES) (11). 85
- Figure 33. Schematic depiction of the strategy used to covalently bind AuNPs on SPs.** SPs surface was firstly modified with -SH functions by polycondensation of MPTES in the presence of amines as catalyst. After the thiol- and amino- modified SPs were incubated with AuNPs. 86
- Figure 34. Characterization of AuNPs covalent immobilization on silica with thiol functions on the surface.** SEM micrographs of AuNPs immobilized on SPs modified with thiol groups using three different conditions (a, b, c). The SPs were reacted with (a) MPTES and APTES; (b) MPTES and ammonia; (c) MPTES, APTES and ammonia. The reaction time was 1.5 h (a₁, b₁ and c₁); 3.5 h (a₂, b₂ and c₂) and 20h (a₃, b₃ and c₃). All scale bars represent 200 nm. 87
- Figure 35. UV-vis characterization of AuNPs in the supernatant after AuNPs immobilization on SPs.** Absorption spectra of the initial AuNPs-citrate diluted 10 times (black line) and of the supernatant after AuNPs immobilization on SPs (grey line). 88
- Figure 36. AuNPs-SPs characterization.** Absorption spectra of the free AuNPs-citrate (black line), of the supernatant after glutaraldehyde crosslinking (grey line), of the AuNPs-SPs after glutaraldehyde crosslinking (red line) and of the AuNPs-SPs after CalB immobilization (green line). 89
- Figure 37. Nanobiocatalyst characterization.** SEM micrographs of the (a) immobilized AuNPs-CalB-SPs and (b) shielded AuNPs-CalB-SP_{OS} (scale bars represent 200 nm). Cryo-EM micrographs of the (c) immobilized AuNPs on SPs and (d) shielded AuNPs-CalB-SP_{OS} (scale bars represent 100 nm). (e) Statistical distribution of bare SPs diameters (red bars) and of shielded AuNPs-CalB-SP_{OS} (grey bars) diameter, 106 particles were measured. 91
- Figure 38. CalB-SPs characterization.** SEM micrographs of (a) bare SPs and (b) shielded CalB-SP_{OS} used for control experiments; (c) statistical distribution of bare SPs diameters (red bars) and of protected CalB-SP_{OS} (grey bars). The average diameter of the shielded particles was 319 ± 12 nm, corresponding to a layer of 18 nm in thickness. Scale bars represent 200 nm 92
- Figure 39. AuNPs- β gal-SP_{OS} and β gal-SP_{OS} characterization.** SEM micrographs of (a) AuNPs- β gal-SP_{OS} and (b) β gal-SP_{OS} used for control experiments. Scale bars represent 200 nm. (c) Statistical analysis of SPs, AuNPs- β gal-SP_{OS} and β gal-SP_{OS} diameter. 94

Figure 40. Experimental set-up used for laser irradiation at controlled temperature. (a) A laser (MGL-H-532nm-500mW-17111070) was connected through (b) an optical fiber (diameter 600 μm) to (c) a cuvette holder where the sample was stirred during the assay. The cuvette holder was maintained at a fixed temperature by means of (d) a temperature controller. 95

Figure 41. Activity study. Concentration of *p*-nitrophenol (*p*NP) produced by (a) AuNPs-CalB-SPs (empty symbols) and by AuNPs-CalB-SP_{OS} (filled symbols); (b) a solution of soluble CalB and free AuNPs present at the same concentration than in the immobilized and protected system and by (c) CalB-SPs and CalB-SP_{OS}. All kinetics were measured in dark condition (black squares) and upon laser irradiation (grey triangles) using 615 mW laser power. (d) Activities [U] calculated from the linear fits on (a), (b) and (c). 96

Figure 42. Activity test on CalB-AuNPs-SP_{OS} at different temperatures. (a) Activity [U] of CalB-AuNPs-SP_{OS} measured in the dark (black squares) and upon laser irradiation at 615 mW (grey triangles); (b) summary of activities [U] measured at different temperatures and activities % increase upon irradiation. *the activity assay at 10°C was performed for 20 min due to the freezing of the solution, samples were tested for 30 min at the other temperatures. 97

Figure 43. Activity increase [U%] upon irradiation vs laser power. Study of the AuNPs-CalB-SP_{OS} activity at 10°C using different laser power values 94, 231, 451, 548, 613 mW..... 97

Figure 44. Activity study. Concentration of *o*-NP produced by (a) AuNPs- β gal-SPs (empty symbols) and by AuNPs- β gal-SP_{OS} (filled symbols); (b) a solution of soluble β gal and free AuNPs present at the same concentration than in the immobilized and protected particles and by (c) β gal-SPs and β gal-SP_{OS}. All kinetics were measured in dark condition (black squares) and upon laser irradiation (grey triangles) at 615 mW laser power. (d) Activities [U] calculated from the linear fit of (a), (b) and (c)..... 99

Figure 45. U% increase of AuNPs- β gal-SPs and AuNPs- β gal-SP_{OS} upon irradiation vs. laser power. The activity study was performed using 94, 223 and 615 mW laser power. AuNPs- β gal-SPs (empty symbols) and AuNPs- β gal-SP_{OS} (filled symbols). 100

Figure 46. Activity test on AuNPs- β gal-SPs at different temperatures. (a) Comparison of activity [U] of AuNPs- β gal-SPs measured in the dark (black squares) and upon laser irradiation at 615 mW (grey triangles); (b) summary of activities [U] measured at different temperatures and activities % increase upon irradiation. 101

Figure 47. Active site of EH₃. (a) Molecular surface of the EH₃ monomer, in the same orientation to that in Figure 1, showing a tunnel 18 Å deep giving access to the catalytic triad formed by Ser192, Asp291 and His321, through the cap domain (EH₃ is coloured with the same code than in Figure 1). (b) Ensemble refinement performed with the EH₃ coordinates showing potential conformations of the N-terminal region comprising α 1 and α 2 (colour code gives chain mobility, from low in blue to high in red). The catalytic triad is shown as sticks. (c) A close view of the EH₃-butyl-hexyl phosphonate complex mimicking the tetrahedral intermediate of the hydrolytic reaction. The 2Fo-Fc electronic density map at the inhibitor contoured at 0.9 σ cut-off is shown in green. The catalytic Asp291 stabilizes His321, the proton donor/acceptor, which deprotonates the hydroxyl of serine (situated at the “nucleophilic elbow” between β 5 and α 6) enabling its role as nucleophile. Then, it attacks the ester carbonyl resulting in a tetrahedral intermediate, where the oxygen is hydrogen bonded to glycine at the oxoanion hole (Gly112, Gly113 and Gly193). Hydrogen bonds network is shown as dashed lines. (d) A cross-section of the molecular surface of EH₃ showing the catalytic pocket occupied by the phosphonate inhibitor, and the residues bordering the alcohol (black) and acyl (grey) binding sites. 125

Figure 48. Lys residues on the surface of EH₃. Molecular surface of the two molecules (pink and beige) of the EH₃ dimer showing the position of the Lys residues represented as spheres, with the amine nitrogen atom colored in blue. The phosphonate inhibitor is shown as green sticks in the active site of one of the monomers, while the other active site is hidden at the opposite face of the dimer. Two 90° opposite sense rotations display the top/bottom views of the central picture. Most of the Lys residues are on the “top hemisphere”, which is the putative region involved in immobilization of EH₃ to the support. 126

Figure 49. Enzyme immobilization optimization. Different concentration of EH₃ have been tested (x axis). After immobilization, the supernatant was recovered and the concentration (in $\mu\text{g mL}^{-1}$) of unbound enzyme was measured by means of BCA assay. 127

Figure 50. Lys residues at the surface of EH_{1A1} (PDB code 6RB0). Molecular envelope of the two monomers (raspberry and beige) within the dimer, showing their flexible cap domains as cartoon. The superficial Lys residues are represented as yellow spheres, with their amine nitrogen atom colored in blue. A phosphonate inhibitor is shown as green sticks to highlight the active site within each monomer. 128

Figure 51. EH_{1A1} and EH₇ scanning electron microscopy (SEM) characterization. Micrographs of (a) EH_{1A1}-TBu/A_[4/1] and (b) EH₇-TBu/A_[4/1]. Scale bars represent 200 nm. 129

Figure 52. EH_{1A1} and EH₇ Selectivity study. k_{cat}/K_m study of EH_{1A1}, EH_{1A1}-TBu/A_[4/1], EH₃ and EH₃-TBu/A_[4/1], EH₇ and EH₇-TBu/A_[4/1] sub-enzymes measured for a set of esters found to be hydrolysed by any of the preparations (shown at the left side of a panel). Hydrophobicity ($\log P$) and volume (\AA^3) of each of the esters are specifically indicated in the columns on the right. For activity determination, calculated on a continuous pH indicator assay.¹⁴³ The k_{cat}/K_m values are indicated by the size of the circles, according to the scale shown at right (for raw data, see **Table 9** Annex). Abbreviations as follows: BFPME: benzoic acid, 4-formyl-, phenylmethyl ester; BHPP: benzyl (*R*)-2-hydroxy-3-phenylpropionate. The substrates are ranked based on their volume (\AA^3). The panel was created as described in **Figure 18**. 130

Figure 53. EH_{1A1} and EH₇ Enantioselectivity study. (a) Diagram of the k_{cat}/K_m values of EH_{1A1}, EH_{1A1}-TBu/A_[4/1], EH₃ and EH₃-TBu/A_[4/1], EH₇ and EH₇-TBu/A_[4/1] preparations tested, with nine pairs of chiral substrates shown as a function of their hydrophobicity ($\log P$) and volume (\AA^3). The k_{cat}/K_m values are indicated by the size of the circles, according to the scale shown at right (for raw data, see **Table 9**). The panel was created as described in **Figure 18**. 131

LIST OF TABLES

Table 1. Shield thicknesses (nm) \pm standard error and PDI indices, calculated as in Figure 17 . Standard error values are calculated from 3 batches of particles prepared separately.....	61
Table 2. Zeta potential values of SPs functionalized with different concentrations of APTES (2).	83
Table 3. Statistical details of AuNPs calculated using TEM micrographs and of bare SPs, CalB-SPos and AuNPs-CalB-SPos calculated using SEM micrographs.	93
Table 4. Crystallographic statistics of EH ₃	132
Table 5. Silanes used for the production of protective shields.....	133
Table 6. List of carboxyl esters substrates found to be converted by EH ₃ . The table reports the k_{cat} values for a number of non-chiral (a) and chiral (b) esters. The following information are provided: name of ester, $LogP$ value of the ester calculated using the ACD/ChemSketch 2015.2.5 software, molecular volume of the ester calculated as described in http://www.molinspiration.com/cgi-bin/properties , and average k_{cat} in s ⁻¹ . The assays were performed at 30°C and pH 8.0. The data shown in this table, correspond to average values of three technical assays using one immobilized preparation per each enzyme. The standard deviation was less than 1% for all measurements.....	141
Table 7. k_{cat} ratio for preferred over non-preferred ester for 9 pairs of enantiomers as determined following hydrolysis of separate enantiomers using EH ₃ preparations. average values of three technical assays using one immobilized preparation per each enzyme are reported.....	145
Table 8. $e.e\%$ for methyl (<i>R/S</i>)-2-phenylpropanoate as determined by GC following hydrolysis of a racemic mixture using EH ₃ and the immobilized preparations. Results correspond to average values of three technical assays using one immobilized preparation per each enzyme.	146
Table 9. List of carboxyl esters substrates found to be converted by EH _{1A1} , EH _{1A1} -TBU/A _[4/1] , EH ₇ and EH ₇ -TBU/A _[4/1] . Shown are the k_{cat} , K_m and k_{cat}/K_m values for a number of non-chiral (a) and chiral (b) esters. The following information is provided: name of ester, $LogP$ value of the ester calculated using the ACD/ChemSketch 2015.2.5 software, molecular volume of the ester calculated as described in http://www.molinspiration.com/cgi-bin/properties , and average k_{cat} , K_m and k_{cat}/K_m values. The assays were performed at 30°C and pH 8.0, the average values are given, and the standard deviation was less than 1% in all cases. For comparison, values for EH ₃ and EH ₃ -TBU/A _[4/1] , are included. Assays consist in three technical (immobilized) replicates of three different enzymes independently prepared. The standard deviation of the linear fit of replicates is shown, as calculated with Sigma Plot 13.0.....	147
Table 10. Kinetic parameters, E_{app} and $e.e\%$ for EH ₃ and EH ₃ -TBU/A _[4/1] against methyl-(<i>R</i>)-2-phenylpropanoate and methyl-(<i>S</i>)-2-phenylpropanoate. Assays consist in three technical (immobilized) replicates of three different enzymes independently prepared. The standard deviation of the linear fit of replicates is shown, as calculated with Sigma Plot 13.0.	152
Table 11. Kinetic parameters, E_{app} and $e.e\%$ for for EH _{1A1} , EH _{1A1} -TBU/A _[4/1] , EH ₇ and EH ₇ -TBU/A _[4/1] against ethyl (<i>R</i>)-4-chloro-3-hydroxybutyrate and ethyl (<i>S</i>)-4-chloro-3-hydroxybutyrate. The assays, in triplicates, were performed as for EH ₃ . The standard deviation of the linear fit of triplicates is shown, as calculated with Sigma Plot 13.0.	153

ABBREVIATIONS

AFM	Atomic Force Microscopy
APTES, A	(3-aminopropyl)triethoxysilane
AuNPs	Gold Nanoparticles
BCA	bicinchoninic acid assay
BSA	Bovine Serum Albumine
Bu	n-butyltriethoxysilane
Bz	benzyltriethoxysilane
CalB	Lipase B from <i>Candida Antarctica</i>
DLS	Dynamic Light Scattering
EH ₃	Ester hydrolase 3
HEPES	(4-(2-hydroxyethyl)-1-piperazineethanesulfonic acid
Hm	hydroxymethyltriethoxysilane
MES	2-(N-morpholino)ethanesulfonic acid
MPTES	(3-mercaptopropyl)triethoxysilane
<i>o</i> NP	ortho-nitrophenol
<i>o</i> NPG	ortho-nitrophenyl- β -galactoside
pNP	4-nitrophenol
pNPB	4-nitrophenyl butyrate
SEM	Scanning Electron Microscopy
SPs	Silica Particles
T	temperature
TEM	Tunnel Electron Microscopy
TEOS, T	tetraethyl orthosilicate
TRIS	tris(hydroxymethyl)aminomethane
Ur	1-[3(trimethoxysilyl)propyl]urea
β gal	β galactosidase

CHAPTER 1
INTRODUCTION

Enzymes are biomolecules able to catalyze a wide range of biological reactions and to control complex metabolic pathways. The evolution of enzymes has led to biocatalytic processes that are extremely efficient, enantio-, chemo- and regio-selective and specific to diverse conditions (e.g. pH, temperature, solvents).¹

Enzymatic processes in nature have inspired scientists in different research fields to develop and continuously improve biocatalysis, using enzymes to catalyze chemical reactions. Today, biocatalysis is an important field of research in both academic and industrial level. The enormous efforts made by scientists on the optimization of the catalytic properties of enzymes and on the improvement of their stability in harsh conditions (e.g. at high or low temperatures, in the presence of organic solvents or at a broad range of pH) allowed the use of enzymes in several industrial processes.¹ With the aim of producing novel efficient biocatalysts, several multidisciplinary strategies have been used.²⁻³ In this context, among protein engineering approaches and chemical modifications of enzymes, the bioconjugation of enzymes to solid supports, known as enzyme immobilization, has proven to be a promising approach.

This chapter provides an overview of the methods used to modify enzyme catalytic properties, with a focus on enzyme immobilization. A general overview of the properties of materials used for enzyme immobilization and their impact on enzyme properties, is provided. As silica and organosilica are the main materials used in the work described in this thesis their characteristics and their application as a support for enzyme immobilization, are reviewed. Another technique for the modification of enzyme catalytic properties, consisting of tuning the enzyme environment is discussed as a joint strategy with enzyme immobilization.

1 METHODS FOR THE MODIFICATION OF ENZYME PROPERTIES

Approaches to modify the catalytic properties of enzymes can be generally classified into protein engineering⁴ and chemical protein modification.⁵ Protein engineering approaches such

as directed enzyme evolution provided enormous advances in this context, as confirmed from the work of Frances H. Arnold, who was awarded the Nobel Prize in Chemistry.⁶ Protein engineering includes the synthesis of new enzymes and the modification of existing ones genetically modifying their amino acid sequence. This approach, often, requires a rational knowledge of the structure of the desired protein and of the link between protein structure and function (**Figure 1**). The availability of numerous techniques for designing, screening and selecting enzymes⁷⁻⁸ by means of several analytical tools (e.g. crystallographic analytical methods,⁹ Fourier-transform infrared spectroscopy (FTIR), Raman and circular dichroism (CD) spectroscopies,¹⁰ calorimetric methods¹¹ and nuclear magnetic resonance (NMR)¹²⁻¹³), allowed a significant understanding of the soluble enzyme properties. Those efforts permitted generating new biocatalysts able to catalyze unknown reactions in nature.⁶ The group of Frances H. Arnold, by means of directed evolution method, demonstrated for the first time the possibility to produce Si-C bonds with an enzymatic process catalyzed by a cytochrome C. The biocatalyst showed 15 times higher turnover than the catalysts currently used in industry for performing this reaction.¹⁴

By contrast, chemical protein modification is a post translational approach, in which enzyme catalytic properties are tuned through chemical modification (e.g. acylation, glycosylation, phosphorylation, methylation) of targeted amino acid side chains.¹⁵ Moreover, the availability of several chemical moieties on amino acid residues allowed the bioconjugation of enzymes to materials ranging from other biomolecules (e.g. proteins in cross-linked enzyme aggregate) to organic or inorganic materials.¹⁶

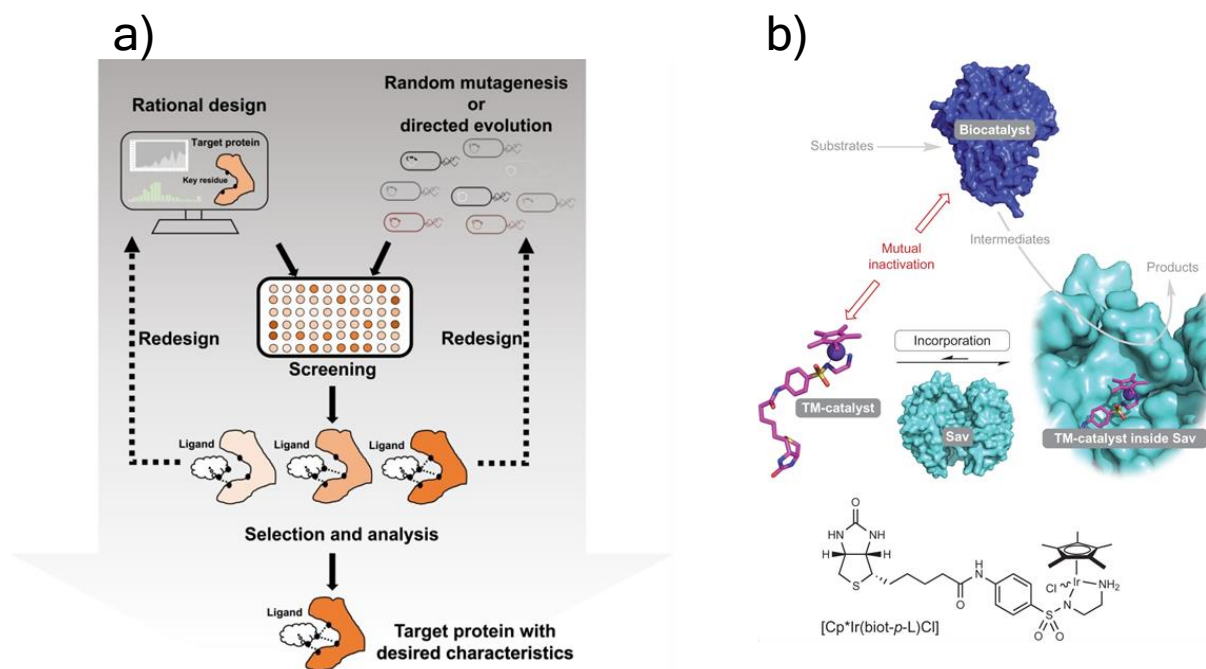


Figure 1. Protein engineering and artificial metalloenzyme methods. (a) Schematic depiction of the protein engineering process. The protein with desired properties (e.g. enhanced catalytic activity, increased stability in extreme conditions) can be selected among a library of variants and further analyzed. Adapted with permission from reference 8. Copyright (2019) Elsevier Ltd.; (b) the complex [Cp*Ir(biot-*p*-L)Cl], including biotin and the iridium catalyst (TM catalyst) within streptavidin (Sav) allowed the production of a transfer-hydrogenase (ATHase), an artificial metalloenzyme. Adapted with permission from reference 17, Copyright (2012), Springer Nature.

With covalent or supramolecular anchoring strategies, a metal cofactor moiety can be inserted into a protein scaffold allowing the production of artificial metalloenzymes, which represent powerful tools for accomplishing diverse objectives in synthetic chemistry and biology.¹⁸ Köhler *et al.* demonstrated the possibility to carry out tandem reactions with organometallic catalyst and enzymes (**Figure 1**). Issues regarding the inactivation of both the catalyst and the enzyme have been overcome by inserting the metal catalyst into a protein scaffold. The artificial transfer-hydrogenase (ATHase) produced was then combined with various redox enzymes to catalyze cascade reactions, such as cofactor recycling, stereoselective amine deracemization and others.¹⁷

As the approach used in this thesis work for the modification of enzyme catalytic properties was based on enzyme immobilization methods, the rest of this chapter focuses on the

bioconjugation of enzymes onto solid supports. For a complete overview of protein engineering and chemical protein modification, the reader is directed to three comprehensive reviews on these topics.^{5, 19-20}

2 ENZYME IMMOBILIZATION ONTO SOLID SUPPORTS

In 1974 Wingard *et al.* wrote,²¹ in a meeting report on the Enzyme Engineering conference held in August 1973:

“More than 190 selected speakers and scientists from 18 countries participated, including biochemists, chemical engineers, microbiologists, and a variety of other specialists from industry, government, and universities [...] Wingard, Jr. (University of Pittsburgh) opened the conference by citing the developments since the 1971 conference and by challenging the participants with the need for definitive economic and technical evaluations of specific applications of immobilized enzymes, for greatly improved feedback on economic and operational problems from industry to universities and granting agencies, and for more academic input toward resolving the more difficult problems of enzyme stability, cofactor systems, multienzyme systems, and enzyme moderated energy transfer.”

This report attests to the interdisciplinarity feature intrinsic to the field of enzyme immobilization, which brings together scientists from diverse fields. Remarkably, it also shows that enzyme immobilization, has remained a topic of interest for almost 50 years. Enzyme bioconjugation on a solid support has been widely exploited since the first published report on invertase absorption on charcoal and aluminium dioxide in 1918.²² In this report, Nelson and Griffith reported that the loss of enzymatic activity upon immobilization of the invertase on charcoal was due to a different pH in the enzyme environment. Additionally, due to the limited knowledge on protein structures, Nelson and Griffith concluded that an enzyme can be considered as a colloid.²² Since this pioneering research, enzyme immobilization was widely

investigated and the knowledge on protein structure is now dramatically advanced. However, when it comes to apply the analytic and design tools for protein structure determination, mentioned in section 1, on immobilized enzymes it is extremely challenging to obtain conclusive results. Indeed, when the enzyme immobilization leads to modifications e.g. in the active site, crystallographic techniques are unsuitable. Additionally, the structural characterization methods suitable for soluble enzymes require a high enzyme to/support material ratio, which is often difficult to achieve. Furthermore, support materials can interfere with the measurements.

Despite the challenge on the determination of the protein structure upon immobilization, the bioconjugation to solid supports allowed tuning enzymes properties such as turnover rate, selectivity and stability, in addition to providing the possibility of reusing the supported biocatalyst.^{3, 23-26} As a result, immobilized enzymes were implemented in catalytic conversion in continuous flow processes.²⁷

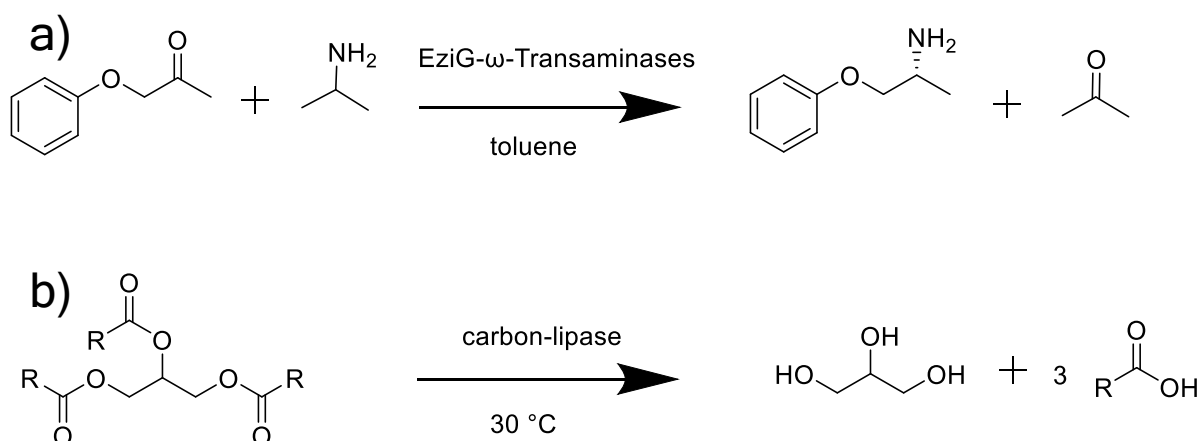


Figure 2. Enzymatic reaction in continuous flow reactors using supported enzymes. (a) Conversion of 1-phenoxypropan-2-one with 2-propylamine into the (*R*)-aminated derivative using ω -Transaminases immobilized on a porous support, namely EziG; (b) conversion of edible oils contained in waste stream at 30°C using a lipase immobilized onto a carbon support.

Böhmer *et al.* recently demonstrated the possibility to use ω -Transaminases for the first time in neat organic solvent (i.e. toluene), in continuous flow reaction for catalysis. By enzyme

immobilization onto a glass porous support, namely EziG, it was possible to catalyze the amination reaction reported in **Figure 2** in continuous flow with conversion yields as high as 96% and high enantioselectivity (e.e. % 99).²⁸ Immobilized lipases on nanoporous carbon have also been used to process edible oil found in waste stream of fuels refineries. The hydrolysis of edible oils was performed in a packed bed reactor yielding the 99% of hydrolyzed product (**Figure 2**).²⁹

Enzyme immobilization can be classified with respect to the procedure used to conjugate the enzyme to the support material.³⁰ The main strategies for enzyme conjugation are enzyme adsorption, covalent immobilization and entrapment.

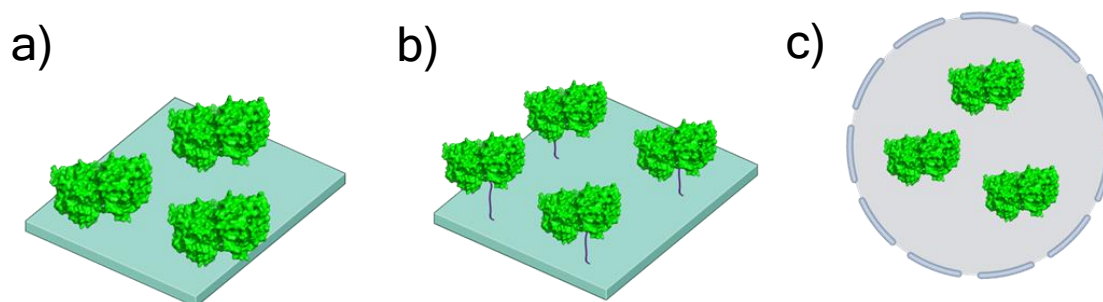


Figure 3. Enzyme immobilization onto a solid support. Enzyme (green) (a) adsorption; (b) covalent immobilization and (c) encapsulation/entrapment onto a solid support (cyan and grey).

Enzyme adsorption

Enzyme adsorption on a support material occurs through physical interactions such as van der Waals forces, hydrophobic interactions, and ionic or hydrogen bonds.

Enzyme adsorption methods display several advantages for the immobilization of enzymes. First, they allow for enzyme immobilization without chemical manipulation of the enzyme. Second, enzyme adsorption is generally non-destructive toward enzyme activity, due to the reduced probability of inducing conformational changes on the enzyme structure. Finally, being reagent free it is a simple and low-cost strategy.³⁰

Adsorption of lipases has been shown to allow the modulation of the enzymes structure and catalytic activity.³¹⁻³⁴ This was possible due to the stabilization, by the hydrophobic support, of the most catalytic active state of the lipase. Lipases are characterized by the presence of a flexible structural domain, namely lid, located over the active site and including hydrophobic residues.³⁵ When the enzyme is in aqueous media the lid is closed, while in presence of a hydrophobic layer the lid changes his conformation to a partial open state, due to the interfacial activation mechanism, which makes the active site available for catalysis (Figure 4).³⁵

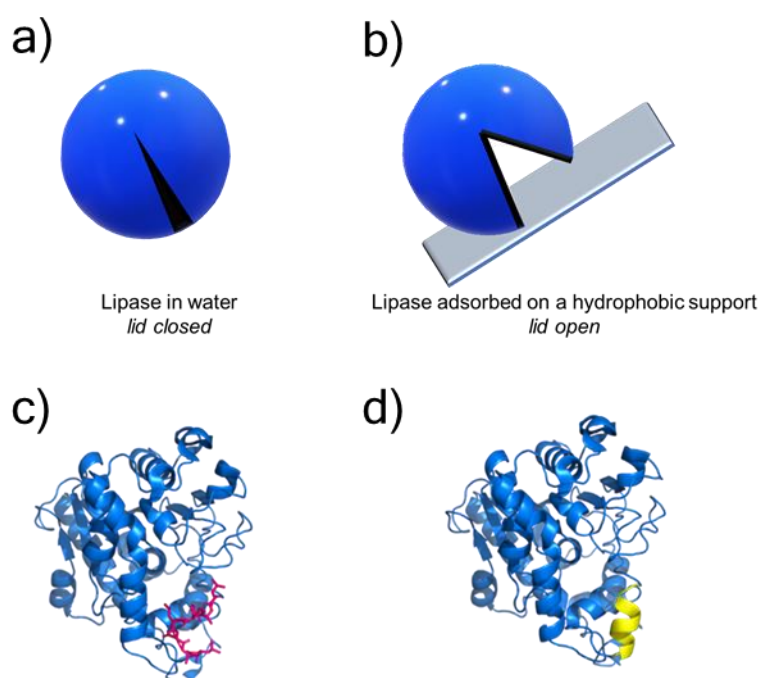


Figure 4. Interfacial activation of lipases. Schematic depiction of interfacial activation upon immobilization on a hydrophobic surface (a-b). The hydrophobic lid of the lipase is orientated towards the active site when the enzyme is in an aqueous environment (a), rendering the enzyme inactive. The lipase absorption onto a hydrophobic support stabilizes the open conformation of the lid (b), activating the enzyme. Crystalline structure of *Candida antarctica* Lipase B with (c) closed state (occurs when the random coil, in magenta, closes the active site) and (d) open state showing a α -helix (yellow) at the place of the random coil (see (c)). The image was created with PyMOL (PDB 5A6V).

Interestingly, in the specific case of the Lipase B from *Candida antarctica* (CalB) the presence of a lid causing the interfacial activation is unclear and matter of debate. The reason of this unclarity lies in the size of the structural domain that could be considered as a lid.³⁵ The lid of CalB has a limited size including only few amino acid residues and therefore it is expected not

to strongly impact the catalytic performance of the lipase. However, structural investigations on CalB revealed that the switch between its open and closed state occurs by the conformational change of a structural domain (from Leu140 to Leu147) in the vicinity of the active site, from a α -helix to a random coil (Figure 4).³⁶ On account of the interfacial activation mechanism, immobilization of lipases produced good results in terms of improvement of activity of the supported enzyme in comparison with its soluble counterpart.³⁷⁻³⁸ Bastida *et al.* showed that a lipase from *Humicola lanuginosa* immobilized on octyl-agarose gel, hydrolyzed up to 20 times more *p*-nitrophenyl propionate than the corresponding soluble lipase.³⁹

However, enzyme adsorption has some limitations. The enzyme can leach from the support due to changes in temperature, pH or ionic strength, thus hindering the reusability and the stability of the biocatalyst.³⁰ Moreover, immobilization without a spacer between the enzyme and the surface of the support causes steric constraints, which can lead to the structural unfolding of the enzyme.⁴⁰ Thus, there is a need for alternative approaches that allows producing more stable biocatalysts with improved catalytic activity.

Covalent immobilization and cross-linking of enzyme

Covalent immobilization of enzymes is based on the formation of multiple covalent bonds between amino acid residues of the enzyme and the chemical moieties of the support material.³⁰ The advantage of this approach is that it permanently binds the enzyme to the support. The multipoint binding of the enzyme to the solid support reduces the flexibility of the enzyme. As a consequence, the resistance of enzyme to denaturation stress is increased.⁴¹⁻⁴² The covalent immobilization of enzymes is typically carried out by selectively targeting side chains of amino acid residues on the protein.⁴¹⁻⁴² Many studies have been reported on enzyme bioconjugation by targeting the thiol moiety of cysteine and the amino group of lysine. Bioconjugation via the phenolic moiety of tyrosine, the indole moiety of tryptophan and the imidazole of histidine has

been less studied. Studies of bioconjugation through other amino acid residues, from the carboxylic moiety of aspartic acid and glutamic acid to the hydroxyl moiety of serine, are even less common (**Figure 5**).⁴²

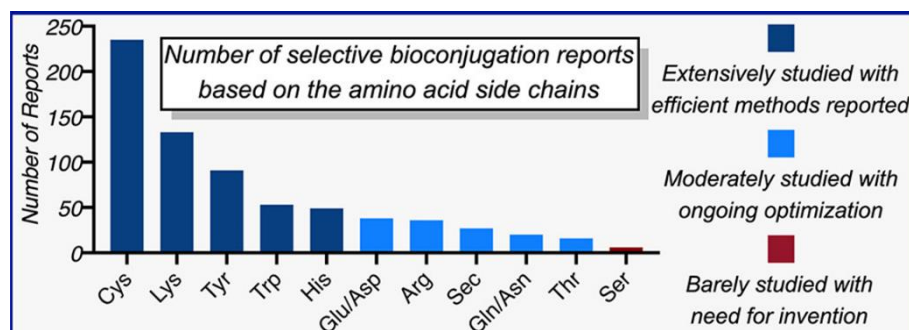


Figure 5. Number of reports on selective bioconjugation based on amino acid chains. Adapted with permission from reference 42. Copyright (2020) American Chemical Society.

For immobilizing enzymes onto solid supports, it is common practice to use molecular crosslinkers with two anchoring groups: homobifunctional crosslinkers have two identical anchoring groups, whereas heterobifunctional crosslinkers have two different groups. The diversity of chemical functions on enzymes, the wide range of crosslinkers, and the broad selection of supports for covalent immobilization have led to myriad possibilities when choosing the most appropriate experimental conditions.

Examples of enzyme crosslinking to a solid support have been reported for immobilization on aminated supports by targeting lysine residues. This procedure, which takes advantage of the large number of lysine residues available throughout the surface of enzymes, is typically applied if site-specific immobilization is not needed^{41, 43} To this end, one of the most frequently used crosslinkers is glutaraldehyde, due to its low cost and high reactivity in water at pH 7 (**Figure 6**).⁴⁴ This crosslinking method results in the formation of an imine bond between the enzymes and the support. As the resulting imine bond is reversible, this strategy can lead to enzyme leaching. To prevent this, a reducing agent such as sodium borohydride is often added to reduce the imine bond to amine.⁴⁴

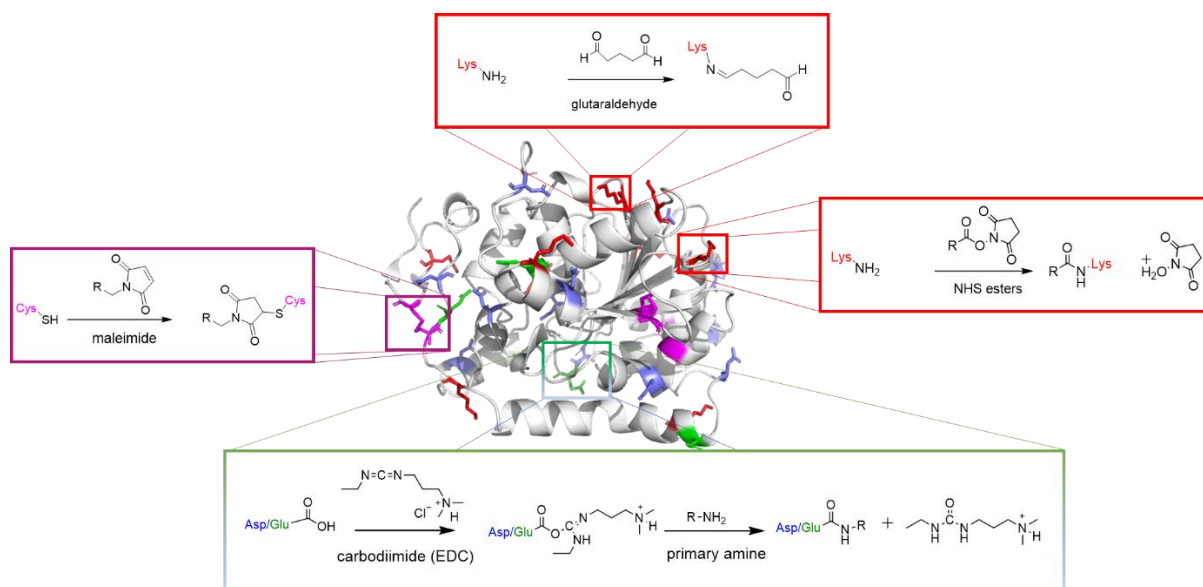


Figure 6. Enzyme cross-linking reactions. Crosslinking of lysine residues (red) with glutaraldehyde forms an imine bond, whereas with NHS ester it results in the formation of an amide bond; the thiol moiety of cysteine (magenta) with the maleimide reagent forms a thioether bond; the carboxylic acid moiety of glutamic/aspartic acid (blue/green) and the C-terminus reacted with the carbodiimide reagents form an imine bond that is then converted into an amide bond upon reaction with primary amines. Representative amino acid residues were selected. The image was created with PyMOL and using lipase B (from *Candida antarctica*) as a template (PDB code: 1TCA).

In other examples, N-hydroxysuccinimide (NHS) esters have been used to cross-link enzymes to their support by forming an amide bond, which is a remarkably stable bond (bond dissociation energy ΔH°_{298} 440-300 kJ mol⁻¹ according to the substituent on the nitrogen).⁴⁵ Along with the ϵ -amines of the lysine and of the N-terminus, the thiol moiety of cysteine is widely targeted for enzyme covalent immobilization due to its high nucleophilicity. In addition, the possibility of activating the carboxylate moieties towards nucleophiles makes them frequently used (Figure 6).^{43, 46}

Nevertheless, most immobilization techniques cannot control the final orientation of the enzyme toward the support. Rivero *et al.* used a computational method to study the orientation changes of a phosphopentomutase upon immobilization on differently activated agarose supports, and then related the structural information to the enzyme activity. The authors reported that enzyme immobilization onto agarose support activated with cyanogen bromide, occurred via the N-terminus, re-orienting the enzyme with its active site facing the support.

This caused partial blocking of the active site, consequently the catalytic activity of the supported enzyme was reduced in comparison to that of its soluble counterpart.⁴⁷ To enable site directed immobilization, the protein must be immobilized via a specific residue,⁴⁸ which can be introduced by protein engineering.⁴⁹ In alternative, significant efforts have been made to develop new strategies for targeting amino acid residues with low availability such as tryptophan and cysteine, which both have a frequency in protein structures of ca. 1%.^{42, 50-51}

Y. Liu *et al.* engineered a β -galactosidase with one cysteine accessible at the surface (**Figure 7**).⁵² Combining a vibrational spectroscopy study with molecular dynamics (MD) simulations, they determined that, upon immobilization, the active site of the enzyme was directed towards the support material activated with maleimide.⁵² However, the authors reported that the two mutants exhibited limited activity when immobilized. In contrast, the enzyme activity drastically increased when immobilized on a mixed maleimide:hydroxyl functionalized surface. The MD simulation study revealed an higher mobility of the enzymes on the more hydrophilic surface, probably due to the weaker interactions between the enzyme and the surface.

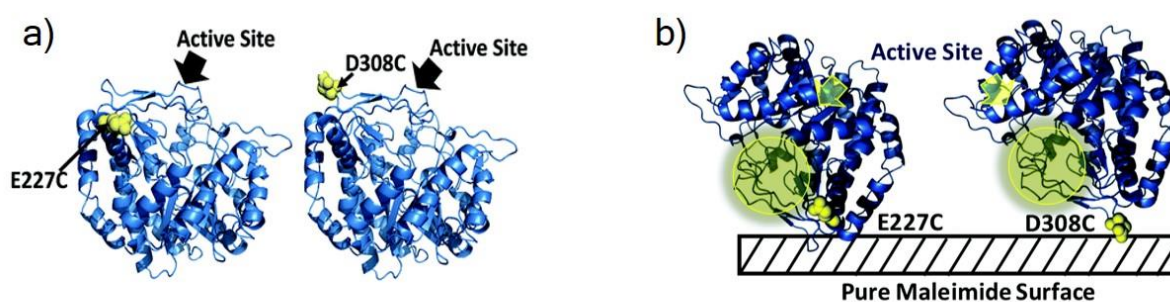


Figure 7. Molecular dynamics (MD) simulations of site directed immobilization of an engineered β -galactosidase. Crystalline structure of an engineered β -galactosidase; (a) cysteines were introduced at positions 227 and 308 in the soluble enzyme structure; (b) their immobilization on a maleimide support, directed the active site toward the support. The simulation indicated that no substantial conformational changes were caused upon immobilization of both mutants. Adapted with permission from reference 52. Copyright (2017) Royal Society of Chemistry.

Enzyme encapsulation

Enzyme encapsulation is defined as a procedure that allows enzyme entrapment in three-dimensional frameworks. Enzyme encapsulation does not require any chemical modification of the enzyme. The choice of the material for the encapsulation of the enzyme is crucial as it must enable the substrate and reaction products to diffuse while reducing any enzyme leach. Indeed, the main advantages of this approach are that the enzyme can be confined in a favourable environment, and that the risk of enzyme leaching is limited. Several materials such as polymer, sol-gel, liposomes, hydrogel, metal-organic framework and proteins cages allowed enzyme encapsulation.⁵³⁻⁵⁶

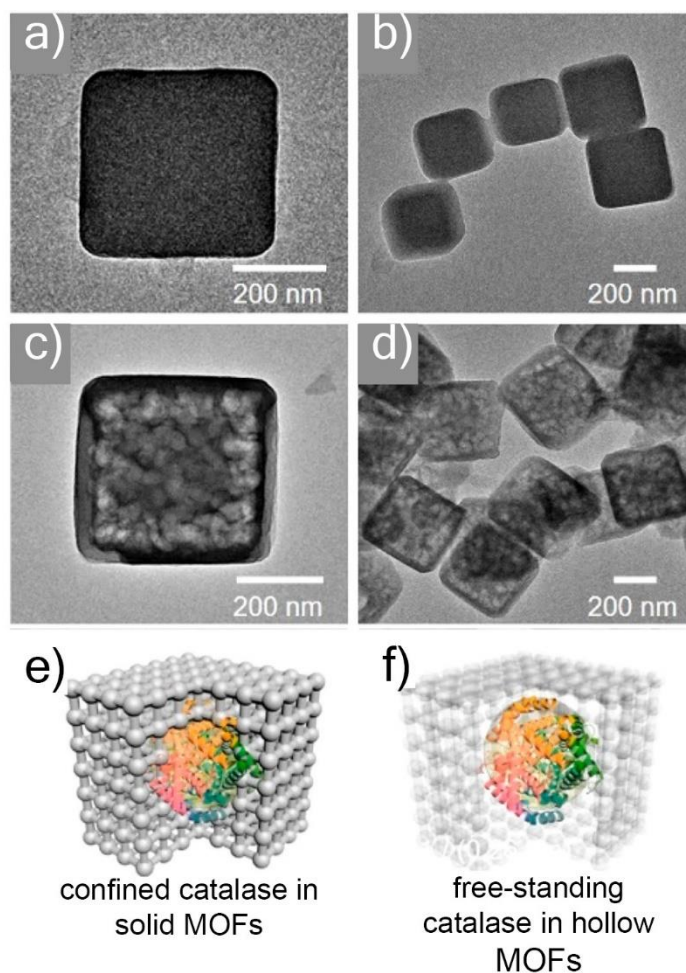


Figure 8. Structural characterization of MOFs and encapsulated catalase. Transmission electron microscopy (TEM) micrographs of encapsulated catalase in (a–b) solid and (c–d) hollow MOFs. Schematic illustration of catalase encapsulated in (e) solid and (f) hollow MOFs. Adapted with permission from reference 54. Copyright (2020) American Chemical Society.

Chen *et al.* recently reported an elegant approach for enzyme encapsulation in which the use of hollow metal–organic frameworks (MOFs) enabled the encapsulation of a catalase in a free-standing fashion (**Figure 8**).⁵⁵ The kinetic study of encapsulated catalase in the degradation of H₂O₂ showed that the maximum rate of reaction was 10 times higher for the enzyme encapsulated in the hollow MOF (and so comparable to that of the soluble enzyme) than for the enzyme in the solid MOF. These results were explained by the reduced number of interfacial interactions between the enzyme and the hollow MOF, which increased the enzyme's conformational freedom. The encapsulated catalase showed increased stability when treated with urea 8M and proteinase K, which typically lead to the enzyme inactivation.⁵⁵

Sol-gel matrixes (e.g. silica, alumina, titania) have been widely used for encapsulating enzymes, due to the mild experimental conditions of the sol-gel synthesis and to the possibility to tailor the properties of the material, thus offering the possibility to tune the catalytic activity of the encapsulated enzymes.⁵⁷ For example, whereas the usage of Si-(OCH₃)₄ sol gel matrix for the encapsulation of a lipase dramatically reduced the enzyme activity, the replacement of one methoxy function in the silica sol-gel matrix with a methyl function in CH₃-Si-(OCH₃)₃, increased the enzyme esterification activity up to 1300% in comparison to that of the soluble enzyme.⁵⁸ Sol-gel matrices have proven to be effective also for improving the stability of enzymes in harsh conditions.⁵⁹ Luckarift *et al.* reported on the encapsulation of a butyrylcholinesterase inside silica nanospheres which allowed 100% of enzyme activity to be retained upon storage of the enzyme at 25°C for 30 days, whereas its soluble counterpart was inactive after only eight days. Due to its improved stability and high activity the encapsulated enzyme was used in a flow-through system where it hydrolyzed the substrate over 1000 column volumes of substrate solution.⁵³ Similarly, Zhao *et al.* showed that a lipase encapsulated in a silica shell retained 87% of activity upon storage at 70°C for 2 hours, whereas the soluble enzyme was fully inactivated.⁶⁰ Interestingly, enzyme encapsulation strategy has been used to

design co-enzyme systems for cascade reactions. The advantage of confining two or more enzymes by encapsulation is that it enhances enzyme local concentration, which is important in cascade reactions. Kim *et al.* reported the co-encapsulation of formate dehydrogenase and mannitol dehydrogenase inside pluronic-based nanocapsules. The encapsulated system was then applied for the production of D-mannitol, in a cascade reaction. Up to 10 times more D-mannitol was produced using the co-encapsulated enzymes than using the mixture of soluble enzymes.⁶¹

Those and other reports, show that tuning the properties of the encapsulating materials allows the enzyme environment to be modified, with direct effects on enzyme properties.⁶²⁻⁶⁴ The influence on the enzyme properties by the surface chemical functionality, charge, and topography of the encapsulating materials are highlighted in section 3.

Surface properties of support materials for enzyme immobilization

Wolfgang Pauli, said “*God made the bulk; the surface was invented by the devil.*”⁶⁵ With this expression, Pauli was referring to the profoundly different nature of surfaces (interfaces) compared with the bulk material. Due to the complexity of interfaces the design of the procedure and of the materials to select for immobilizing enzymes is challenging. Therefore, the choice of the most appropriate strategy to use is often made without any prediction of how the properties of enzymes might change upon immobilization. However, the choice of the support material can be made based on considerations of its superficial chemical and physical properties.

A wide range of materials have been used for enzyme immobilization ranging from organic polymers^{26, 66-69} (e.g. poly(vinylamine), polyethylene glycol, poly(ethylene oxide), poly(N-isopropylacrylamide)) to inorganic⁷⁰⁻⁷³ such as sol gel materials,⁷⁴⁻⁷⁶ and biopolymers (e.g. cellulose, collagen, chitin).⁷⁷⁻⁸⁰ Considering the diverse properties of such materials (e.g.

hydrophobicity, hydrophilicity, surface charge, structure), the different interactions occurring between enzymes and the surface of the support material are crucial in determining the final catalytic activity, stability and structural properties of the supported enzymes.

It has been reported that there is a structurally ordered layer of water molecules at the solid-liquid interface that extends over 10 Å from the support surface.⁸¹⁻⁸² Due to its highly organized structure, this hydration shell behaves as a viscous liquid, reducing the conformational flexibility of the enzyme and thus limiting the risk of protein unfolding or aggregation.⁸¹ To study the mechanism of adsorption of enzymes on the surface of a solid material, through the water layer present at the surface, MD simulations have been performed on generic short peptides (**Figure 9**).

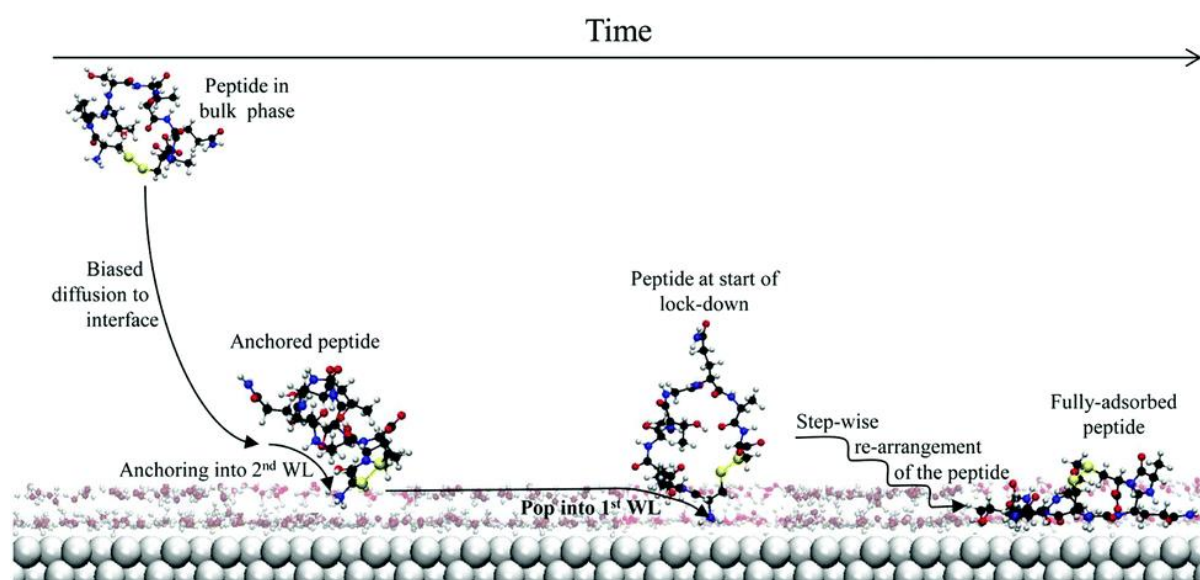


Figure 9. Model of peptide anchoring mechanism on the surface of a solid support. Firstly the peptide diffuses toward the solid surface. Secondly, due to hydrophobic interactions with the surface or to hydrophilic interactions with the second water layer (WL) the peptide diffuses to the first WL. Finally, structural rearrangements of the peptide allow the adsorption of the peptide onto the solid surface. Reproduced with permission from reference 81. Copyright (2017) Royal Society of Chemistry.

The simulations suggest that this water layer has a layer by layer structure, in which one layer faces the bulk solution, while the inner layer intimately shields the support surface. Therefore, the peptide adsorption on a solid surface occurs when the peptide first, diffuses to the solid surface, from the bulk solution and then by crossing those two hydration layers. The driving

forces for the diffusion from the outer layer to the inner one, depend mainly from the type of interactions with the solid surface and with the hydration shell. Indeed, the formation of hydrophobic interaction between the hydrophobic moieties of the peptide and the solid surface, or the H-bond formation between the hydrophilic residues on the peptide and the water molecules shielding the surface of the support are the driving forces leading to the peptide anchoring on the surface. The peptide is finally anchored to the surface due to its conformational changes, caused by the introduction of the amino acids residues into the first water layer at the solid surface.⁸¹

When such modelling approach is applied on proteins, having more amino acid residues and more complex structures than the peptide considered in this study, their interactions with the support and with the solvent are difficult to predict. You *et al.* showed that the immobilization of an α -chymotrypsin on a gold support with a hydrophilic surface resulted in a remarkable loss of activity in comparison to the enzyme immobilized on a hydrophobic surface.⁷¹ This loss of activity was the consequence of a distortion of the protein structure that occurred because of competition for hydrogen bonding by hydrophilic residues with both the support and the water. By contrast, Orrego *et al.* reported that the thermal stability of the penicillin G acylase was 280 times higher when the enzyme was immobilized on a methacrylate support treated with aspartic acid than when it was on the support without the hydrophilic functionalization.⁸³ This result suggested that the hydrophilic interactions of the enzyme with the support were crucial on reducing the risk of protein denaturation caused by the temperature.

The charge on the surface of the support material is a relevant parameter for enzyme immobilization. The charged amino acids on the surface of the enzyme interact electrostatically with the charged surface of the support. The repulsion or attraction of these residues may lead to the distortion of part or of the entire enzyme structure.⁸¹ As an example, immobilization of a cytochrome protein on both positively or negatively charged gold nanoparticles led to the

denaturation of the protein. This result was due to the electrostatic interaction of charged amino acids next to a specific cysteine (i.e. C102) with the charged moiety of the ligands on the surface of the support.⁸⁴ By contrast, immobilization of a glucoamylase and a β -glucosidase onto a polystyrene support that was functionalized with negatively charged groups resulted in a massive immobilization yield (600 mg enzyme per gram of support material) and the full retention of the enzymes catalytic activity.⁸⁵

An increase in surface area and surface curvature of the support contributes on reducing the frequency of protein-protein interactions, thus reducing enzyme crowding phenomena at the surface of the support material.⁸⁶⁻⁸⁷ Enzyme crowding can cause distortion and unfolding of the enzyme structure. Asury *et al.* studied the immobilization of four enzymes on single-walled carbon nanotubes, which offer the potential to stabilize the proteins at high temperatures as an alternative to immobilization on flat supports.⁸⁸ They found that the enzymes immobilized on single-walled carbon nanotubes had higher activity and stability than those immobilized on flat surfaces, due to the curvature of the support, which suppresses lateral protein-protein interactions.

The topography of the support surface can also influence the retention of the enzymatic activity upon immobilization.⁸⁷ The presence of regularities on the surface of the support had a positive effect on the retention of enzyme activity upon immobilization.⁸⁹⁻⁹⁰ Enzyme immobilization on polymeric supports with an isotactic and syndiotactic surface retained more catalytic activity than on less ordered support surfaces (coated with atactic polymers). Immobilization on a regular surface was hypothesized to occur with fewer contacts between the enzyme and the support, thus avoiding structural re-arrangements of the protein.⁸⁷

Silica based materials

The choice of the support for enzyme immobilization must also take into account the compatibility of the material with the enzyme and with the immobilization strategy, its chemical and thermal stability, and its capability of regeneration and reusability for more cost-effective processes.⁹¹ In the research of suitable supports for enzyme immobilization, silica and gold nanoparticles (AuNPs) are preferred. This section focuses on silica-based materials, whereas AuNPs are described in Chapter 4, where a hybrid system including enzyme and AuNPs is described.

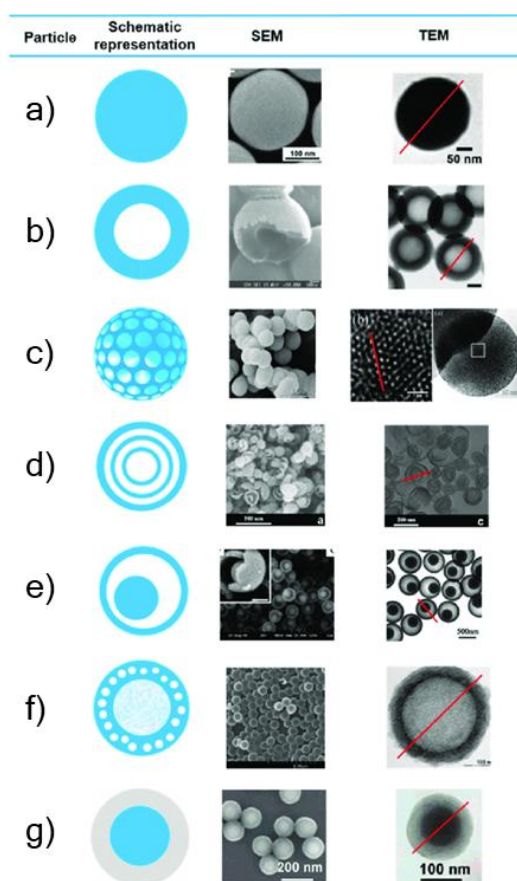


Figure 10. Silica particles in various morphologies. Schematic representations (left column) of silica particles and their characterization with scanning (middle columns) and transmission (right column) electron microscopy (SEM and TEM). The morphology nomenclature for these particles is defined as (a) nonporous/dense; (b) hollow; (c) ordered mesoporous; (d) multi-shell; (e) core in hollow (rattle/egg yolk); (f) hollow with hierarchical pores; (g) core-shell. Adapted with permission from reference 92. Copyright (2016) American Chemical Society.

The wide use of silica-based materials for enzyme immobilization is due to their low production cost and high thermal and mechanical stability.⁴⁶ Sol-gel methods have been developed to synthesize silica supports with different structures, ranging from dense silica particles to mesoporous ones and finally to hollow silica particles (**Figure 10**).⁹²

Dense particles are produced by Stöber synthesis in aqueous solution using tetraethoxysilane (TEOS), ammonia and ethanol (**Figure 11**).⁹³ Variation of the silane/solvent ratio allows the particle size, shape and uniformity to be fine-tuned.⁹⁴ In this way, particles can be synthesized by means of a template-free synthesis that nevertheless allows for control of their properties. Silica-dense particles were proven to be a valid support for the production of highly active and recyclable biocatalysts.^{53, 95}

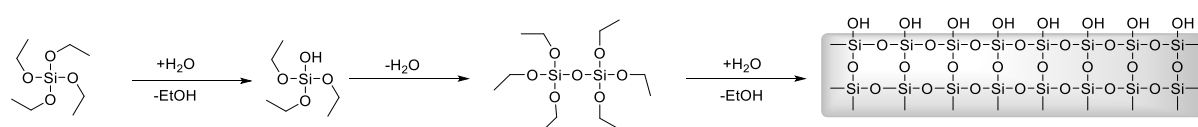


Figure 11. Stöber synthesis scheme. The hydrolysis of tetraethoxysilane (TEOS) is followed by the polycondensation of the hydrolyzed TEOS.

Mesoporous and hollow silica particles are produced in the presence of a template, which controls the pore size and the hierarchical structure of the final material.⁹⁶⁻⁹⁷ The advantage of using mesoporous and hollow silica supports is their high surface area and large pore volume. Besides their use for catalysis, drug delivery, gas separation, and pollutant absorption,⁹⁸ they have proven to be valuable supports for producing bioconjugated enzymes due to their higher loading capacities. Wang *et al.* produced a supported horseradish peroxidase on dendritic mesoporous silica, which offered a significant signal amplification for use in enzyme-linked immunosorbent assay (ELISA) and a sensitivity that was 10⁴ times higher than that of the classical ELISA.⁹⁹ In another example hollow silica particles were used to encapsulate a glucose oxidase (GOx) and magnetite nanoparticles (Fe₃O₄) (

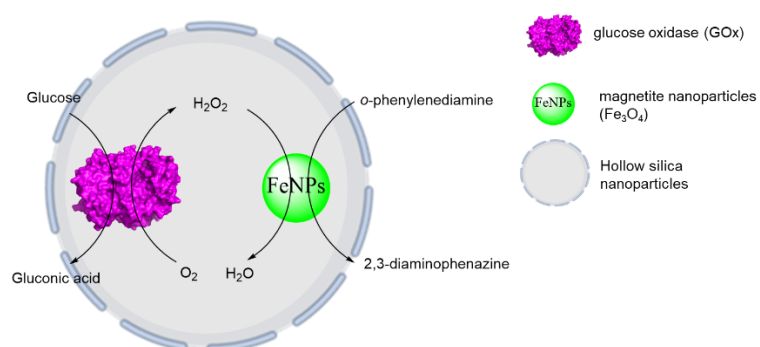


Figure 12).¹⁰⁰ The hollow particles were used as a microreactor for the cascade reaction of oxidation of glucose to gluconic acid and hydrogen peroxide (H_2O_2) by the GOx, followed by the oxidation, with H_2O_2 , of the *o*-phenylenediamine to 2,3-diaminophenazine by Fe_3O_4 .¹⁰⁰ The catalytic constant k_{cat} was 14 times higher when the two catalyst were confined inside the HSPs in comparison to the soluble counterparts.

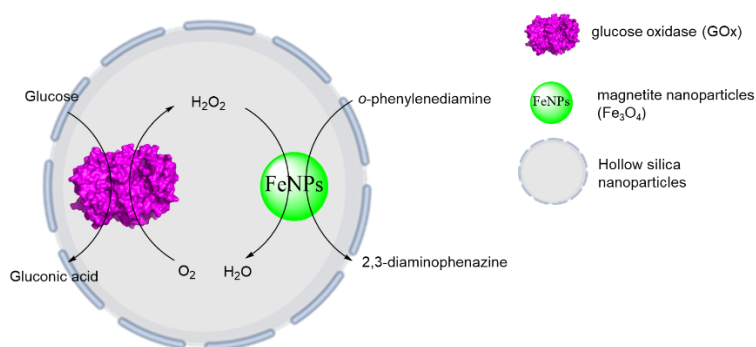


Figure 12. Schematic depiction of cascade reaction inside hollow silica nanoparticles (HSNPs). The cascade reaction involving the glucose oxidase (GOx) and the magnetite nanoparticles was performed inside hollow silica nanoparticles, where both the enzyme and the inorganic catalyst were confined. The catalytic constant k_{cat} was 14 times higher when the two catalyst were confined inside the HSPs in comparison to the soluble counterparts. Adapted with permission from reference 100. Copyright (2020) American Chemical Society.

In addition, silica materials enable efficient enzyme immobilization due to the potential to chemically modify the surface of the material to enable a wide range of functionalities. As discussed in the previous section, this is crucial for the efficiency of the enzyme immobilization

strategy and for the final properties of the supported enzyme. Pina *et al.* studied the effect of different surface moieties (e.g. amine, pyridine, carboxylic acid, alkane and isocyanate) of a mesoporous silica support on the immobilization yield and on the activity of a tyrosinase, which is the enzyme responsible for food browning.¹⁰¹ The authors reported high loading capacity for all the support materials (100% immobilization yield), apart from the silica functionalized with carboxylic acid. However, enzyme inhibition was very low for all the materials studied. Interestingly, the authors discovered that the amine-functionalized silica was able to capture the oxidation product, thus delaying food browning for 90 minutes in the presence of oxygen.

Silica-supported enzymes have been investigated in biomedical engineering for use in a wide variety of applications, ranging from drug delivery and biocatalysis,¹⁰² to cancer therapy¹⁰³ and biosensing.¹⁰⁴ Therefore, one last aspect to take into consideration when using silica materials in enzyme bioconjugation is their biocompatibility. Li *et al.* reported on the cytotoxicity in macrophages of Stöber synthesized silica particles with different surface modification such as NH₂, COOH and PEG.¹⁰⁵ The cytotoxicity of the silica particles was lowest for COOH modification and highest for PEG modification. In general, the replacement of silanol groups reduced the cytotoxicity of the particles in comparison with the unfunctionalized ones. Indeed, the presence of silanol groups on the surface of silica particles seems to be linked to membranolytic processes in the cells, due to the interactions between SiO⁻ and the cell membrane.¹⁰⁶ Other properties of silica particles (e.g. size and shape) have been investigated in relation to their toxicity and provide a guide for further consideration.¹⁰⁷⁻¹⁰⁸ Despite extensive efforts to study this topic, the biocompatibility of silica materials is still under consideration and the results remain controversial, thus preventing a general conclusion. This lack of clarity is due to the availability of multiple support structures, sizes and functionalities, along with various doses and cell types, which have led to a heterogeneous set of results.¹⁰⁹

3 MODIFICATION OF THE ENVIRONMENT OF IMMOBILIZED ENZYMES

Enzymes are open systems exchanging mass, energy and information with their surrounding environment within confined areas inside the cell.¹¹⁰ Enzymes are able to recognize their substrate, distinguishing it among many. Finally, they can exchange the product of substrate conversion with the environment. In this process, the conformational flexibility of enzymes and the modification of the substrate structure allows for enzyme-substrate recognition (e.g. lock-and-key, induced fit model),¹¹¹ and lowers the energetic barrier for substrate conversion. Enzymes respond to stimuli in the environment, such as the concentration of the target substrate, pH, temperature, ionic strength, the type of solvent, and the presence of inhibitors or surfactants. Consequently, enzymatic processes are triggered or hindered by the interactions between enzymes and the environments in which they are located.¹¹⁰

When an enzyme is confined to a surface, by immobilization, or inside a 3D network, as in the case of encapsulated enzymes, the environmental factors described above might be different at the interface than in the bulk. An immobilized enzyme is indeed part of a specific nano-environment, which affects its structure, turnover, stability and selectivity.¹¹² In this context, a rational understanding of immobilized enzyme properties can be challenging. With the aim of highlighting the influence of the enzyme environment on enzymatic catalysis, the next two sections focus on factors affecting the interface of enzymes confined on a surface and inside a 3D network.

Interfacial environment

Heterogeneous biocatalysis, performed by immobilized enzymes, occurs when a substrate diffuses from the bulk to the nano-environment of the biocatalyst. The properties of the substrate and of the components of the bulk (e.g. solvent, pH, ions, surfactants) are therefore important.

Partitioning of the substrate between the bulk solvent and the interface can take place due to charges at the support surface or to its hydrophobicity.¹¹³⁻¹¹⁴ If the substrate charge is the same as the net charge of the support on which the enzyme is immobilized, the partition effect is unfavourable to binding. Therefore, to enable conversion of the substrate, the substrate's affinity for the interface, rather than for the bulk, has to be enhanced. A kinetic study of the conversion of a substrate with positive, negative or neutral charge by α -chymotrypsin revealed that the enzyme immobilized on amino acid-functionalized gold nanoparticles showed significant selectivity for the positively charged substrate, whereas the soluble enzyme converted all three substrates with comparable activity (**Figure 13**).¹¹⁵ The increase in selectivity by the immobilized α -chymotrypsin was driven by the higher affinity of the substrate for the charged layer at the solid-liquid interface (**Figure 13**).

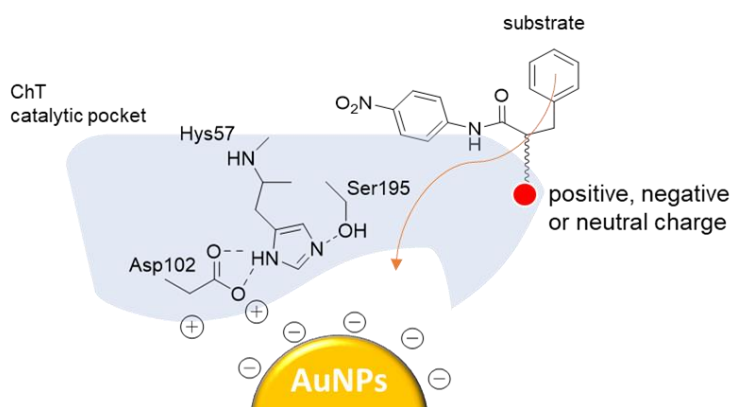


Figure 13. schematic depiction on catalytic pocket of α -chymotrypsin (ChT) immobilized on gold nanoparticles (AuNPs). The charged substrate enters in the catalytic pocket (Asp102-Hys57-Ser195) only if its charge is positive (red circle) due to attraction with the charges on the surface of AuNPs. Adapted with permission from reference 115. Copyright (2006), American Chemical Society

When enzymes are immobilized on supports that are able to attract ions, specifically hydrogen ions, a buffered area with different pH than that of the bulk might be established at the interface. Therefore, the pH range in which immobilized enzymes are active can be modified or extended.^{80, 116} Several reports have shown a change in the optimum pH of enzymes upon immobilization. For example, an enzyme immobilized on polycationic supports (e.g. polyethylenimine) had a more acidic optimum pH than the free enzyme, while the opposite was

true when it was immobilized on polyanionic supports.⁸⁷ Therefore, a rational design of the interface charge might provide the opportunity to tune enzymatic activity at different pH values.

Enzyme environment inside a 3D network

When an enzyme is shielded, encapsulated or entrapped in a porous support, the catalytic reaction occurs in a confined environment.

In such cases, the mass transfer from the bulk to the confined enzyme becomes important. In this context, substrates must diffuse through the encapsulating support material, or shield, where they are converted; finally, the product diffuses out from this confined system. The mass transfer occurs according to diffusion limits.¹¹⁷

When diffusion of the substrate or product is not a limiting factor, the ratio of surface area to volume of the shield can influence enzyme activity. Indeed, in low-volume systems, surface effects of the shield become significant.¹¹⁰ In such systems, interactions with the surface of the shield affect the structure of enzymes and therefore their catalytic properties.¹¹⁸⁻¹²⁰ Some meaningful examples of enzyme shielding and enzyme-shell interactions have been reported^{76, 121} Correro *et al.* provided an example of β -galactosidase immobilized on silica particles and embedded into an organosilica shield, including TEOS and (3-aminopropyl)triethoxysilane (APTES) (**Figure 14**).⁷⁵ The authors characterized the enzyme activity during the shielding process. Interestingly, the authors reported a dramatic drop of activity of the immobilized enzyme soon after shielding, followed by recovery of 68% of the enzyme activity 12 hours after shielding; the whole period involving the layer growth on the enzyme was named as curing time.

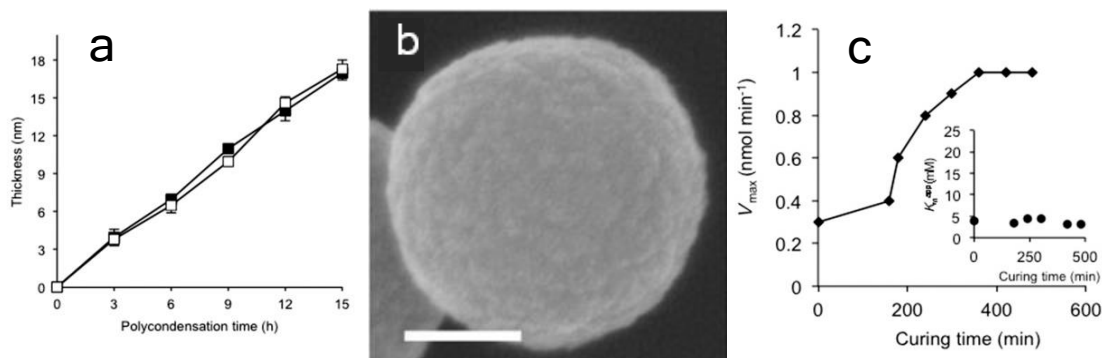


Figure 14. β -galactosidase encapsulated in an organosilica layer. (a) Kinetic of organosilica layer growth on a shielded β -galactosidase (white squares) and on bare SPs (black squares). The layer thickness was measured from SEM micrographs (b) of the shielded particles (scale bar is 200 nm). Increase of layer thickness of 1.2 nm h^{-1} was calculated. (c) A Michaelis-Menten study of the shielded β -galactosidase. Adapted with permission from reference 75. Copyright (2016) John Wiley and Sons.

The authors concluded that the shield initially interacted with the surface of the enzyme via hydrogen bonding and electrostatic interaction, thus limiting enzyme mobility. During the curing process, more Si-O-Si bonds were formed in the layer matrix. Consequently, the interactions of the layer with the enzyme surface were reduced. A Michaelis-Menten study of the encapsulated enzyme revealed an increase of the maximum velocity (V_{max}) of SP-enzyme during the curing. Those results suggested that the curing process, led to the increase of porosity of the organosilica layer, which allowed the enzyme to acquire a more favourable conformation. This increased enzyme flexibility and thus its activity. The immobilized β -galactosidase shielded with TEOS and APTES and with different moieties (e.g. propyl-, hydroxy-, benzyl-, etc) in the shield allowed to dramatically enhance the enzyme stability in different stress conditions (e.g. thermal treatment, in presence of denaturation agents such as sodium dodecyl sulphate and in presence of urea).⁷⁶

CHAPTER 2

OBJECTIVES OF THE RESEARCH

In a world confronting with serious environmental issues, the attention of scientists on greener and sustainable processes is exponentially arising. In this context, biotechnology and biocatalysis are of great value through the application of sustainable processes for the conversion of biomass into a wide range of compounds (e.g. ethanol, biofuels) and for the production of pharmaceuticals, food additives, detergents, vitamins, fragrances and fine chemicals with sustainable processes. Considering that enzymes are natural high-performing catalysts able to function in mild conditions and showing high selectivity, biocatalytic processes require less energy and produce reduced amount of by-products waste.

The implementation of strategies supporting the stability of enzymes under non-physiological conditions, or the production of new and improved enzymes, is a powerful asset in the biotechnology toolbox.

In the frame of this PhD thesis, the synthesis of enzyme-nanomaterial conjugates (i.e. immobilized enzymes) was the first step in the production of highly stable biocatalysts. This approach was then followed by supramolecular enzyme engineering, which supports the modification of the enzymatic environment such that fine tuning of the enzyme properties can be obtained, while preserving the original genetic and chemical properties of the protein. The main questions driving the research work related to the means by which the local environment of the enzyme could affect its structure, catalytic function and stability, and how could this local environment be redesigned to enhance the enzyme's catalytic properties in harsh conditions.

To address to these questions, the research was firstly implemented with the aim of endowing non-enantioselective enzymes with enantioselectivity. Specifically, the objective was to convert non-enantioselective and highly promiscuous enzymes with enantioselectivity, with no major changes in the enzyme promiscuity. With the objective of tuning the interaction of the

enzyme with various chemical moieties at the surface of the protective layer, its composition was controlled, consequently inducing a change in the enzyme catalytic properties.

The research was then directed to the development of a new method for the production of biocatalysts with extremophilic properties. The rational design of the interface between different enzymes and inorganic materials aimed to confer cryogenic properties to mesophilic enzymes. Specifically, the objective of the work was the production of enzymes showing improved activity at low temperatures (below 20°C).

Ultimately, the methods described in this PhD thesis were applied to structurally diverse enzymes aiming at testing the versatility of this approach.

CHAPTER 3

TUNING THE ENANTIOSELECTIVITY

OF NATURAL PROMISCUOUS

ENZYMES

SUMMARY

In the present chapter, we reported a novel method for tuning enzyme properties based on the enzyme environment modification approach. The method, herein proposed, allows to confer stereoselectivity properties to highly substrates promiscuous and not enantioselective esterases while retaining a high degree of enzymes promiscuity. Esterases were immobilized on a silica support to stabilize and promote their enzymatic activity (**Figure 15**). Furthermore, an organosilica layer was grown at the surface of the immobilized enzyme in order to modify the catalytic environment of the esterase. The modulation of the enzyme enantioselectivity was achieved by tuning the organosilica layer composition. Moreover, high solvent stability of these novel biocatalysts was observed. Here, we propose an innovative approach for the fine tuning of catalytic properties of natural enzymes.

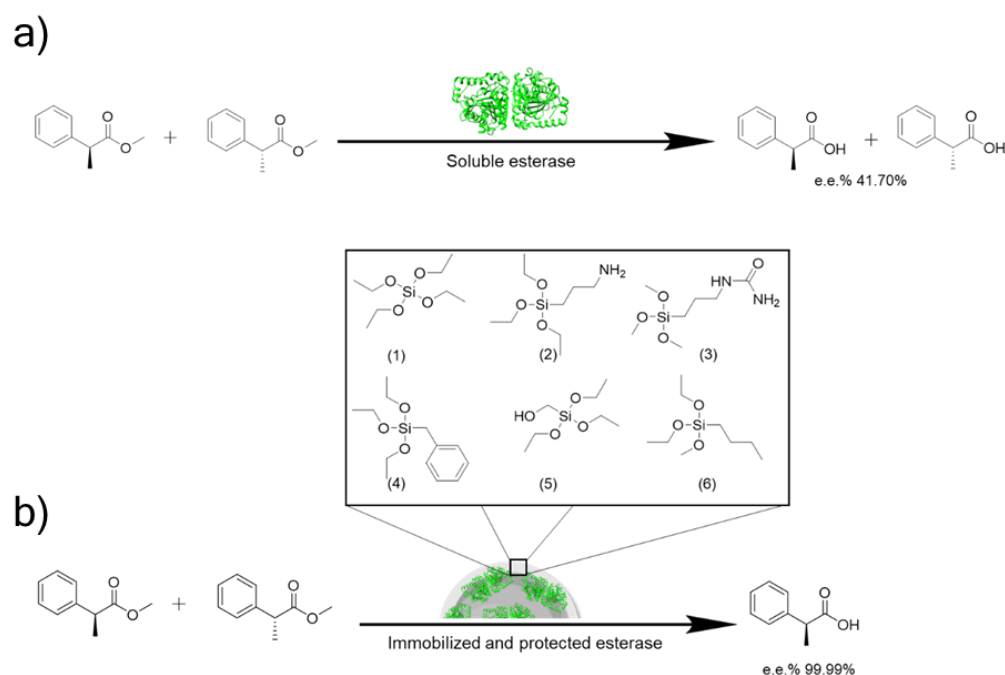


Figure 15. Schematic depiction of the strategy used to modify the enantioselectivity of esterases. While the (a) soluble esterase does not show enantioselectivity in the conversion of the methyl (*R/S*)-2-phenyl propanoate. (b) The immobilized and shielded enzyme shows improved enantioselectivity. In the box: Tetraethoxysilane TEOS (1), (3-aminopropyl) triethoxysilane APTES (2); 1-[3-(trimethoxysilyl)propyl]urea (3); benzyltriethoxysilane (4); hydroxymethyltriethoxysilane (5); and n-butyltriethoxysilane (6).

A short insight on the enzyme promiscuity will introduce the experimental work reported and investigated in a manuscript submitted for publication. Prof. Manuel Ferrer, Sandra Alonso, Isabel Cea-Rama are acknowledged for the production, crystallization and characterization of the esterases, and for the characterization of the activity of the biocatalysts produced in this work.

1 ENZYME PROMISCUITY

Despite the evolution process has led enzymes to develop high specificity and selectivity, in some enzymatic families promiscuous activities are commonly found.¹²²⁻¹²³ Promiscuous enzymes are classified as enzymes capable to convert “indiscriminately” a wide range of substrates (substrate promiscuity). Additionally, along with their native activity, promiscuous enzymes show one or more secondary activities (catalytic promiscuity).¹²⁴

Enzyme promiscuity may be related to the high enzyme conformation flexibility.¹²⁵ Honaker *et al.* investigated the relation between the substrate promiscuity and the structure flexibility of a glutathione S-transferases.¹²⁶ A differential scanning calorimetry (DSC) study revealed the presence of an α -helix covering the active site, which can assume different conformations. The flexibility of this motif in close proximity to the active site allowed binding a large number of substrates.¹²⁶ Enzyme promiscuity can also be attributed to specific properties of the catalytic centre, such as size, shape or functional groups.¹²⁷ It was shown that both catalytic and substrate promiscuity occur in enzymes with large active sites as they are able to accommodate structurally different substrates.¹²⁸⁻¹²⁹ In an interesting example, Albanese *et al.* reported that the presence of a lysine inside a hydrophobic pocket of the bovine serum albumin was responsible for the enzyme catalytic promiscuity in both water and in organic solvents.¹³⁰ Finally, it is also possible to induce enzyme promiscuity with various enzyme environmental conditions. The presence of organic solvents, cofactor or metal ions along with occurring

hydrophobic interactions with substrates, or the variation of temperature and pH, have been proven to have an effect on the enzyme promiscuity.¹³¹ For example, it was reported that the thymidine kinase from *Thermotoga maritima* shows high substrate specificity at 82°C but high promiscuity at 37°C.¹³²

Tuning the Properties of Natural Promiscuous Enzymes by Engineering their Nano-Environment

Carolina I. Giunta, Isabel Cea-Rama, Sandra Alonso, Manon L. Briand, Rafael Bargiela, Cristina Coscolín, Philippe F.-X. Corvini, Manuel Ferrer, Julia Sanz-Aparicio*, and Patrick Shahgaldian**

Keywords: nanoparticles, supramolecular engineering, enzymes, organosilica, biocatalytic promiscuity

2 ABSTRACT

Owing to their outstanding catalytic properties, enzymes represent powerful tools for carrying out a wide range of (bio)chemical transformations with high proficiency. In this context, enzymes with high biocatalytic promiscuity, are somewhat neglected. Here, we demonstrate that a meticulous modification of a synthetic shell that surrounds an immobilized enzyme possessing broad substrate specificity allows the resulting nanobiocatalyst to be endowed with enantioselective properties while maintaining a high level of substrate promiscuity. Our results show that control of the enzyme nano-environment enables tuning of both substrate specificity and, remarkably, enantioselectivity. Further, we demonstrate that our strategy of enzyme supramolecular engineering allows the enzyme to be endowed with markedly enhanced stability in an organic solvent (i.e., acetonitrile). The versatility of the method was assessed with two additional substrate-promiscuous and structurally different enzymes, for which remarkable improvements in enantioselectivity and stability were confirmed. We expect this method to open new avenues for the use of supramolecularly engineered promiscuous enzymes in industrially relevant biocatalytic processes.

3 INTRODUCTION

The natural evolution of enzymes that have undergone four billion years of stringent environmental stress conditions, has endowed these functional proteins with enhanced substrate- and reaction- selectivity along with high turnover rates.^{124, 133-134} By contrast, a limited number of enzymes that have been sheltered in favorable ecological niches have endured only limited environmental stress and thus have maintained the substrate and catalytic promiscuities of their progenitors.¹³⁵

From a molecular viewpoint, a high level of promiscuity is typically enabled by a voluminous biocatalytic active site that accommodates a large number of substrates. Large active sites also increase the substrate docking freedom and thus display limited stereoselectivity, which restricts the industrial use of promiscuous enzymes for example for the synthesis of chiral molecules.

Recent breakthroughs in protein engineering, through the development of rational design and directed evolution strategies, have provided scientists with efficient tools to improve enzyme properties.^{20, 136-139} When applied to promiscuous enzymes, protein engineering methods can enhance biocatalytic activity or introduce new-to-nature reactions.²⁰ For example, a promiscuous 4-oxalocrotonate tautomerase has been endowed, through mutability-landscape assessment and engineering, with the ability to perform unnatural Michael-type additions of aldehydes or ketones to various nitroalkenes.¹⁴⁰ Cytochrome P450 (P450) enzymes are widely used as biocatalysts for monooxygenation of various organic substrates, and they have been extensively engineered to control their biocatalytic activity.¹⁴¹ For example, a substrate-promiscuous P450 from *Bacillus megaterium* has been engineered to enable non-native substrates to be processed for the development of a novel semi-biosynthetic route for artemisinin production.¹⁴² An approach based on a literature-based cluster analysis along with

the use of a correlated mutational network, allowed to significantly improve the enantioselectivity of a promiscuous esterase from *Pseudomonas fluorescens*.¹⁴³ Recently, we engineered a promiscuous esterase with two catalytic active sites, one of which was chemically modified to catalyze oxidation and Friedel–Crafts alkylation reactions.¹⁴⁴

Enzyme properties may also be tuned by engineering enzyme microenvironments,¹⁴⁵ immobilization on solid supports, or encapsulation.^{3, 30} With the aim of combining immobilization and environment engineering, we previously reported a strategy for immobilizing and shielding enzymes within enzyme-thick and soft organosilica material, which resulted in the marked enhancement of resistance to denaturing stresses.⁷⁵⁻⁷⁶ The shield was designed so as to avoid reducing protein mobility while increasing enzyme stability in response to different stress conditions (e.g., high temperature, freeze-thaw cycles, urea or sodium dodecyl sulfate treatment).

Enzyme immobilization typically results in enantioselectivity impairment,³² although, few reports have demonstrated enantioselectivity enhancement via enzyme encapsulation or immobilization.^{32, 146} To the best of our knowledge, no chemical strategy enabling enantioselectivity to be conferred on non-enantioselective enzymes has been reported.

Here, we report on the transformation of three substrate-promiscuous and non-enantioselective ester hydrolases (EHs) into highly enantioselective yet promiscuous biocatalysts. This was achieved by supramolecularly engineering the enzyme nano-environment to create a complex network surrounding the enzyme. With the approach described in this work, we demonstrate that the need for a compromise between substrate promiscuity and stereoselectivity can be bypassed by chemically modifying the local nano-environment of the enzyme.

4 RESULTS AND DISCUSSION

Synthesis and structural study

As a first model enzyme, we used a serine ester hydrolase isolated from the metagenomic DNA of microbial communities inhabiting the chronically polluted seashore area of Milazzo harbor in Sicily (Italy), referred to as EH₃ (GenBank acc. no. KY483645). In a recent study, EH₃ was identified, among 145 ester hydrolases, as one of the enzymes with the broadest substrate spectrum when tested with a set of ca. 100 chemically and structurally different esters; this was attributed to its voluminous active site (effective volume of 200 Å³).¹²⁸ EH₃ hydrolyses 71 esters, with glyceryl tripropionate (k_{cat} : 28.84 ± 0.4 s⁻¹) serving as the best substrate. As it is highly substrate-promiscuous, EH₃ did not show enantioselectivity when tested with chiral esters.¹²⁸

The molecular structure of EH₃, solved by single-crystal X-ray crystallography, revealed that the enzyme (**Figure 16** and **Table 4 Annex**) has two domains: a catalytic α/β hydrolase fold, typical of the hydrolase superfamily; and a cap domain on top of the catalytic triad (Ser192, Asp291, His321), which regulates substrate access (**Figure 47 Annex**). The polypeptide chain is highly flexible at the part of the cap domain comprising $\alpha 1$ and $\alpha 2$, as indicated by the high B-factor values (**Figure 47 Annex**). Moreover, EH₃ has three tunnel-like accesses to reach the catalytic Ser192 (**Figure 16**). Two cavities opposite one another are long tunnels for the acyl and the alcohol moieties, while a third cavity is believed to accommodate substrates with branched acyls as triglycerides. In order to confirm this assumption, EH₃ crystals were soaked in a solution containing butyl 4-nitrophenylhexyl phosphonate (B-4NHP), an esterase suicide inhibitor.

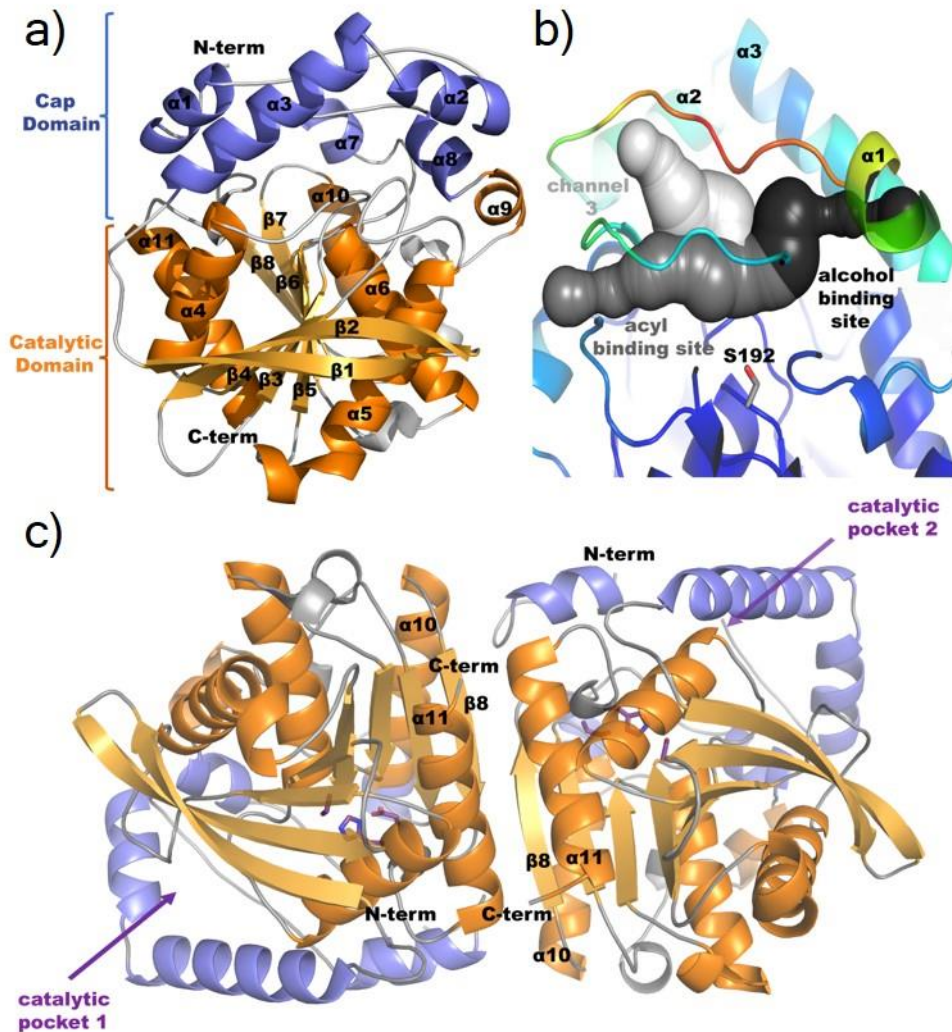


Figure 16. Crystal structure of EH₃. (a) Folding of the subunit showing the catalytic α/β hydrolase domain (orange), comprising six α -helices and eight β -strands, of which only $\beta 2$ is antiparallel. The cap domain (purple) involves five α -helices: $\alpha 1$ (Pro17–Ala25), $\alpha 2$ (Arg37–Asn45), $\alpha 3$ (Pro47–Met63), $\alpha 7$ (Pro234–Asn239) and $\alpha 8$ (Gln250–Tyr255) (b) The channels providing access to the catalytic Ser192, as calculated with CAVER.¹⁴⁷ The acyl and alcohol binding sites are labelled. A third channel can be occupied by substrates with branched acyls. The polypeptide chain is colored in a rainbow code according to the B-factor values, from blue (low) to red (high); a very flexible loop linking $\alpha 1$ to $\alpha 2$ is essential in delineating the binding channels. The view is rotated 180° with respect to the view shown in (a) for a better view of the channels. (c) Homodimer, with the same coloring as in (a), showing the catalytic triad as sticks. Interaction between subunits occurs mostly through $\beta 8$, with additional contributions from the preceding and following helices ($\alpha 10$, $\alpha 11$). Both subunits are related by a two-fold axis that is perpendicular to the view shown and situates the two active sites on opposite faces of the dimer.

The structural study of the phospho-ester-inhibited enzyme confirmed that this derivative occupies the acyl and alcohol binding sites. It mimics the tetrahedral intermediate of the reaction, as observed in classical phosphonate transition state analogues where the oxoanion is stabilized by Gly112 and Gly113 (**Figure 47 Annex**).¹⁴⁸ Like other homologues within family

IV of esterases, EH₃ is a homodimer with approximate dimensions of 8.0 x 5.0 x 4.0 nm and subunits related by a two-fold axis of symmetry, which situates the corresponding access to both active sites on opposite faces of the dimer (**Figure 16**).

EH₃ was immobilized on the surface of amino-modified silica particles (SPs) of 314 ± 7 nm diameter using glutaraldehyde as a crosslinker, according to an established procedure.⁷⁵ The enzyme immobilization occurred via the formation of imine bonds between glutaraldehyde and lysine (Lys) residues in the protein. The crystal structure of EH₃ revealed the absence of Lys residues in the vicinity of the active site (**Figure 48 Annex**), ensuring, in principle, immobilization without a major detrimental effect on the enzyme active site. Most Lys residues are located in one “hemisphere” of the dimer, so one can assume that this “hemisphere” is the region linked to the silica particle surface. However, it is challenging to predict the specific Lys residues involved in the binding; they could be very exposed residues, such as Lys100, or many proximal Lys residues in a zone on the surface, which therefore would have a higher binding efficacy.

The immobilization procedure was optimized to allow an immobilization yield of 87% (**Figure 49 Annex**), which represented 31 µg of protein per mg of silica. Next, the EH₃-immobilized particles (hereafter referred to as EH₃-SPs) were further processed in order to shield the enzyme in a protective layer of controlled thickness and composition (**Figure 17**). From the protein structure, and assuming the preferred orientation of the enzyme with regard to the silica surface, we estimated that a layer of 5 nm would cover the immobilized enzyme. For the protective building blocks, we initially used a precursor of inorganic silica (tetraethyl orthosilicate, TEOS) and 3-aminopropyl-triethoxysilane (APTES) (**Figure 17**) at varying ratios [TEOS/APTES (T/A); 1/1, 4/1, 6/1 and 10/1 (mol:mol), for samples EH₃-T/A_[1/1], EH₃-T/A_[4/1], EH₃-T/A_[6/1] and EH₃-T/A_[10/1], respectively]. Furthermore, organosilanes with different

organic moieties were used; namely n-butyltriethoxysilane (Bu), benzyltriethoxysilane (Bz), hydroxymethyltriethoxysilane (Hm) and 1-[3 (trimethoxysilyl)propyl]urea (Ur).

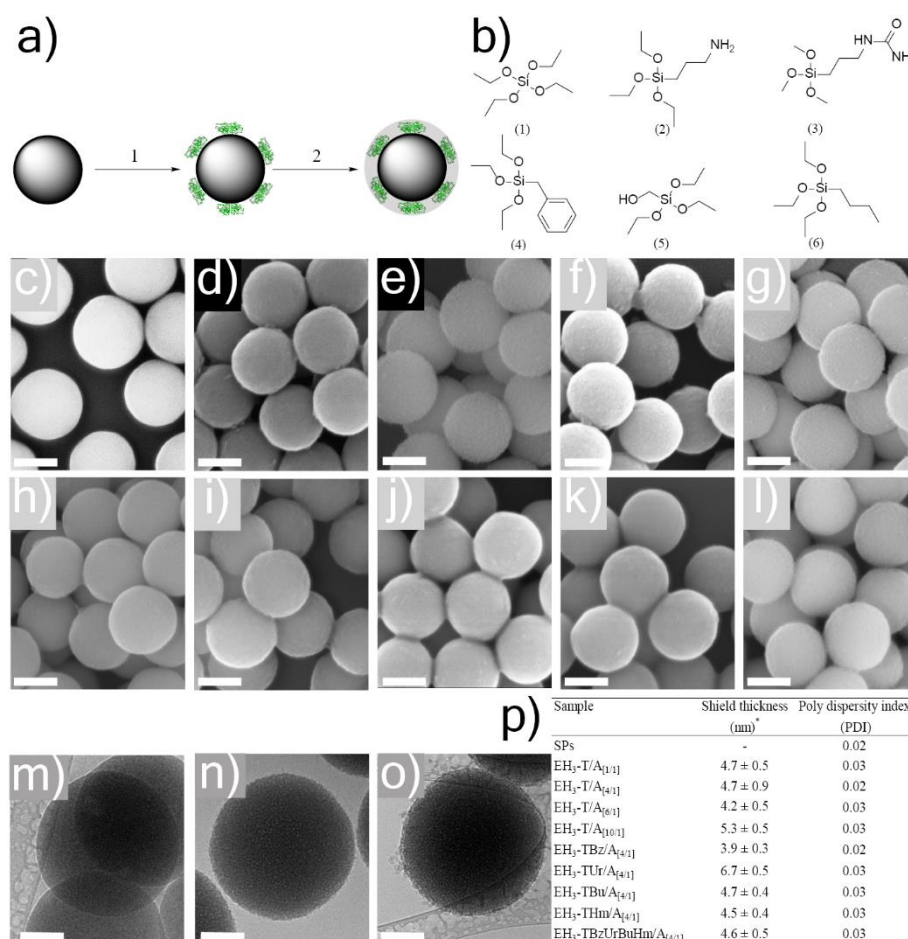


Figure 17. Nanobiocatalyst design, synthesis and characterization. (a) Schematic representation of EH₃ immobilization and protection in an organosilica layer of controlled thickness. The growth of this layer occurs through self-sorting and poly-condensation of hydrolyzed tetraethyl orthosilicate (TEOS) and organosilanes. (b) Molecular structures of the building blocks used in the protection layer formed by TEOS (1) (denoted as T); (3-aminopropyl)triethoxysilane (2) (APTES; denoted as A); 1-[3-(trimethoxysilyl)propyl]urea (3) (Ur); benzyltriethoxysilane (Bz) (4); hydroxymethyltriethoxysilane (Hm) (5); and n-butyltriethoxysilane (Bu) (6). Scanning electron microscopy (SEM) micrographs of (c) bare silica particles (SPs), (d) EH₃-T/A_[1/1], (e) EH₃-T/A_[4/1], (f) EH₃-T/A_[6/1], (g) EH₃-T/A_[10/1], (h) EH₃-TBz/A_[4/1], (i) EH₃-TUr/A_[4/1], (j) EH₃-TBu/A_[4/1], (k) EH₃-THm/A_[4/1], and (l) EH₃-TBzUrBuHm/A_[4/1]. Scale bars of SEM micrographs represent 200 nm. Cryo-EM micrographs of (m) bare SPs used as support for the biocatalyst, (n) EH₃-SPs, and (o) EH₃-T/A_[4/1]. Scale bars of cryo-EM micrographs represent 100 nm. (p) Shield thicknesses (nm) ± standard error and polydispersity indices (PDI). PDI was calculated as the ratio of the standard deviation σ and the diameter mean (\bar{d}) of the shielded particles (σ/\bar{d}). Standard error is calculated as $\sigma((\bar{d}_{\text{bare}} - d_{\text{shield}})/2) / \sqrt{n}$ where n is the number of measured particles. * is referred to 3h layer growth.

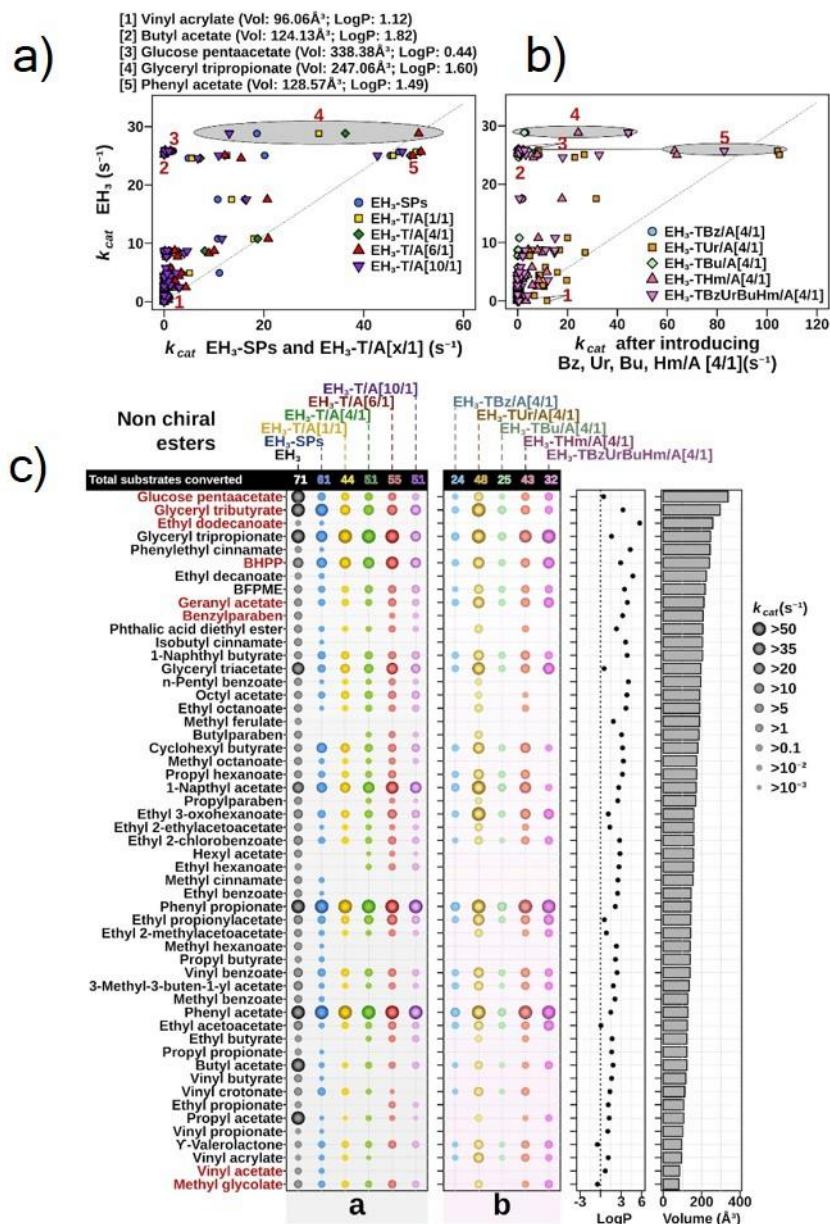
The organosilane building blocks were selected to enhance hydrophobic effects, H-bonding, π - π , and electrostatic interactions with the surface of the enzyme, respectively. A series of particles with layers of different chemical composition were synthesized accordingly (EH₃-TBz/A_[4/1], EH₃-TUr/A_[4/1], EH₃-TBu/A_[4/1], EH₃-THm/A_[4/1], and EH₃-TBzUrBuHm/A_[4/1]). For consistency, the ratio of TEOS organosilane:APTES was maintained at 4:1 (**Table 5 Annex**). All samples were reacted for 3h with the respective silane mixture to produce the desired 5 nm organosilica shield, which was then characterized using scanning electron microscopy (SEM) and cryo-transmission electron microscopy (TEM) (Figure 2 c-o).

Particles characterization showed that the starting SPs displayed a smooth surface (Figure 2c), were monodisperse in size with an average diameter of 314 nm and had a polydispersity index (*PDI*) of 0.02. All EH₃-SPs that were reacted with organosilanes had a larger diameter, with values ranging from 322 nm to 327 nm, consistent with the growth of an organosilica layer. Those values correspond to protection layers with thicknesses of 4 nm to 7 nm, confirming the shielding of the immobilized EH₃ enzyme (**Figure 17**). Further, while the surface of the newly grown layers appeared to be slightly rougher than the starting SPs, the increase in diameter did not involve major changes in the *PDI*, which remained low with values ranging from 0.02 to 0.03. The cryo-EM results (**Figure 17**) are in good agreement with the SEM observation. Interestingly, EH₃-SPs appeared somewhat rough, presumably owing to the presence of the enzyme on the surface of the SPs. The thin protective layer on EH₃-T/A_[4/1] was observed as a layer of lower electron density than the core of the SPs.

Substrate specificity and catalytic turnover study

To assess the influence of immobilization and shielding on the substrate specificity and catalytic turnover of the tested EH₃, the EH₃-SPs and the different shielded particles, we systemically analyzed catalytic constants values (k_{cat}) of the systems produced using a series

of 98 carboxylic ester substrates by means of a high-throughput pH indicator assay in 384-well plates. The acid produced after ester bond cleavage by the hydrolytic enzyme induced a colour change in the pH indicator that was measured spectrophotometrically at 550 nm.¹⁴⁴



As reference, we also measured the activity of the soluble enzyme (

Figure 18). The esters, their main physicochemical properties (volume, hydrophobicity and molecular weight) and their biocatalytic conversion rates are listed in **Table 6** (Annex).

We focused first on the maximum catalytic turnover and overall substrate spectra (

Figure 18a and **b**). Whereas soluble EH₃ can transform as many as 71 substrates with (highest k_{cat} of 28.84 s⁻¹), the substrate spectrum of EH₃-SPs was reduced to 61 substrates (absence of activity was defined as at least two-fold background signal).¹²⁸ This reduction can be reasonably attributed to a lower enzyme flexibility at the cap domain when it is immobilized on a solid support, resulting in a more rigid active site that is unable to accommodate as many substrates as its soluble counterpart. As observed previously for other enzymes, the presence of the shielding layer reduced the rate of hydrolysis for most substrates, while retaining or slightly increasing the k_{cat} for a few substrates up to ca. 47.07 s⁻¹, a value slightly higher than that of the free enzyme. When the shield was produced with varying ratios of TEOS to APTES, the resulting system transformed 44 to 55 substrates, depending on the shield composition, while slightly enhancing the conversion of some esters (k_{cat} up to ca. 51.52 s⁻¹) compared to free enzyme and EH₃-SPs. The introduction of Ur and Hm did not have a major impact on substrate promiscuity, with 48 and 43 substrates transformed, respectively; their shielding even enhanced the catalytic activity (k_{cat} up to ca. 104.93 s⁻¹). By contrast, the presence of Bz and Bu in the protective shield had a greater impact, with the number of transformed substrates decreasing to 24 and 25 substrates, respectively, and conversion rates also decreasing (k_{cat} ca. 8.33 s⁻¹). Combining the introduction of Ur, Hm, Bz and Bu produced results that were between those produced by Ur and Hm and those by Bz and Bu (33 esters converted; k_{cat} ca. 82.85 s⁻¹). This is in agreement with results obtained by studying P450 promiscuity and efficiency, where the most promiscuous isoforms had higher efficiency values.¹⁴⁹ However, our results are in

contrast with previous reports in which low conversion efficiencies were measured for high values of promiscuity for glutathione-S-transferase enzymes.¹⁵⁰

When comparing to its soluble counterpart, the specific catalytic activity of most shielded EH₃ appeared to be, to some extent, lower (

Figure 18 a and b). However, for several substrates and depending on the shield composition, k_{cat} is markedly increased. For example, the hydrolysis of glyceryl-tripropionate varied with the chemical composition of the shield, from 2.67 s⁻¹ for EH₃-TBu/A_[4/1] to 51.02 s⁻¹ for EH₃-T/A_[6/1]. In the case of phenyl acetate, k_{cat} varied from 8.0 s⁻¹ for EH₃-TBz/A_[4/1] to 104.18 s⁻¹ for EH₃-TUR/A_[4/1]. The observed differences in promiscuity and biocatalytic efficiency might be attributed to either a molecular “sieving” effect of the shield or to a structural change of the active site of the enzyme embedded in the organosilica shield.

We evaluated the similarity of the substrate spectra of all preparations, including EH₃, EH₃-SPs and all nanobiocatalysts synthesized, depending on their chemical similarities, e.g. size and hydrophobicity. By ranking the substrates by their size, no obvious trend was visible. The biggest substrates tested, glucose pentaacetate (338.38 Å³) and glyceryl tributyrate (297.46 Å³), as well as other big substrates such as geranyl acetate (212.09 Å³) and benzyl (*R*)-2-hydroxy-3-phenylpropionate (241.87 Å³), were well converted by all the shielded nanobiocatalysts produced. By contrast, similarly large substrates such as ethyl dodecanoate (258.55 Å³) and benzyl paraben (208.24 Å³) were not hydrolyzed by most of the shielded nanobiocatalysts. In the case of the smallest tested substrates, vinyl acetate (84.89 Å³), it was converted by none of the shielded enzymes, while methyl glycolate (81.98 Å³) was transformed by seven shielded systems. Similarly, vinyl acrylate (96.06 Å³) and butyl acetate (124.13 Å³) are less converted by all tested formulations with regard to the soluble EH₃. These results suggest that there is no direct physical “sieving” phenomenon that can explain the specificity of the shielded

nanobiocatalysts. A similar absence of any explicit trend was observed while focusing on the *Log P* values of the esters. Thus, we could define no clear relationship between the physicochemical properties of the substrates (volume, Å³; *Log P*) and the substrate specificity and the catalytic efficiency of the nanobiocatalysts (

Figure 18 c).

Collectively, these results strongly suggest that the variations in substrate promiscuity are related to a structural change in the active site environment of the enzyme rather than a simple molecular sieve effect of the shield. Indeed, interactions between the shield and residues from the cap domain of EH₃ may lead to a different shape for the tunnels that permits access to the catalytic serine (**Figure 16**).

Enantioselectivity study

To further examine the effect of the shield, we tested a series of nine chiral ester couples (**Figure 19a**). The selectivity towards chiral esters was first determined by measuring the apparent selectivity factor (E_{app}). It is generally accepted that for soluble enzymes, E_{app} can be calculated as the ratio between the k_{cat}/K_m value of the preferred chiral ester to that of the non-preferred chiral ester, when both (*R*) and (*S*)-esters are tested separately. To evaluate possible effects of the immobilization on the enzyme enantioselectivity we herein decided to use the ratio between k_{cat} values (**Table 7 Annex**). Afterwards, the enantiomeric excess (*e.e.*%) values were determined by gas chromatography using racemic mixtures of chiral esters for which substantial increased can be observed, to confirm the results.

Our results show that the soluble enzyme, EH₃, did not display enantioselectivity for any of the esters tested (k_{cat} ratio from 1.0 to 6.1; **Table 7 Annex**) according to the commonly accepted 25-E value threshold above which an esterase is relevant for industrial applications.¹³⁹ The

absence of enantioselectivity can safely be attributed to the large volume of the active site of the enzyme.

Moreover, close inspection of the structure of EH₃ revealed that the acyl/alcohol binding sites are bordered by hydrophobic residues (**Figure 47** Annex). In principle, these residues would establish non-specific interactions with the substrates, which would potentially lack hydrogen bonds often necessary for discriminating between enantiomers.

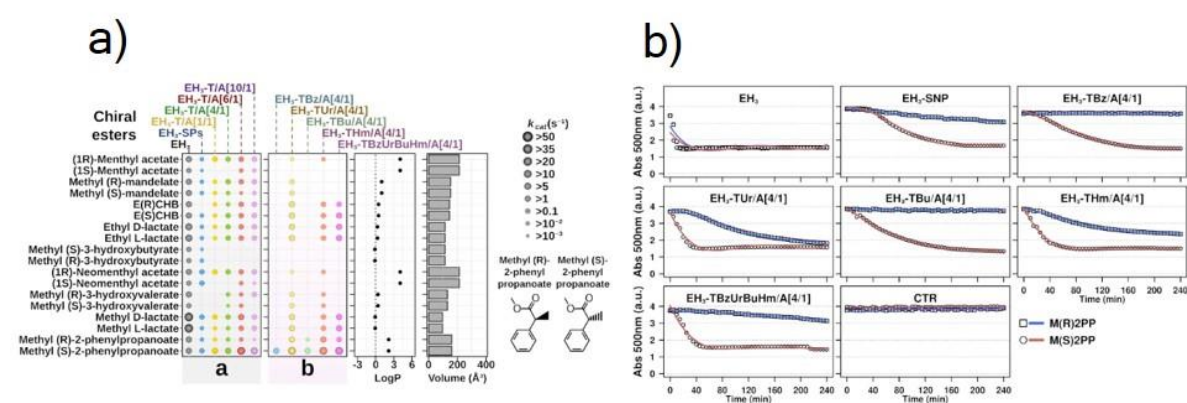


Figure 19. Enantioselectivity study. (a) Diagram of the specific activities of all preparations tested, with nine pairs of chiral substrates shown as a function of their hydrophobicity (log P) and volume (Å³). In the left part of the diagram, the activities for the TEOS/APTES shield compositions are reported. In the right part, the activities for the silane compositions of the shield are reported. The panel was constructed as described in

Figure 18.

As expected, and in agreement with the region previously assumed to be involved, no significant improvement in enantioselectivity was observed after immobilization in the absence of the shield. Only a slight increase in k_{cat} ratio was observed for the immobilized EH₃-SP enzyme for (1R)-menthyl acetate (7-fold), ethyl (S)-4-chloro-3-hydroxybutyrate (43-fold) and methyl (S)-2-phenylpropanoate (8-fold), with no significant improvement in enantioselectivity for the other chiral esters. This moderate increase in enantioselectivity is in agreement with previously reported examples of immobilized esterases.¹⁵¹⁻¹⁵³ By contrast, EH₃-T/A_[1/1], EH₃-T/A_[4/1], EH₃-TU_r/A_[4/1] and EH₃-THm/A_[4/1] selectively hydrolyzed S-enantiomers of menthyl acetate and neomenthyl acetate with an apparent enantiopreference of 100%. Remarkably,

whereas the EH₃-SPs did not show any catalytic activity in the conversion of both enantiomers of methyl-3-hydroxyvalerate, the presence of the shield in EH₃-T/A_[4,6,10/1] and the introduction of Ur and Hm into the shield (EH₃-TUr/A_[4/1] and EH₃-THm/A_[4/1]) reactivated the enzyme in the conversion of both enantiomers. More importantly, EH₃-T/A_[10/1] enabled the EH₃ to selectively hydrolyze the methyl-(*R*)-3-hydroxyvalerate with an apparent enantioselectivity of 100%. In the conversion of methyl mandelate, EH₃-T/A_[6/1] exhibited higher preference and enantioselectivity (k_{cat} ratio of 200.0) for the hydrolysis of the (*S*)-enantiomer than for the (*R*)-enantiomer. Likewise, EH₃-T/A_[10/1] exhibited higher enantioselectivity for the hydrolysis of methyl-(*S*)-2-phenylpropanoate compared to the soluble enzyme (k_{cat} ratio of 1.9) and of EH₃-SPs (k_{cat} ratio of 14.4); EH₃-T/A_[1/1], EH₃-T/A_[4/1], EH₃-T/A_[6/1] and EH₃-TBu/A_[4/1] had k_{cat} ratio values of 54.8, 62.5, 147.1 and 9,311.0, respectively. In addition, EH₃-TBz/A_[4/1] selectively hydrolyzed the *S*-enantiomer and EH₃-TBu/A_[4/1] showed a marked preference for this enantiomer (k_{cat} ratio of 202). By contrast, EH₃-TUr/A_[4/1], EH₃-THm/A_[4/1] and EH₃-TBzUrBuHm/A_[4/1] had k_{cat} ratio values for the conversion of methyl-(*S*)-2-phenylpropanoate of only 5.9, 7.1 and 26.3, respectively.

Encouraged by the promising results obtained from this set of enantioselectivity assays, we carried out additional kinetics with a racemic mixture of methyl-2-phenylpropanoate enantiomers by chiral gas chromatography (**Figure 19b**; **Table 8 Annex**).¹⁴⁴ This chiral esters pair was selected as model as it is structurally similar to ibuprofen-like esters, which are of great industrial relevance, and it was the chiral pair for which higher enantioselectivity increased was observed. The results of kinetics experiments using separate enantiomers and catalytic efficiency calculations (**Table 7 Annex**) confirmed the lack of enantioselectivity of soluble and immobilized EH₃-SPs, as well as increasing enantioselectivity when raising the T/A ratio from EH₃-T/A_[4/1] to EH₃-T/A_[10/1] and also for EH₃-TBz/A_[4/1] and EH₃-TBu/A_[4/1]. For other shielded preparations, enantioselectivity was observed only after short reaction

durations (up to 40 min). These results were confirmed by measuring the enantiomeric excess (*e.e.*%) by gas chromatography, which was 41.7% for soluble EH₃, 70.8% for EH₃-SPs, and as high as 98.40 to 99.99% for EH₃-T/A_[4/1] to EH₃-T/A_[10/1], EH₃-TBz/A_[4/1] and EH₃-TBu/A_[4/1] (**Table 8 Annex**). The gain in enantioselective properties of EH₃ can be explained in terms of a rearrangement of the residues in the proximity of the catalytic site by means of the enzyme-shield interaction. Such a reorientation might position hydrophilic residues pointing towards the acyl/alcohol binding sites, enabling specific interactions that favor one enantiomer. As an example, Glu30 in the highly flexible loop connecting $\alpha 1$ to $\alpha 2$ of the cap domain (highlighted in **Figure 16b**) protrudes from the enzyme in our crystal structures but might be easily reoriented towards the catalytic pocket.

Solvent stability study

Next, we explored the possibility of using the nanobiocatalysts produced herein with a model substrate (α -naphthyl acetate) in solutions containing increasing proportions of an organic solvent, namely acetonitrile (ACN). This solvent was chosen because it is used extensively at an industrial level in ester hydrolase-based processes, which usually cause enzyme instability. We followed the hydrolysis of the ester using high-performance liquid chromatography (HPLC).¹⁴⁴

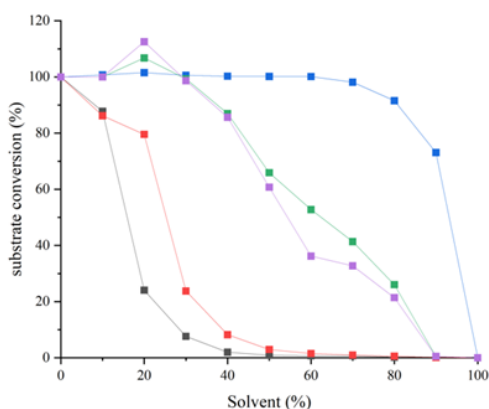


Figure 20. Solvent stability study. Conversion of α -naphthyl acetate in the presence of increasing proportions of acetonitrile, by EH₃ (black), EH₃-T/A_[1/1] (red), EH₃-T/A_[4/1] (blue), EH₃-T/A_[6/1] (green) and EH₃-T/A_[10/1] (purple). Reactions were assayed using HPLC.

Our results show that the specific activity of EH₃ dramatically decreased to 20% of its initial activity in the presence of 20% ACN and to 0% with 40% ACN (**Figure 20**). While the stability of the nanobiocatalyst was only marginally improved for EH₃-T/A_[1/1], there was a marked improvement for EH₃-T/A_[4/1], EH₃-T/A_[6/1] and EH₃-T/A_[10/1], which all displayed high activity even in the presence of large proportions of ACN. In particular, EH₃-T/A_[4/1] maintained a substrate conversion rate as high as 80% in the presence of 90% ACN. Therefore, the high enzymatic stability in the presence of ACN confirmed that the shield establishes a relatively stable environment via modification of the enzymatic active site.

On the reproducibility of the method

In order to prove the reproducibility of both the synthetic method and the biocatalytic transformations, we produced three independent enzyme-based EH₃-Tbu/A_[4/1] particle replicates, and performed statistical analyses of the shield thickness (**Table 1**). This formulation was selected as it was found the highest improvement of enantioselectivity (see above) using this layer composition for shielding the enzyme. Determination of the substrate spectra and the catalytic turnover (k_{cat}) confirmed a high reproducibility of the results. Indeed, the same substrates were found to be converted (**Table 9 Annex**) in comparison with the previous EH₃-Tbu/A_[4/1] produced (**Table 6 Annex**). The standard deviations resulted to be lower than 1% (**Table 9 Annex**), which confirmed the reproducibility and robustness of the immobilization method. We additionally determined the substrate affinity (K_m) for each of the converted substrates using the three independent immobilized preparations, and the values were compared with those of soluble EH₃. As shown in **Table 9 (Annex)**, we found that the layer does not have a major effect on the substrate diffusion/affinity, with K_m differences varying from 1 to 4.5-fold (average: 1.7-fold). Focusing on chiral esters such as methyl-(*S*)-2-phenylpropanoate and methyl-(*R*)-2-phenylpropanoate, we observed no differences in K_m values

before (EH₃) and after (EH₃-TBu/A[4/1]) immobilization, but a marked difference in k_{cat} , responsible for an E_{app} increased by two order of magnitude after immobilization, in agreement with *e.e.*% improvements from $41.70 \pm 0.48\%$ to $99.9 \pm 1.8\%$ (**Table 10 Annex**). This supports our assessment that the variations in substrate promiscuity are related to a structural change in the active site environment of the enzyme, impacting the catalytic efficiency, rather than a sieving effect of the shield.

Table 1. Shield thicknesses (nm) \pm standard error and PDI indices, calculated as in **Figure 17**. Standard error values are calculated from 3 batches of particles prepared separately.

Preparation	Enzyme structure	Enzyme dimensions [nm]	Shield thickness [nm]	PDI	Enzyme concentration [$\mu\text{g mL}^{-1}$]	Immobilization yield [%]
EH ₃ -TBu/A[4/1] nr. 1	Dimer	8.0 x 5.0 x 4.0	3.6 ± 1.5	0.028	164	83
EH ₃ -TBu/A[4/1] nr. 2	Dimer	8.0 x 5.0 x 4.0	4.2 ± 1.3	0.029	165	84
EH ₃ -TBu/A[4/1] nr. 3	Dimer	8.0 x 5.0 x 4.0	4.6 ± 1.5	0.026	165	84
EH _{1A1} - TBu/A[4/1]	Dimer	8.0 x 5.0 x 4.5	6.0 ± 1.8	0.024	6	15
EH ₇ -TBu/A[4/1]	Octamer	9.0 x 8.7 x 8.9	7.2 ± 1.3	0.022	95	94

On the versatility of the method

In order to evaluate the versatility of the method herein described, we decided to apply it to two additional enzymes characterized in previous studies, namely EH_{1A1} and EH₇.^{14,22} EH_{1A1} is a mutant (R23G) of a serine ester hydrolase isolated from the metagenomic DNA of microbial communities inhabiting the Lake Arreo, an evaporite karst lake in Spain.¹⁴ EH₇ (Gene Bank acc. nr. KY483644) was isolated from the metagenomic DNA of microbial communities inhabiting the chronically polluted seashore area of Milazzo harbor in Sicily (Italy), as EH₃.²² In a recent study, EH_{1A1} was identified, among 145 ester hydrolases, as the enzyme with the broadest substrate spectrum when tested with a set of ca. 100 chemically and structurally different esters.¹⁴ EH₇ was identified as the seventh most substrate-promiscuous

one.²². EH_{1A1} and EH₇ were selected for the following reasons. First, their crystal structures were fully characterized (EH_{1A1}: 6RB0 in **Figure 50** Annex;¹⁴ EH₇, available but not yet released to PDB). Second, they present catalytic features similar to those of EH₃: they are highly active, and they are substrate-promiscuous but not enantioselective. Third, they have different sizes and oligomeric state: EH₃ is a dimer of 8.0 x 5.0 x 4.0 nm; EH_{1A1} is a dimer of 8.0 x 5.0 x 4.5 nm; EH₇ is an octamer of 9.0 x 8.7 x 8.9 nm (**Table 1**). Fourth, although they have a catalytic α/β hydrolase fold, they are structurally different and belong to different sub-families of ester-hydrolases; thus, while EH_{1A1} and EH₃ belongs to Family IV, EH₇ belongs to Family VII.

EH_{1A1} and EH₇ were immobilized on the surface of SPs following the method previously described for EH₃. The immobilization of EH_{1A1} and EH₇ resulted in immobilizations yield of 15 and 94 % respectively, allowing the immobilization of 6 and 95 $\mu\text{g mL}^{-1}$ (**Table 1**). The immobilized enzymes were further shielded using TBu/A as this formulation yielded the best results in terms of enantioselectivity for EH₃. EH_{1A1}-TBu/A_[4/1] and EH₇-TBu/A_[4/1] produced were characterized by means of SEM (**Figure 51** Annex and **Table 1**). The thickness of the organosilica layer was 6.0 ± 1.8 nm and 7.2 ± 1.3 nm for EH_{1A1}-TBu/A_[4/1] and EH₇-TBu/A_[4/1] respectively.

The analysis of the substrate spectrum, catalytic turnover (k_{cat}) and substrate affinity (K_m) of both soluble enzymes and the shielded systems was carried out (**Figure 52** and **Figure 53**; **Table 9** a, b Annex). From our results, we observed that soluble EH_{1A1} and EH₇ hydrolyzed 74 and 71 esters, respectively (**Table 10** a,b Annex), with phenyl propionate (k_{cat} ca. 46.7 s^{-1}) and glyceryl tripropionate (k_{cat} : ca. 28.3 s^{-1}) serving as the best substrates, respectively. EH_{1A1}-TBu/A_[4/1] and EH₇-TBu/A_[4/1] were capable of hydrolyzing 46 and 44 esters, respectively. Interestingly, when comparing EH₃-TBu/A_[4/1] to EH_{1A1}-TBu/A_[4/1] and EH₇-TBu/A_[4/1] the number of substrates converted by EH_{1A1} and EH₇ after shield were higher (46 and 44 esters

converted, respectively) compared to the EH₃ counterpart, which converted only 25 substrates after shielding. Therefore, the selectivity of EH_{1A1} and EH₇ after shielding with TBu/A results more similar to the selectivity of EH₃ shielded with TUr/A, THm/A and T/A_[1/1].

The decrease in the substrate spectra of EH_{1A1}-TBu/A_[4/1] compared to EH_{1A1} can be also due to the interactions between the shield and the three superficial Lys (Lys34, Lys 38 and Lys 212) that are all found in the flexible cap domain (**Figure 50 Annex**); as in EH₃. This may lead to a different shape for the channels that permits access to the catalytic serine. In case of EH₇, four superficial Lys residues are found: Lys161, Lys217, Lys236 and Lys 265 (unpublished results). Two of these (Lys161 and Lys 265) are located at the entrance of a wide cavity giving access to the catalytic site, thus their interaction with the shield may also affect the different substrate specificity of EH₇-TBu/A_[4/1] in comparison to EH₇. As for EH₃, we observed hyperactivation for the hydrolysis of some esters. As example, vinyl propionate and propyl butyrate were 309 and 20 times better hydrolyzed by EH_{1A1}-TBu/A_[4/1], compared to EH_{1A1}. Also, methyl ferulate was 562 times better hydrolyzed by EH₇-TBu/A_[4/1], compared to EH₇. In other cases, a negative effect in the catalytic rate was observed, which was not directly a consequence of the layer as K_m were not significantly affected in most cases.

We further examined the effect in enantioselectivity by determining the E_{app} (**Figure 21, Table 9 b, Table 11 Annex**). EH_{1A1} was capable of hydrolyzing 8 pairs of enantiomers (E_{app} ranging from 1.0 to 6.7); by contrast EH_{1A1}-TBu/A_[4/1] was capable of hydrolyzing 5 pairs with E_{app} ranging from ca. 60 to 16000. Similarly, EH₇ was capable of hydrolyzing 6 pairs of enantiomers (E_{app} ranging from 1.1 to 14); while EH₇-TBu/A_[4/1] was capable of hydrolyzing 6 pairs with E_{app} ranging from ca. 9 to 5300. Those results are in agreement with the change of selectivity of the chiral esters, demonstrated with the EH₃.

We carried out additional kinetic analyses with separate ethyl (*R*)-4-chloro-3-hydroxybutyrate and ethyl (*S*)-4-chloro-3-hydroxybutyrate and confirmed the absence of enantioselectivity of

the soluble EH_{1A1} and EH₇ (**Table 10** Annex). Remarkably, a dramatic improvement of enantioselectivity was found for the two shielded counterparts (**Figure 21**). The EH_{1A1}-TBu/A_[4/1] and EH₇-TBu/A_[4/1] preferentially converted the ethyl (*S*)-4-chloro-3-hydroxybutyrate.

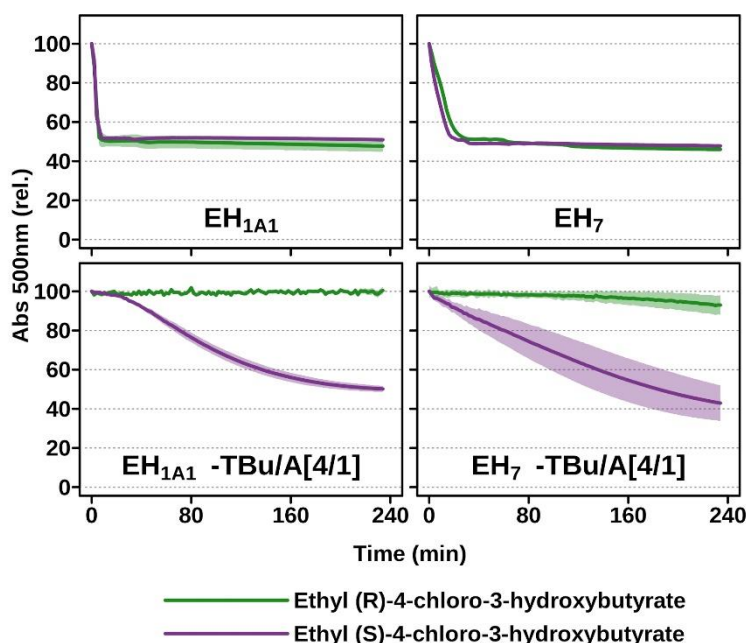


Figure 21. Enantioselectivity study. Kinetic conversion of ethyl (*R*)-4-chloro-3-hydroxybutyrate (E(*R*)CHB) and ethyl (*S*)-4-chloro-3-hydroxybutyrate (E(*S*)CHB) by EH_{1A1}, EH_{1A1}-TBu/A_[4/1], EH₇ and EH₇-TBu/A_[4/1], and a control reaction without enzymatic preparation added. The kinetics of the hydrolysis of separate enantiomers are shown, followed by recordings of the absorbance at 550 nm. At each data point, enantiomeric excess (*e.e.*%) was determined by HPLC using a racemic mixture of ethyl 4-chloro-3-hydroxybutyrate, as described previously.

These results were confirmed by measuring the enantiomeric excess (*e.e.*%) with a racemic mixture of ethyl-4-chloro-3-hydroxybutyrate enantiomers by HPLC.¹⁴⁴ While *e.e.*% measured for the soluble enzymes was *ca.* 50%, the *e.e.*% of EH_{1A1}-TBu/A_[4/1] was 99.7% for and the one of EH_{1A1}-TBu/A_[4/1] was 98.5% (**Table 11** Annex). Note, that methyl-2-propanoate could not be used to determine the enantioselectivity for EH_{1A1} and EH₇ as for EH₃, as this substrate were not used by neither the immobilized preparations nor the EH₇ soluble sub-enzymes (**Figure 21**, **Table 9 b** Annex).

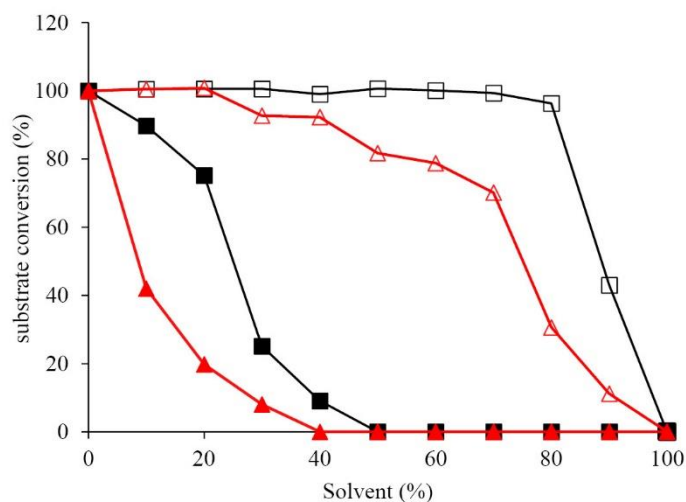


Figure 22. Solvent stability study. Conversion of α -naphthyl acetate in the presence of increasing proportions of acetonitrile, by EH_{1A1} (black full squares), EH_{1A1}-TBu/A_[1/1] (black empty squares), EH₇ (red full triangles), EH₇-TBu/A_[4/1] (red empty triangles).

Finally, we studied the stability in the presence of acetonitrile of the EH_{1A1}, EH_{1A1}-TBu/A_[4/1], EH₇ and EH₇-TBu/A_[4/1], as for EH₃ preparations (

Figure 22). Similarly to what was observed with EH₃, the two soluble EH_{1A1} and EH₇ retained limited activity (25 and 8%) by increasing the ACN concentration up to 30%. On the contrary, EH_{1A1}-TBu/A_[4/1] maintained a substrate conversion rate of 96% in the presence of 80% ACN, while EH₇-TBu/A_[4/1] maintained a substrate conversion rate of 70% in the presence of 70% ACN. This set of results further confirm the stabilization effect of the shield.

5 CONCLUSIONS

We have developed a strategy that allows transforming the properties of enantioselectivity and solvent stability of an enzyme. This strategy relies on enzyme supramolecular engineering, which, in contrast to enzyme engineering, refers to a novel concept of enzyme supramolecular modification without manipulating the protein sequence by genetic engineering or covalent modification of the biomolecule. We applied this enzyme supramolecular engineering approach, to three ester hydrolase enzymes that displays broad substrate-promiscuity and non-enantioselectivity. The structural study of the enzymes studied has been solved by means of single crystal X-ray crystallography, which confirmed a voluminous active site explaining the lack of substrate (enantio)selectivity. The enzyme properties have been modified via the meticulous modification of its environment using a variety of organosilane building blocks in order to produce a layer intimately surrounding the enzyme. The synthetic shield produced is believed to structurally impact the active site of the enzyme promoting the rearrangement of the residues in its proximity causing an increase in stereoselectivity without significantly restricting docking freedom for non-chiral substrates. Evidence of this structural change is provided by the study of the biocatalytic properties of the nanobiocatalysts produced using a broad range of carboxylic ester substrates. We demonstrated that the enzyme shielding method described herein allows transforming non-enantioselective ester hydrolases into enantioselective ones and drastically improving their stability in the presence of an organic solvent. We do believe that, in view of the inexpensive starting chemicals and mild conditions used during the relatively simple synthetic process, and with additional substantial efforts for upscaling, this method could be applied to a wide range of promiscuous enzymes enabling their use in industrially relevant processes.

ASSOCIATED CONTENT

Supporting Information.

The Supporting Information is available free of charge at: <https://pubs.acs.org/acscatalysis.xxx>.

Full description of the experimental and characterization methods; supporting figures and tables. Additional EH₃ and EH₃-B-4NHP crystal structures details are available in Data S1 and S2.

AUTHOR INFORMATION

Corresponding Author

Patrick Shahgaldian – University of Applied Sciences and Arts Northwestern Switzerland, School of Life Sciences, Institute of Chemistry and Bioanalytics, Muttenz, Switzerland; Email: patrick.shahgaldian@fhnw.ch.

Manuel Ferrer – Institute of Catalysis, Consejo Superior de Investigaciones Científicas (CSIC), ES-28049 Madrid, Spain. E-mail: mferrer@icp.csic.es

Julia Sanz-Aparicio – Institute of Physical-Chemistry Rocasolano, Consejo Superior de Investigaciones Científicas (CSIC), ES-28006 Madrid, Spain. E-mail: xjulia@iqfr.csic.es

Other Author

Carolina I. Giunta – University of Applied Sciences and Arts Northwestern Switzerland, School of Life Sciences, Institute of Chemistry and Bioanalytics, Hofackerstrasse 30, CH-4132 Muttenz, Switzerland.

Isabel Cea-Rama – Institute of Physical-Chemistry Rocasolano, Consejo Superior de Investigaciones Científicas (CSIC), ES-28006 Madrid, Spain.

Sandra Alonso – Institute of Catalysis, Consejo Superior de Investigaciones Científicas (CSIC), ES-28049 Madrid, Spain.

Manon L. Briand – University of Applied Sciences and Arts Northwestern Switzerland, School of Life Sciences, Institute of Chemistry and Bioanalytics, Hofackerstrasse 30, CH-4132 Muttenz, Switzerland.

Rafael Bargiela – School of Natural Sciences and Centre for Environmental Biotechnology, Bangor University, Deiniol Rd, Bangor, LL57 2UW, UK.

Cristina Coscolín – Institute of Catalysis, Consejo Superior de Investigaciones Científicas (CSIC), ES-28049 Madrid, Spain. E-mail: cristina.coscolin@csic.es

Philippe F.-X. Corvini – Institute of Ecopreneurship, School of Life Sciences, University of Applied Sciences and Arts Northwestern Switzerland, Hofackerstrasse 30, CH-4132 Muttenz, Switzerland.

Author Contributions

C. I. G. and I. C. R. contributed equally to this work. The manuscript was written through contributions of both authors, who have given approval to the final version of the manuscript.

Funding Sources

This work was funded by the European Union's Horizon 2020 program (INMARE project, grant agreement no. 634486), grants PCIN-2017-078 (within the Marine Biotechnology ERA-NET), BIO2016-76601-C3-3-R and BIO2017-85522-R from the Ministerio de Economía y Competitividad, Ministerio de Ciencia, Innovación y Universidades (MCIU), Agencia Estatal de Investigación (AEI), Fondo Europeo de Desarrollo Regional (FEDER) and European Union (EU). R.B. acknowledges the support of the UK Biotechnology and Biological Sciences

Research Council (BBSRC; grant No. BB/M029085/1) and the Centre of Environmental Biotechnology Project and the Supercomputing Wales project, which are partly funded by the European Regional Development Fund (ERDF) via the Welsh Government.

ACKNOWLEDGMENT

J. L. Gonzalez-Alfonso, D. Rojo and C. Barbas are acknowledged for HPLC and GC analyses. We thank the staff of the Synchrotron Radiation Source at Alba (Barcelona, Spain) for assistance at BL13-XALOC beamline. The authors would like to acknowledge M. Chami and the Bio-EM lab of the Biozentrum, University of Basel for assisting and advising in cryo-EM characterization.

CHAPTER 4

AUROZYME:

towards the engineering of artificial cold active

nanobiocatalysts

SUMMARY

In the present chapter, we report a novel method to design AuNPs co-immobilized with enzymes at the surface of silica particles (SPs) and shielded with a thin organosilica layer. The production of an artificial biocatalyst, the Aurozyme, able to function at low temperatures, is herein proposed. Our approach is based on the use of AuNPs placed in close proximity to natural enzymes. AuNPs due to their plasmonic properties, enable establishing locally heated areas in the enzyme environment, thus endowing the enzyme with high activity yet being in a cold bulk system. Beside the development of a simple method for the efficient immobilization of AuNPs on silica, we demonstrated that the developed systems allow combining the advantages of the photothermal properties and the enhanced stability of immobilized AuNPs with an improved activity of the shielded enzyme.

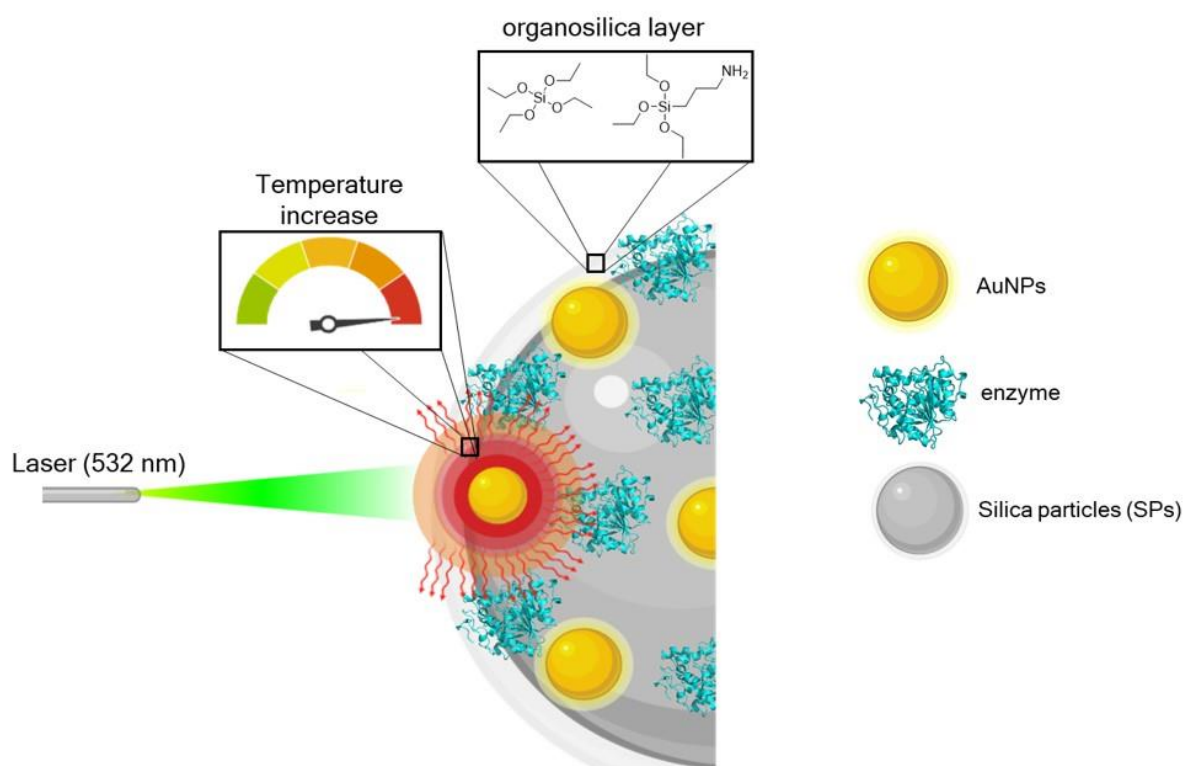


Figure 23. Schematic depiction of photothermal activation of enzymes in the Aurozyme. The Image was created with BioRender. The enzyme crystalline structure reported is that of the Lipase B from *Candida Antarctica* (CalB).

The results and discussion on the Aurozyme in the section 3 is introduced by an insight into cold active enzymes and by an overview of AuNPs properties and applications in section 1 and 2, respectively.

1 COLD ACTIVE ENZYMES (CAEs)

Cold active enzymes (CAEs) from psychrophilic organisms (i.e extremophilic organisms able to survive and proliferate in temperatures ranging from -20°C to $+10^{\circ}\text{C}$), are a class of enzymes active at low temperature, with optimal activity temperature between 20 and 30°C .¹⁵⁴ The reason of their higher enzymatic activity at low temperatures lies in the increased conformational flexibility at these temperatures in comparison with their mesophilic or thermophilic counterparts. The high conformational mobility of CAEs at low temperatures, leads to the need of a limited amount of activation energy in their catalytic processes.¹⁵⁵

Cold active lipases and proteases could find application in the detergent industry to improve cold washing, thus reducing energy consumption and preserving the life and quality of fabrics.¹⁵⁶ CAEs might be used in the food industry because the low working temperatures allow reducing bacterial contamination.¹⁵⁴ Specifically, cold active β galactosidases may be implemented in the dairy industry to hydrolyze lactose for lactose-free products, cold active proteases may replace mesophilic proteases currently used for the hydrolysis of milk proteins that lead to milk coagulation in cheese manufacturing processes, and pectinases may replace their mesophilic counterparts in food processing (e.g. increasing the viscosity of ice cream, juices, and sauces).¹⁵⁴ Along with the potential applications reported above other usages of CAEs, as example in bioremediation processes or for the production of cosmetic or pharmaceuticals, are currently being explored.¹⁵⁴

The scientific research on this class of enzymes concerns the screening of cold regions from which such enzymes could be isolated. Artic or Antarctic regions, glaciers or sea sediments are

often considered for the search of psychrophilic enzymes.¹⁵⁶⁻¹⁵⁷ Beside the search of natural CAEs, strategies aimed at the screening of characteristic structural motif on the surface of CAEs to be introduced on mesophilic enzymes by protein engineering strategies were considered.¹⁵⁸⁻¹⁵⁹ However, the activity of CAEs resulted to be lower than the activity of their mesophilic counterparts at the optimum temperature.¹⁶⁰ Moreover, it was reported that the active site of CAEs is more heat-labile, due to the increased flexibility of the residues in its vicinity, than other structural parts of the enzymes, inducing to the loss of enzymatic activity before protein unfolding.¹⁶¹ Therefore, the usage of CAEs may be limited by their low stability, being tremendously sensitive to temperature increases.¹⁶²

2 GOLD NANO-STRUCTURES

Firstly observed by Michael Faraday in 1857,¹⁶³ gold nanoparticles have received increasing interest from the scientific community mainly due to the simplicity and tunability of their synthesis and due to plasmonic properties.¹⁶⁴⁻¹⁶⁵

AuNPs are commonly synthesized via chemical reduction of gold salts in two steps. Firstly, the Au^{3+} are reduced to Au^0 using a reducing agent (e.g. borohydride, citrate). Secondly, the growth of the Au^0 clusters into nanoparticles of various size is obtained by means of stabilizing agent such as citrate, cetyltrimethylammonium bromide (CTAB) or polymers, which prevent the particles aggregation.¹⁶⁶ The stabilizer molecule and the reducing agent can be the same molecule, like in the most used synthetic protocol described by Turkevich.¹⁶⁷ Several synthetic protocols based on the Turkevich method have been developed for tuning size, shape, and surface chemistry of gold nano-structures.^{166, 168}

Gold nanoparticles are plasmonic nanoparticles. Surface plasmons are defined as waves produced by the interaction of free electrons of conductor materials with the electro-magnetic field of light. The proper match between the size and shape of the material and the wavelength

of the incident light leads to the generation of surface plasmon resonance (SPR) (Figure 24).¹⁶⁹ As a result of this interaction in resonance, the light at the SPR wavelength is absorbed and scattered by the AuNPs.

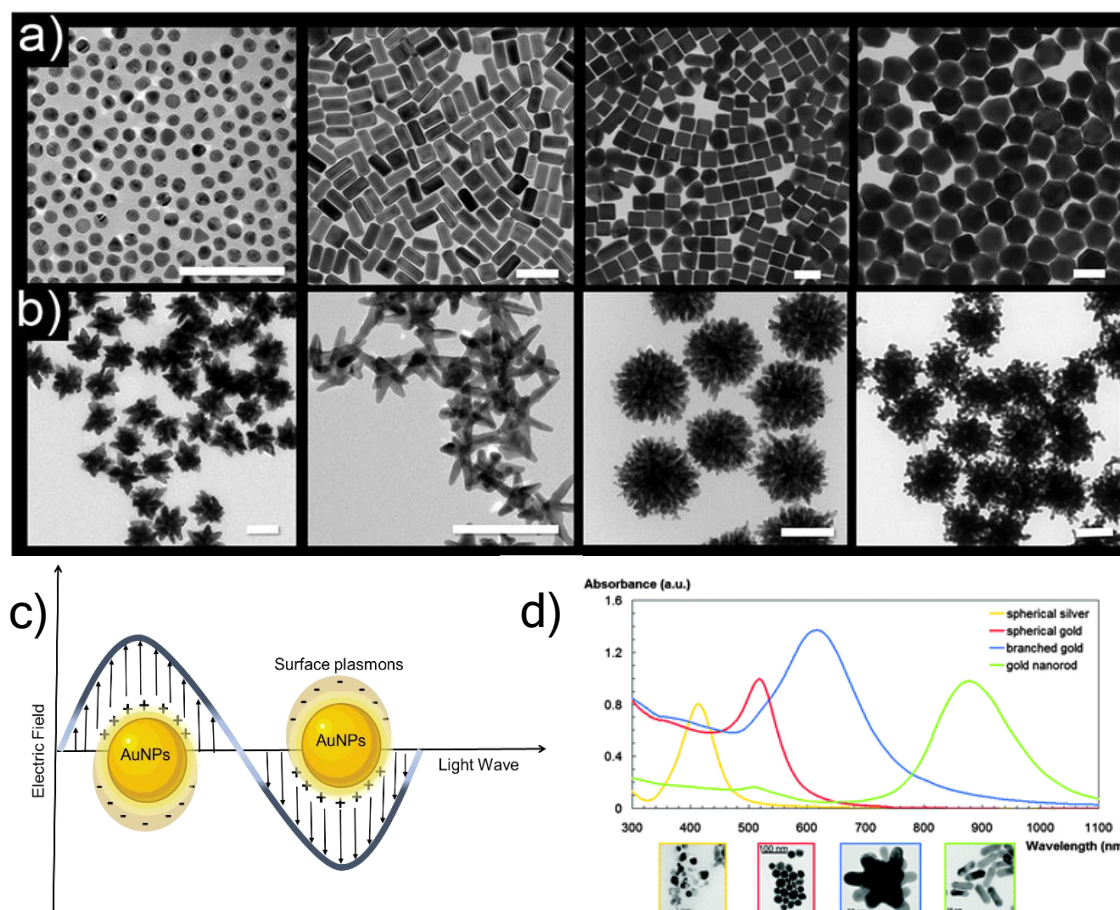


Figure 24. AuNPs properties. (a) TEM micrographs illustrating a library of different gold NPs with regular geometrical shapes and (b) branched shapes. Scale bars represent 100 nm. Figures adapted with permission from reference ¹⁷⁰. Creative Common CC BY licence. (c) Schematic depiction of localized surface plasmon resonance (LSPR) typical on AuNPs. (d) LSPR absorbance of spherical silver and gold, branched gold and gold nanorods. Adapted with permission from reference ¹⁷¹, Copyright (2012) Royal Society of Chemistry.

In Figure 24, SPR absorbance peaks of different gold nanoparticles' structures, ranging from the simpler spherical or rod-like shapes to the more hierarchical branched shapes, are reported.¹⁷¹ The SPR peak is centred at different wavelength showing different profile according to the different geometry and size of gold nanoparticles. For example, while the SPR peak of the gold nanospheres ranges between 518 and 580 nm (by increasing their size),¹⁷² the

spectrum of the gold nanorods is characterized by two peaks; the first one between 518 and 580 nm and the second one between 600 and 1100 nm.¹⁷³ Therefore, the position of the SPR peak can be used as a tool to study the structure and the size of gold nanostructures. Moreover, an analysis of the shift of the SPR peak can be related to modifications of the chemical environment of AuNPs, which can induce changes of the free electron density of the particles.¹⁷⁴

One resulting phenomena of the plasmonic properties of the AuNPs is the conversion of light into heat upon light irradiation. The conversion is efficient only if the wavelength of the light has the same value of the SPR wavelength.¹⁷⁵ Richardson *et al.* investigated the heat generation mechanism of AuNPs embedded into an ice film upon laser irradiation at the wavelength of the SPR of the AuNPs.¹⁷⁶ By increasing the laser power, the melting process of the ice was studied using time-resolved Raman. The irradiation of aggregates of AuNPs with different size resulted on different power threshold values at which the process of ice melting occurred. Interestingly, the irradiation of large aggregates of 50 nm led to the explosive melting of ice using 10 mW laser power. The laser power threshold, for the initiation of the ice melting process by such large particles, was found equal to 4 mW.¹⁷⁶

On account of previously mentioned AuNPs physical-chemical properties and of their compatibility as support for bioconjugation of biomolecules or drugs, AuNPs were investigated for sensing and imaging applications, photothermal therapy, and drug delivery.¹⁷⁷ It was shown that the immobilization of enzymes on AuNPs represents a valid strategy for the improvement of the catalytic properties of enzymes.¹⁷⁸⁻¹⁸⁰ Breger *et al.* demonstrated that the nanoparticle size influences the activity of an immobilized phosphotriesterase with an increase in the k_{cat} value of ca. 3–10-fold by reducing the size of AuNPs from 100 to 1.5 nm.¹⁸¹ The authors

reported that the reduction of the diameter of AuNPs and the increase of their curvature affected the rate of the enzyme-substrate release.

However, the main obstacle for the usage of gold nanoparticles is their poor stability, which stems from their tendency to aggregate upon changes in pH or temperature, or also prolonged irradiation time. Working on the photothermal conversion of CO₂ to hydrocarbons, Yu *et al.* demonstrated that AuNPs are capable, upon visible light irradiation, of catalyzing the reduction of CO₂ to yield methane and ethane.¹⁸² The AuNPs used, however, showed a propensity to aggregation and a loss in catalytic efficiency after 10 hours of reaction. Consequently, tuning the thermal response of AuNPs, might be difficult. Thus, it is of great importance to develop methods allowing to enhance the photostability of colloidal AuNPs without hampering their SPR properties.

The photothermal properties of AuNPs have also been exploited for immobilized enzymes. For example, Tadepalli *et al.* carried out the immobilization of horseradish peroxidase onto the surface of AuNPs or nanorods (AuNRs) followed by the encapsulation of the enzyme within either an organosilica material or a metal-organic framework (MOF).¹⁸³⁻¹⁸⁴ The authors showed an increase of enzyme activity at 25°C of nearly 20% on spherical AuNPs and of 110% on

AuNRs after laser exposure compared to the enzyme activity without laser irradiation (

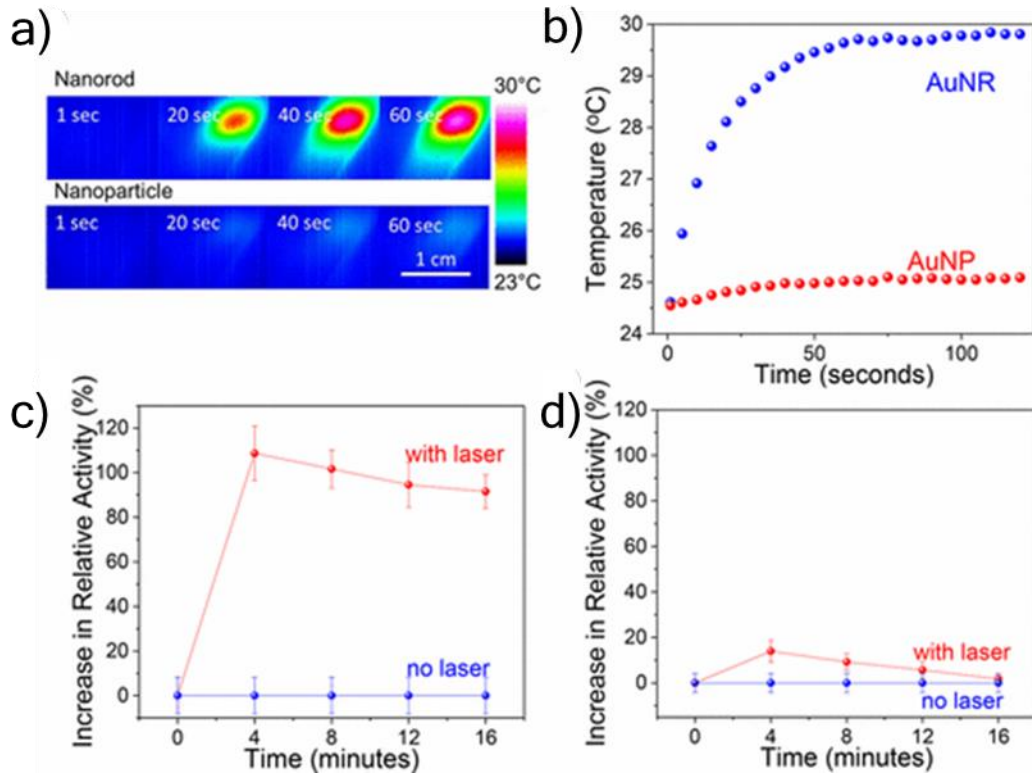


Figure 25).

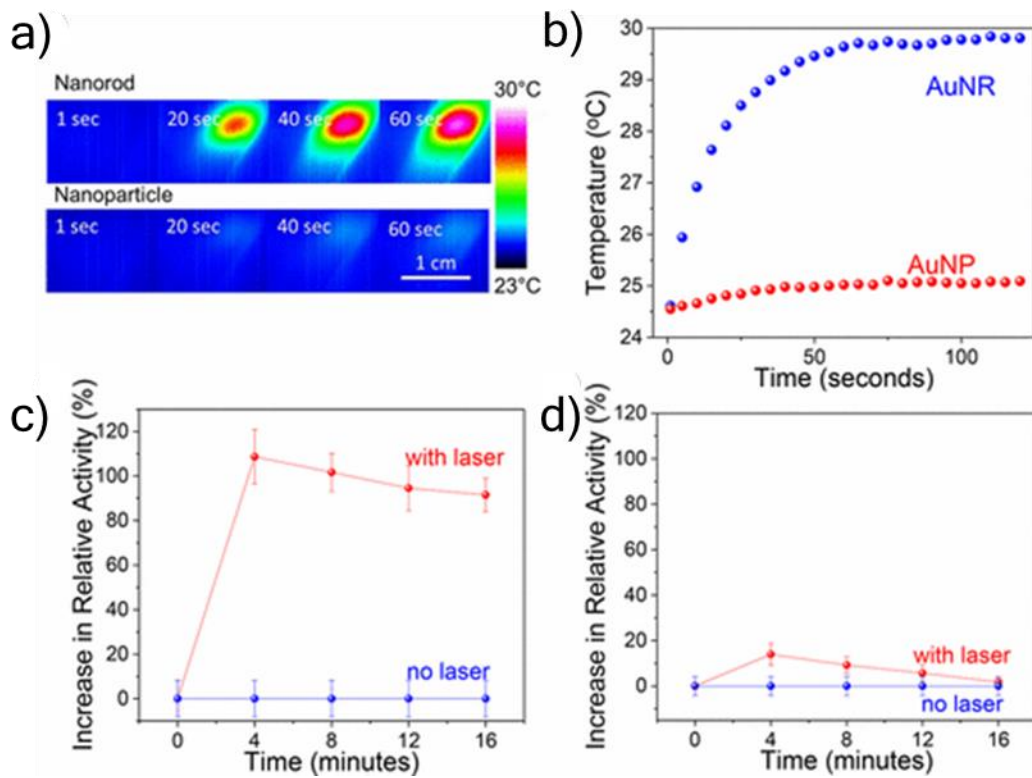


Figure 25. Photothermal enhancement of enzyme activity. (a-b) Temperature increase upon irradiation of AuNPs and AuNRs measured with an IR camera; (c) increase in relative activity for the enzyme immobilized on AuNRs and on (d) AuNPs. Reprinted (adapted) with permission from reference 183. Copyright (2017) American Chemical Society.

In order to increase their stability, the immobilization of AuNPs on a solid support represents a valid strategy to suppress particles aggregation.¹⁸⁵⁻¹⁸⁷ A range of carrier materials have been used for AuNPs immobilization including TiO₂,¹⁸⁸ SiO₂,¹⁸⁹ CeO₂,¹⁹⁰ and zeolites,¹⁹¹ for their application in catalysis¹⁶⁹ and nano-electronics,¹⁹²⁻¹⁹³ among other fields.

3 RESULTS AND DISCUSSION

Aurozyme design

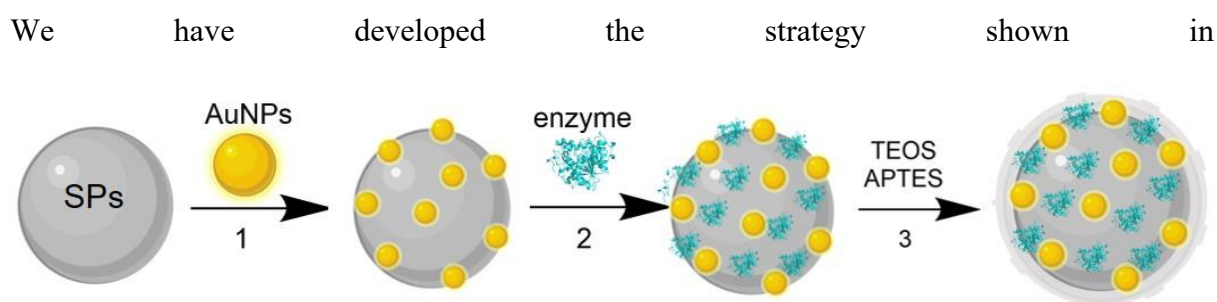


Figure 26, to design a nanobiocatalyst that can be photothermally activated. Enzymes and AuNPs are co-immobilized onto a silica support and embedded in an organosilica layer of controlled thickness that, besides providing a chemical stabilization of the enzyme structure, is expected to allow the confinement of the photothermal energy emitted by AuNPs upon light excitation. On account of its high transparency to the incident light at the SPR of AuNPs along with its thermal properties as insulator, organosilica was the material of choice.¹⁹⁴

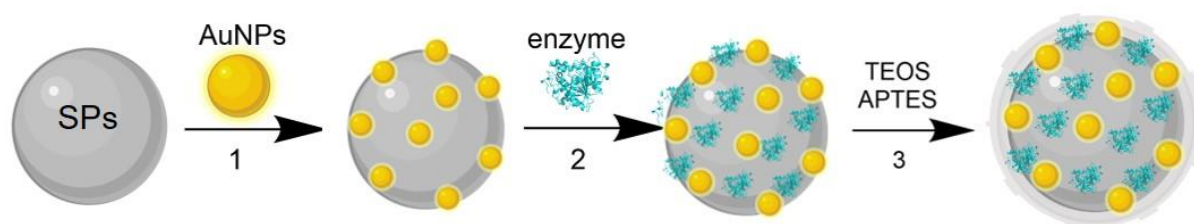
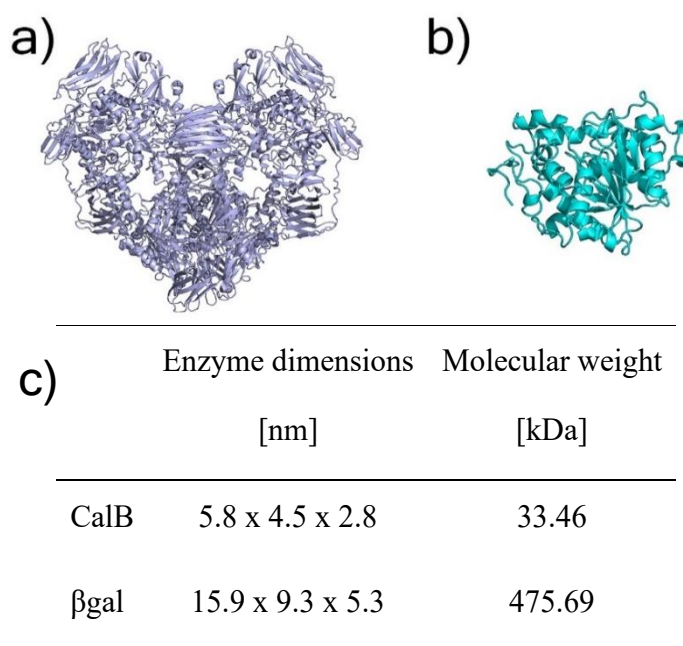


Figure 26. Synthesis of the nanobiocatalyst. Schematic representation of AuNPs (1) and enzyme (2) immobilization and protection (3) in an organosilica layer of controlled thickness.

As model enzymes, we decided to use β -galactosidase (β -gal) and Lipase B from *Candida Antarctica* (CalB). While β -gal from *K. lactis* is a large tetrameric enzyme,¹⁹⁵ the CalB is a small monomeric enzyme (

Figure 27).¹⁹⁶ Their different structural properties are expected to differently affect the enzyme photothermal activation, in regard to the enzyme stability and thermal response at low



temperature.

Figure 27. Structural details of β -gal and CalB. Crystal structures of (a) β -gal from *K. lactis* and of (b) CalB. (c) Summary of structural details of the two enzymes (PDB 3OBA for β -gal and 1TCA for CalB).

β -gal and CalB are enzymes of interest for a variety of applications also in industrial sectors including food, cosmetic, and pharmaceutical industries.¹⁹⁷ As example, β -galactosidase is widely used for lactose hydrolysis in the production of lactose free products.¹⁹⁸ For this specific application, the main issue with the use of mesophilic enzymes comes from the process temperatures, ranging from 20 to 50°C depending on the specific β -galactosidase used (e.g. *K. lactis*, *Aspergillus oryzae*, *Aspergillus niger*). At these temperatures, the risk of microbial

contaminations represents an issue.¹⁹⁸ Moreover, there is a clear interest in developing cryophilic lipases as it is expected to unlock their application where low temperature/energy is of interest (e.g. for the production of detergents with high washing efficiency at low temperature).¹⁵⁶⁻¹⁵⁷

AuNPs synthesis and characterization

Taking into consideration that the AuNPs will be entrapped within an organosilica shield, we initially explored the possibility to avoid covalent cross-linking of the AuNPs on the surface of SPs by immobilizing the AuNPs via electrostatic interactions.

To that end, spherical AuNPs with trisodium citrate (8) as capping agent were synthesized following the Turkevich method (**Figure 28**).¹⁶⁷

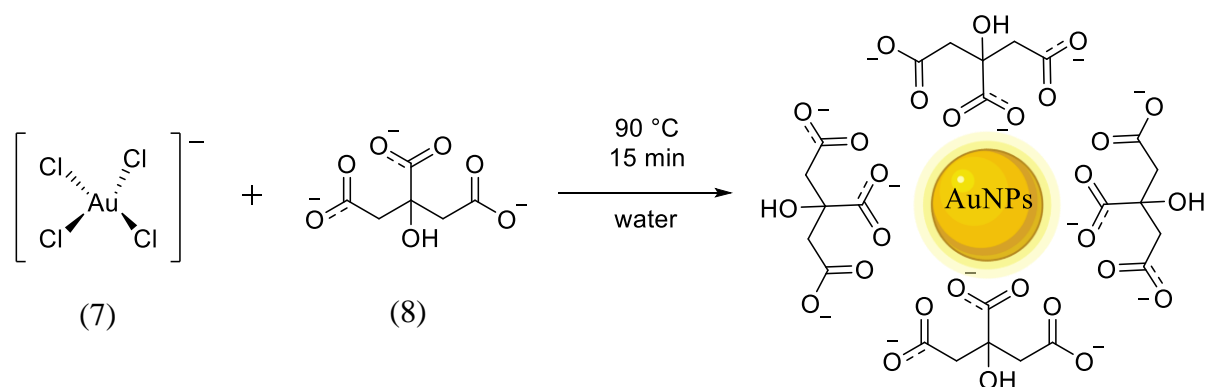


Figure 28. Synthesis of AuNPs with citrate as reducing agent and capping material. Au^{3+} are firstly reduced to Au^0 at 90°C and then stabilized by the citrate (8), in water.

Those nanoparticles were fully characterized by transmission electron microscopy (TEM), scanning electron microscopy (SEM), atomic force microscopy (AFM), and UV-vis spectroscopy (

Figure 29). The TEM characterization of AuNPs showed that the synthesized AuNPs had a spherical shape as expected. Moreover, particles characterization highlighted their high monodispersity, which was confirmed by a statistical analysis. A statistical analysis of the

AuNPs diameter was performed measuring 633 nanoparticles on TEM micrographs; the diameter of the AuNPs resulted to be 18 nm with a standard deviation (SD) of 1 nm.

The polydispersity index (PDI) calculated as

$$\frac{\sigma}{(\bar{d})} \quad 1$$

where (σ) is the standard deviation and \bar{d} the average diameter of the AuNPs, resulted to be 0.06 indicating a high monodispersity of the AuNPs and confirming the results of the TEM characterization. In contrast, the SEM characterization of the AuNPs revealed a certain degree of aggregation of the AuNPs. However, we believe that this result was due to the sample preparation procedure used for the SEM analysis, which consists in the spreading of a drop of the AuNPs solution onto silicon wafer substrates previously cleaned with ethanol.

A UV-vis study was carried out to characterize the photothermal properties of the citrate capped AuNPs. Specifically, the spectrum of the AuNPs at wavelengths ranging from 400 to 900 nm was measured to determine the wavelength of the SPR peak. Moreover, the UV-vis spectrum was used to detect the potential formation of aggregated particles or the presence of different gold nanostructures (e.g. AuNRs) in the solution. The UV-vis characterization revealed that the SPR peak of the AuNPs was placed at 520 nm, as expected for particles diameter of ca. 20 nm.¹⁶⁹ Moreover, the spectrum did not display additional peaks typically appearing between 600 and 900 nm when aggregates or AuNRs, and other gold nanostructures are present in the solution.¹⁶⁹

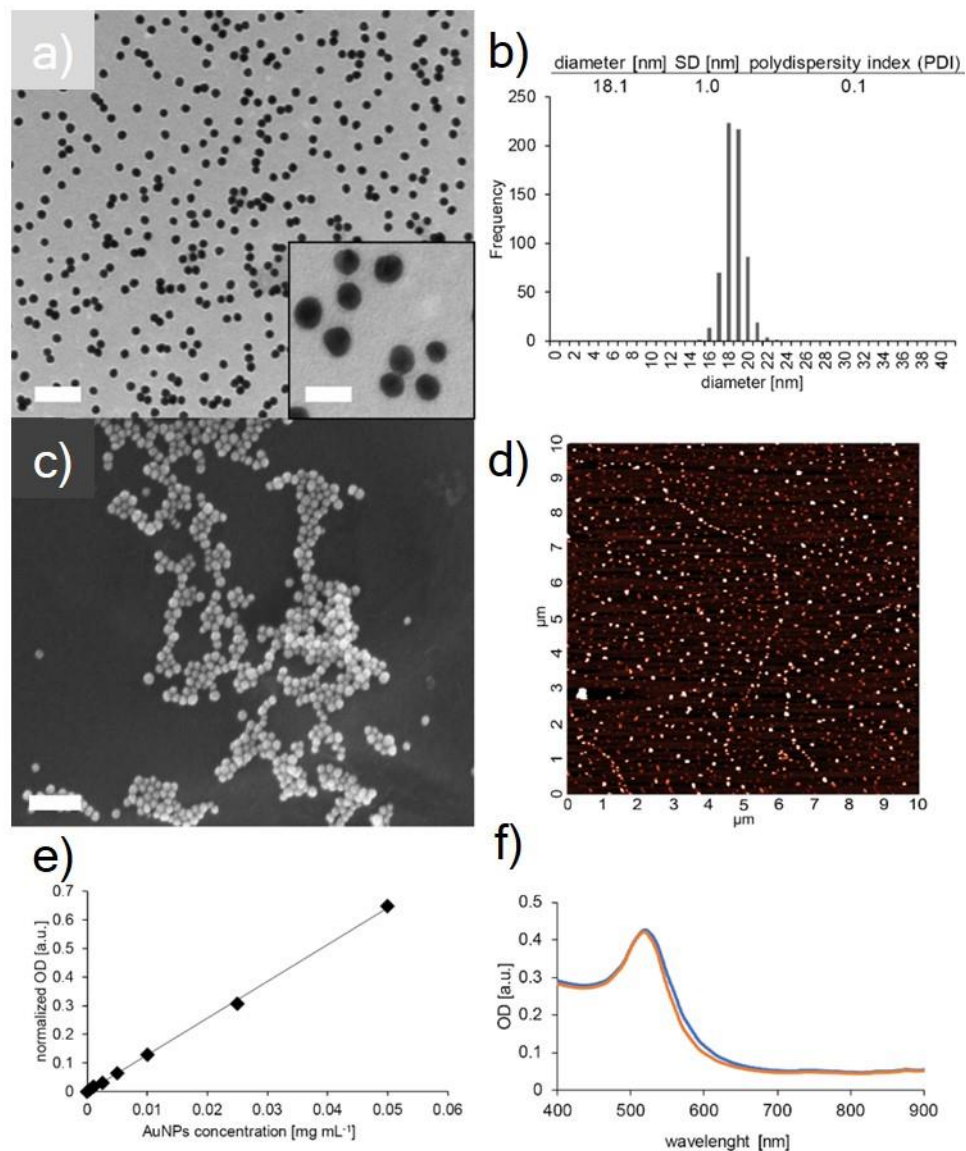


Figure 29. AuNPs characterization. (a) TEM micrographs; (b) statistical analysis based on TEM micrographs (a); (c) SEM micrographs and (d) AFM image of AuNPs-citrate. (e) Calibration line of absorbance at 520 nm vs. concentrations of a solution of commercial AuNPs citrate; (f) absorption spectra of AuNPs-citrate solution before (red line) and after freeze-drying, in presence of sucrose 5% w/v, diluted 10 x (blue line).

The absorbance at the SPR peak was used to determine the concentration of the AuNPs. To this end, a calibration line (

Figure 29) was produced by measuring the absorbance at 520 nm of a commercial AuNPs-citrate solution of known concentration and diameter (20 nm). The equation $y = 12.821x$, obtained from the linear regression of the calibration line was used to quantify the AuNPs

concentration after their synthesis and after following steps in the synthesis of the Aurozyme. In order to achieve a full AuNPs coverage on the surface of the SPs (described in the next section), we decided to start from a more concentrated AuNPs-citrate solution than the one obtained after synthesis, performing one cycle of freeze-drying of the AuNPs solution after synthesis. After freeze drying, the AuNPs pellet was resuspended in water in order to increase the AuNPs concentration up to ten times. The comparison of the UV-vis spectra (

Figure 29) of the AuNPs-citrate before and after freeze drying shows that the surface plasmon resonance (SPR) peak is placed at 520 nm in both curves, and that the peak profile did not show major changes after freeze drying. This confirms that the freeze-drying process did not change the properties of the AuNPs herein synthesized.

AuNPs electrostatic immobilization and enzyme co-immobilization

Considering the negative charges of citrate-capped AuNPs, we decided to chemically modify the surface of the silica in order to introduce positively charged (at neutral pH) primary amino functions. This was achieved by reacting silica particles (SPs, produced using the Stöber method,⁹³ with a diameter of 284 ± 8 nm) during 90 min with the APTES (2) at increasing concentrations 2.6, 7.8 and 26 mM. A zeta potential (ζ -potential) analysis was performed in order to detect the positive amine functions on the surface of the silica particles, after amino modification (**Table 2**). The ζ -potential study showed an increase of the charge on the surface of the SPs going from -55 mV for the bare SPs to -46, -19.2 and -9.99 mV when the concentration of the APTES (2) was 2.6, 7.8 and 26 mM, respectively. Those results confirmed that the SPs surface was modified with positive amine moieties.

Table 2. Zeta potential values of SPs functionalized with different concentrations of APTES (2).

APTES [mM]	zeta potential [mV]
0	-55.0
2.6	- 46.0
7.8	-19.2
26	-9.99

After removing unreacted APTES, the amino-modified nanoparticles SPs were further incubated with 0.3 mg mL^{-1} of AuNPs for 15 h and characterized by SEM (**Figure 30**). From the SEM micrographs, it can be clearly seen that the density of AuNPs on the surface of SPs increases with the concentration of APTES (2) used for the amino modification. A uniform AuNPs coverage (ca. 30% of the SPs surface) was reached on the SPs amino modified with 7.8 and 26 mM APTES.

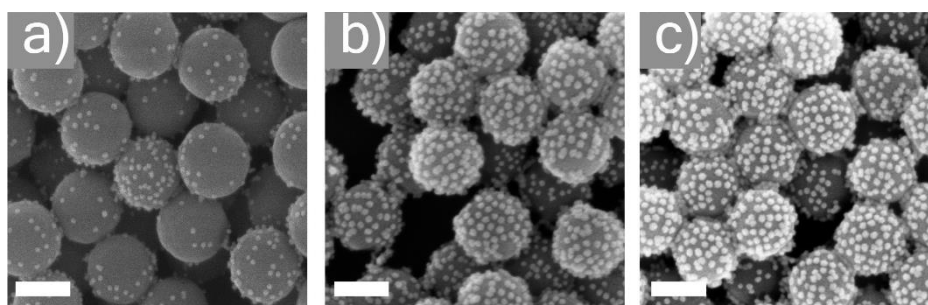


Figure 30. Characterization of AuNPs-citrate electrostatic immobilization on SPs. SEM micrographs after AuNPs immobilization on SPs functionalized with (a) 2.6 mM; (b) 7.8 mM and (c) 26 mM of APTES (2). Scale bars represent 200 nm.

The particles produced, named AuNPs-SPs from now on, were further modified in order to co-immobilize CalB on the AuNPs-SPs. To that end, we used glutaraldehyde as a homobifunctional crosslinker (methods reported in the methods section). By using a concentration of 0.097 mg mL^{-1} of CalB, we reached a substantial immobilization yield of 100%. After enzyme immobilization, the particles were characterized using SEM (

Figure 31) in order to determine whether after CalB immobilization, the AuNPs coverage on the surface of the SPs had major changes.

The SEM characterization of the particles produced, however, revealed a drastic decrease of the AuNP density at the surface of the SPs (

Figure 31). When applying the same reaction conditions, in the absence of glutaraldehyde, the density of AuNPs did not change significantly.

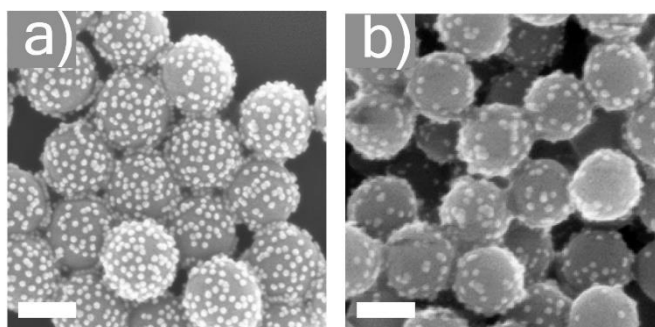


Figure 31. Characterization of AuNPs-SPs after enzyme immobilization. SEM micrographs of SPs amino modified with 26 mM APTES before (a) and after (b) enzyme-glutaraldehyde crosslinking. Scale bars represent 200 nm.

This set of results strongly suggests that the reaction of glutaraldehyde with the amino functions at the surface of the SPs suppressed the positive charge of the SP and caused the release of the AuNPs. In order to circumvent this issue and to increase the stability of the CalB-AuNPs-SPs, we decided to proceed with the covalent modification of the AuNPs on silica.

AuNPs covalent immobilization

Firstly, we performed ligand exchange experiments on the AuNPs-citrate in order to replace the citrate with cysteine (9) or with cysteamine (10) (**Figure 32**). Cysteine (9) and cysteamine (10), being biomolecules with a thiol group, are often chosen as stabilizing agent for AuNPs.¹⁹⁹⁻²⁰⁰ However, the citrate exchange reaction with the cysteamine (10) resulted in the formation of AuNPs aggregates, as confirmed by the PDI values, measured with dynamic light scattering (DLS) method, that increased from 0.1 for the AuNPs-citrate to 0.9 for AuNPs-cysteamine (data not shown). The cysteine-capped AuNPs were covalently immobilized to the surface of the amino modified SPs, using glutaraldehyde as cross-linker. Despite the extensive effort

made following this immobilization strategy, just few AuNPs-cysteine were immobilized on the surface of SPs (**Figure 32**). Therefore, an alternative strategy for AuNPs immobilization was followed.

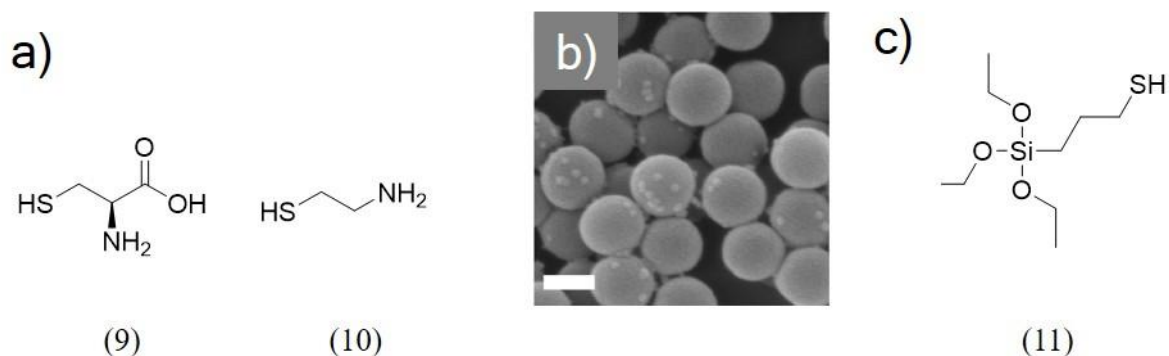


Figure 32. Characterization of AuNPs covalent immobilization on SPs. (a) Structures of L-cysteine (9) and cysteamine (10); (b) SEM micrograph of AuNPs with cysteine as capping material immobilized on amino modified SPs; (c) structure of 3-(mercaptopropyl)trimethoxysilane (MPTES) (11).

The AuNPs and enzyme co-immobilization strategy relies on the modification of the SPs surface with both amine groups, to allow further immobilization of the enzyme, and thiol groups for binding the AuNPs. To that end, we used (3-mercaptopropyl)trimethoxysilane (11) (MPTES) an organosilane bearing a thiol function (**Figure 32**), for grafting the surface of SPs with thiol moiety. The mercaptosilane (11), in the presence of amines in water solution, is hydrolyzed initiating its polycondensation reaction at the surface of the SPs. Considering that the polycondensation reaction of the silanes requires the presence of amines as catalyst, no experiments were performed with the only mercaptosilane (11) in the reaction mixture.²⁰¹ The optimization of the method for the covalent immobilization of the AuNPs on the SPs surface was carried out by reacting the SPs with three different reaction mixtures (**Figure 33**):

- a) mercaptosilane (11) and aminosilane (2) (23 mM and 26 mM),
- b) mercaptosilane (11) and ammonia (23 mM and 0.7%), used as catalyst of the silane polycondensation reaction.

c) mercaptosilane (11), aminosilane (2) and ammonia (23 mM, 26 mM and 0.7% respectively).

All the reactions were stopped by centrifugation after 1.5, 3.5, and 20 hours. Consequently, the modified SPs were incubated with AuNPs-citrate suspension for 15 hours, centrifuged and characterized via SEM.

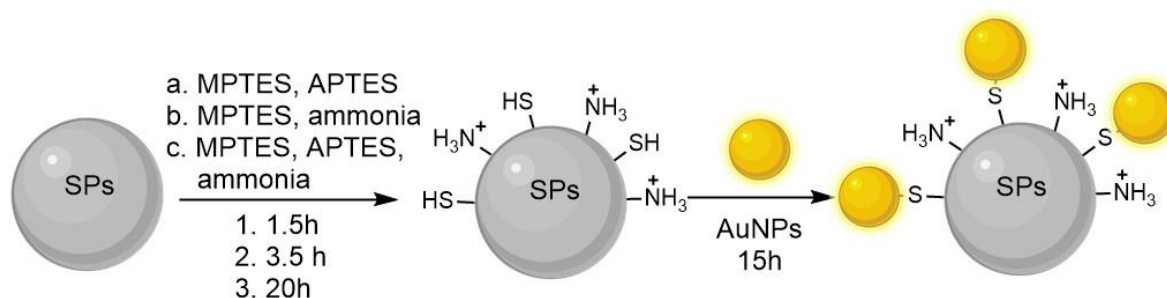


Figure 33. Schematic depiction of the strategy used to covalently bind AuNPs on SPs. SPs surface was firstly modified with -SH functions by polycondensation of MPTES in the presence of amines as catalyst. After the thiol- and amino- modified SPs were incubated with AuNPs.

The SEM characterization of the SPs after AuNPs immobilization (**Figure 34**) showed that the SPs, treated for 1.5 hours with aminosilane (2) and mercaptosilane (11), were covered with a uniform AuNPs layer with average surface coverage of ca. 40%, thus resulting in a higher AuNPs coverage in comparison to the particles coverage obtained by electrostatic immobilization of the AuNPs to the surface of the amino modified SPs (30%, **Figure 30**).

For all reaction conditions and longer reaction times (3.5 and 20 hours), while the AuNPs coverage remains high, there is an evident change in the shape and in the morphology of the SPs (**Figure 34**). This was caused by the growth of a non-uniform organosilica layer at the surface of the SPs when reacted with the organosilanes and ammonia. When the second mixture (mercaptosilane (11) and ammonia) was used to modify the SPs surface, no AuNPs immobilization was achieved. This result suggests that the presence of the aminosilane (2) on the surface of the SPs is important for the AuNPs immobilization. A potential explanation could

be that the aminosilane (2), bearing a positive charge, might play a role on attracting a major number of citrate-capped AuNPs to the SPs surface, than when no positive charges are present at the surface of the SPs. When both the aminosilane (2) and ammonia were used with the mercaptosilane (11) after 1,5 h, one can observe the formation of amorphous and larger SPs.

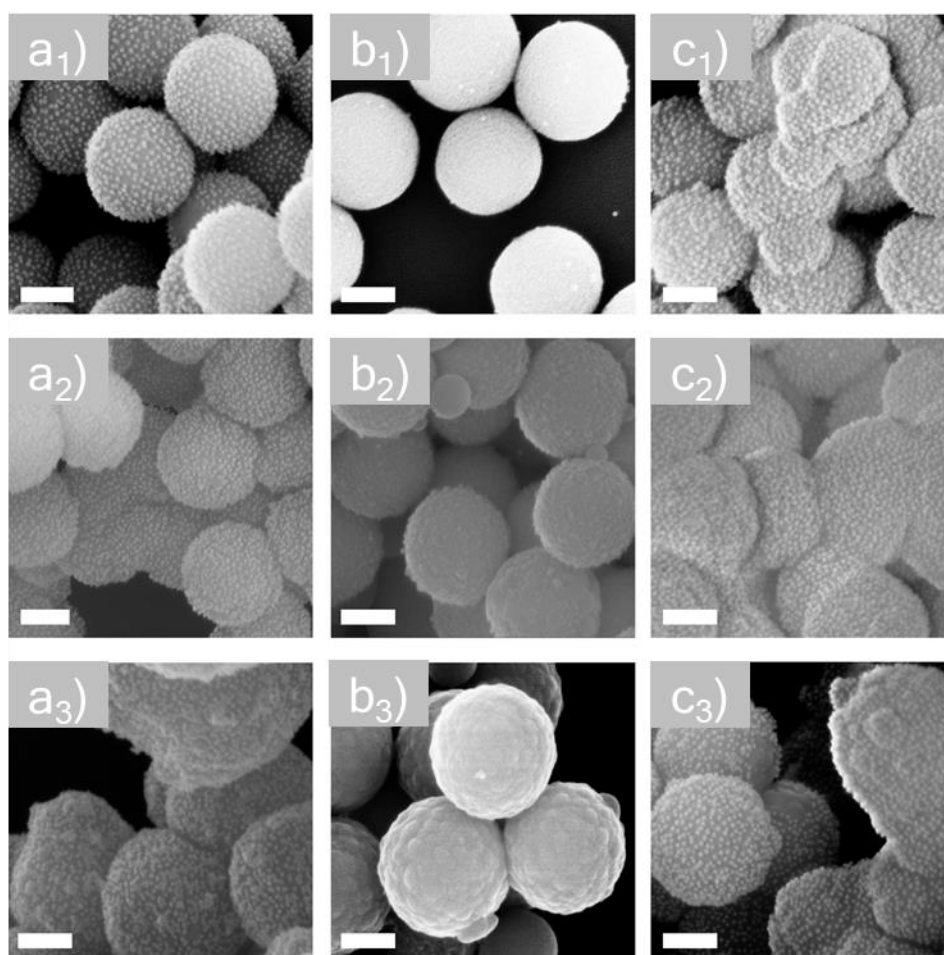


Figure 34. Characterization of AuNPs covalent immobilization on silica with thiol functions on the surface. SEM micrographs of AuNPs immobilized on SPs modified with thiol groups using three different conditions (a, b, c). The SPs were reacted with (a) MPTES and APTES; (b) MPTES and ammonia; (c) MPTES, APTES and ammonia. The reaction time was 1.5 h (a₁, b₁ and c₁); 3.5 h (a₂, b₂ and c₂) and 20h (a₃, b₃ and c₃). All scale bars represent 200 nm.

Thus, AuNP-SPs reacted with the mercaptosilane (11) and the aminosilane (2) for 1.5 hour were further characterized by UV-vis (**Figure 35**) and used as carriers for the enzyme bioconjugation (described in the following section). To determine the AuNPs immobilization yield, we measured the UV-vis spectra of the supernatant after their immobilization on SPs (**Figure 35**). The absorbance of the SPR peak of the unbound AuNPs was used for calculating

the AuNPs immobilization yield. This was done by using the linear regression equation obtained from the calibration curve of the commercial AuNPs (

Figure 29). The concentration of AuNPs detected in the supernatant after AuNPs immobilization was very low when comparing to the starting AuNPs solution. Indeed, the calculated immobilization yield was 97%, corresponding to 0.301 mg mL⁻¹ AuNPs immobilized on SPs.

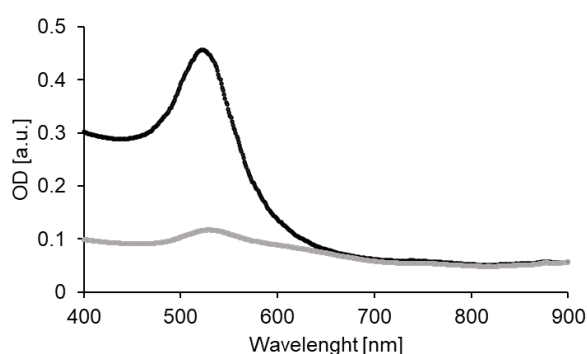


Figure 35. UV-vis characterization of AuNPs in the supernatant after AuNPs immobilization on SPs. Absorption spectra of the initial AuNPs-citrate diluted 10 times (black line) and of the supernatant after AuNPs immobilization on SPs (grey line).

Enzyme bioconjugation with AuNPs-SPs

As mentioned previously, the bioconjugation on AuNPs-SPs was carried out with two model enzymes: the β -galactosidase and the CalB. The bioconjugation, the shielding and the activity characterization methods were optimized and applied on both enzymes to confirm the versatility of our approach.

Enzyme immobilization was performed via glutaraldehyde cross-linking. To do so, the bioconjugation was carried out by reacting AuNPs-SPs amino modified with glutaraldehyde (described in the methods section). Consequently, the particles were incubated either with β -galactosidase (0.050 mg mL⁻¹) or with CalB (0.1 mg mL⁻¹). The crosslinking reaction was stopped by centrifugation. Bicinchoninic acid assay (BCA) was performed on the supernatant

to determine the enzyme immobilization yield. Immobilization yields of 76% and 66% for β -galactosidase and CalB respectively, were calculated and the particles were named as CalB-AuNPs-SPs. In order to investigate the plasmonic properties of the AuNPs co-immobilized with the enzyme, the AuNPs-CalB-SPs was used as a model system for a spectrophotometric UV-vis study (**Figure 36**).

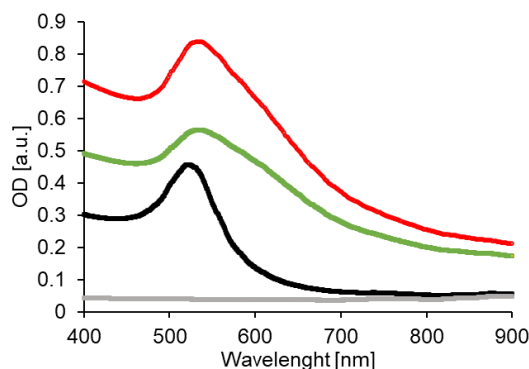


Figure 36. AuNPs-SPs characterization. Absorption spectra of the free AuNPs-citrate (black line), of the supernatant after glutaraldehyde crosslinking (grey line), of the AuNPs-SPs after glutaraldehyde crosslinking (red line) and of the AuNPs-SPs after CalB immobilization (green line).

In **Figure 36**, the UV-vis study confirms the absence of AuNPs in the supernatant after glutaraldehyde cross linking. This result suggests that the glutaraldehyde crosslinking did not induce any AuNPs leaching from the SPs surface. A shift of the SPR wavelength, from 520 nm to 534 nm after glutaraldehyde crosslinking, was observed in the absorbance spectrum of AuNPs-SPs. The SPR wavelength of AuNPs further shifted from 534 nm to 535 nm after CalB immobilization. The red shift of the SPR peak was related to changes in the AuNPs environment due to its binding, as shown in other reports.¹⁸³⁻¹⁸⁴ The increase of the SPR absorbance from 0.4 to ca. 1 in the spectra of the immobilized AuNPs, in both AuNPs-SPs and AuNPs-CalB-SPs, was related to the increase of the scattering of the whole system caused by the presence of the SPs.

Shielding of co-immobilized AuNPs-enzyme-SPs with organosilane

After enzyme bioconjugation, either the AuNP-CalB-SPs and the AuNPs- β gal-SPs were reacted with a mixture of tetraethoxysilane (TEOS) (1) and aminosilane (APTES) (2) to grow a protective organosilica shield. This was achieved by incubating AuNPs-CalB-SPs with TEOS and APTES (ratio 5/1) for 18h and AuNPs- β gal-SPs with TEOS and APTES (ratio 4/1) for 5h. The resulting samples were named as AuNPs-CalB-SP_{OS} and AuNPs- β gal-SP_{OS}. Moreover, as a control for the enzymatic activity experiments (next section), CalB and β -galactosidase were immobilized and shielded on SPs omitting the AuNPs. The resulting samples were named as CalB-SP_{OS} and β gal-SP_{OS}. The particles produced were characterized using SEM and the AuNPs-CalB-SP_{OS} was used as a model for cryo-EM analysis. Moreover, a statistical analysis of the layer thickness was performed using the SEM-micrographs to determine the PDI values (using *equation 1*) of the shielded particles and the thickness of the layers. The shield thickness on the particles was calculated using *equation 2*

$$\frac{(\bar{d})_{\text{shield}} - (\bar{d})_{\text{bare}}}{2} \quad 2$$

Where \bar{d}_{shield} is the average diameter of the shielded particles and \bar{d}_{bare} represents the average diameter of the bare SPs. The standard error on the layer thickness was calculated as

$$\frac{\frac{(\bar{d})_{\text{shield}} - \bar{d}_{\text{bare}}}{2}}{\sqrt{n}} \quad 3$$

Where n is the number of measured particles.

The complete particles characterization is shown in **Figure 37**, **Figure 38** and in **Table 3**.

On the shielding of AuNPs-CalB-SPs

In **Figure 37**, particles SEM characterization showed that the starting AuNPs-SPs displayed an average diameter of 283 nm. The AuNPs-CalB-SP_{OS} had a larger diameter (324 nm) consistent with the growth of an organosilica layer. This value corresponds to a protection layer thickness of 18 nm, confirming the shielding of the immobilized CalB and AuNPs. Moreover, the AuNPs on the surface of the SPs were no longer visible after shielding (AuNPs-CalB-SP_{OS}) and the particles surface appeared rough. Those results suggest that the AuNPs were buried within the shield and acted as a mould for the outer layer. The presence of the AuNPs underneath the layer is also confirmed from the cryo-EM micrographs, where a uniform coverage of gold nanoparticles on the surface of AuNPs-CalB-SPs and AuNPs-CalB-SP_{OS} is observed. Therefore, the immobilization of CalB and the growth of the layer did not displace the covalently immobilized AuNPs.

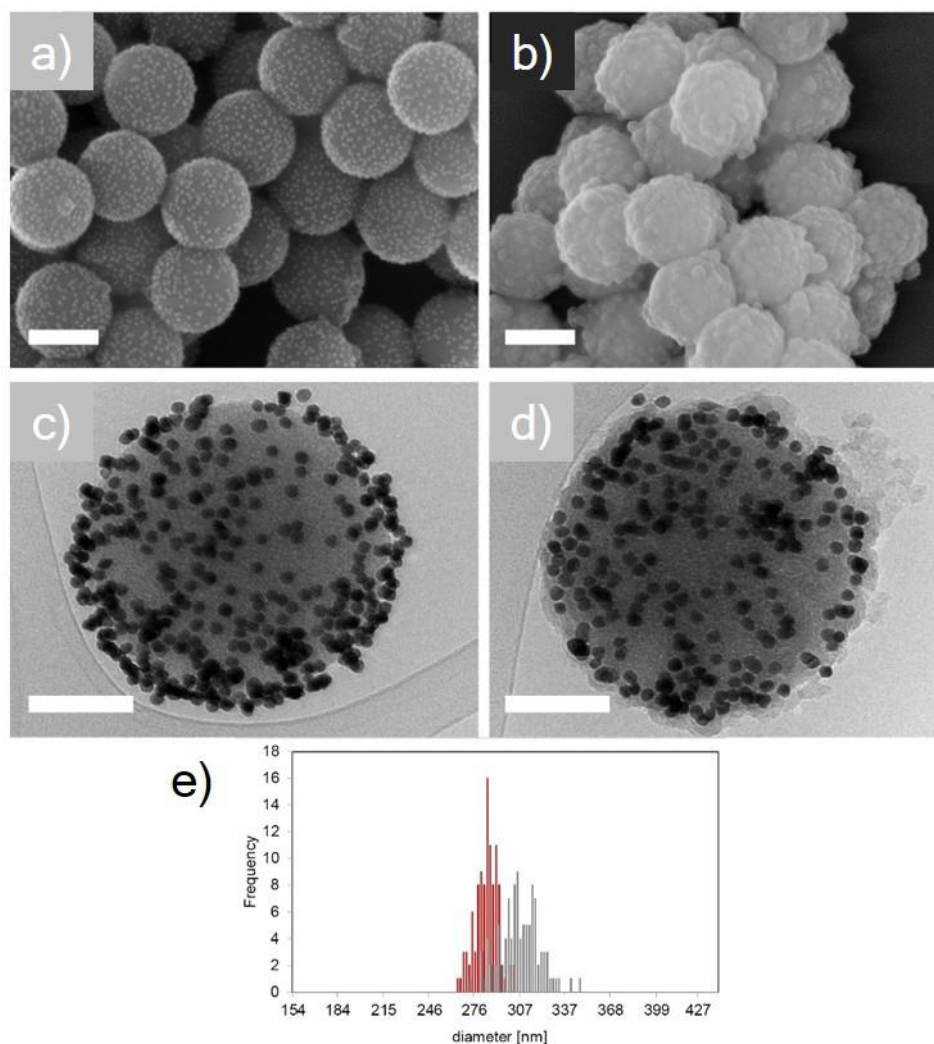


Figure 37. Nanobiocatalyst characterization. SEM micrographs of the (a) immobilized AuNPs-CalB-SPs and (b) shielded AuNPs-CalB-SP_{OS} (scale bars represent 200 nm). Cryo-EM micrographs of the (c) immobilized AuNPs on SPs and (d) shielded AuNPs-CalB-SP_{OS} (scale bars represent 100 nm). (e) Statistical distribution of bare SPs diameters (red bars) and of shielded AuNPs-CalB-SP_{OS} diameter, 106 particles were measured.

SEM characterization of the CalB-SPs and CalB-SP_{OS} (**Figure 38**) showed that the bare SPs particles had a smoother surface in comparison with the shielded particles. An increase of the diameter from 283 nm for CalB-SPs to 319 nm for CalB-SP_{OS} was measured. This increase in diameter corresponds to the growth of a layer with thickness of 18 nm. When comparing the SEM micrograph of the CalB-SP_{OS} to the one of the AuNPs-CalB-SP_{OS}, one can see that the layer surface on the CalB-SP_{OS} appears smoother than the one on the AuNPs-CalB-SP_{OS} (**Figure 37**), due to the absence of AuNPs on the surface of SPs.

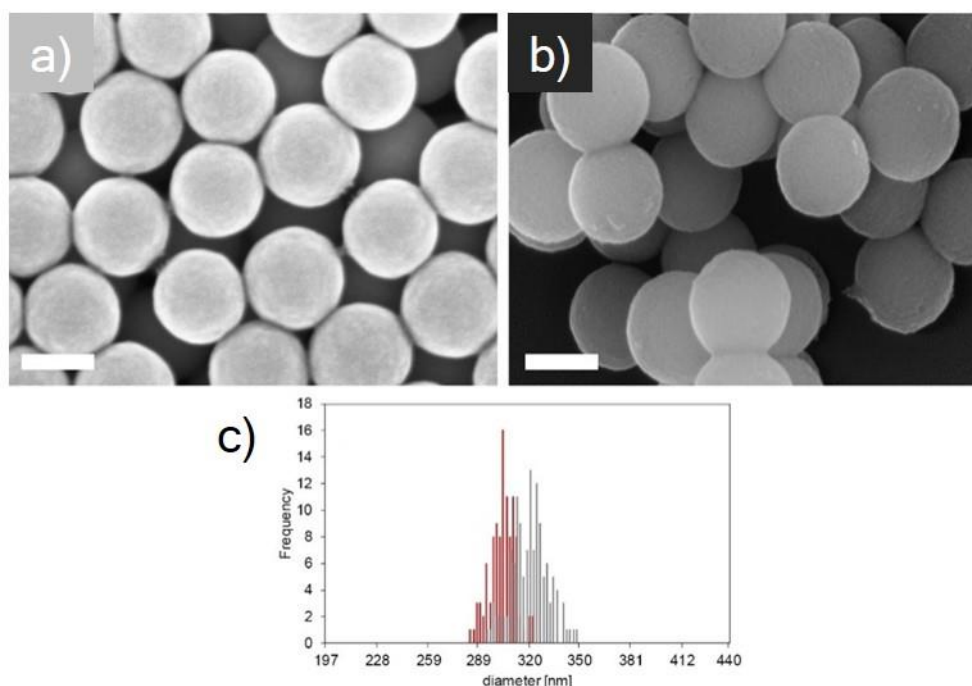


Figure 38. CalB-SPs characterization. SEM micrographs of (a) bare SPs and (b) shielded CalB-SP_{OS} used for control experiments; (c) statistical distribution of bare SPs diameters (red bars) and of protected CalB-SP_{OS} (grey bars). The average diameter of the shielded particles was 319 ± 12 nm, corresponding to a layer of 18 nm in thickness. Scale bars represent 200 nm

The statistical analysis of the diameter sizes obtained from the SEM characterization is summarized in **Table 3**. The polydispersity indices (PDI) of the free AuNPs and of the bare SPs were 0.06 and 0.027 respectively, indicating a high monodispersity of the initial particles. The statistical analysis on CalB-SP_{OS} and AuNPs-CalB-SP_{OS} revealed that PDI were 0.037 and 0.042, respectively. Considering that the PDI values of the shielded particles did not show major changes, we can conclude that the presence of the organo-silica layer did not influence the monodispersity of the initial SPs and AuNPs.

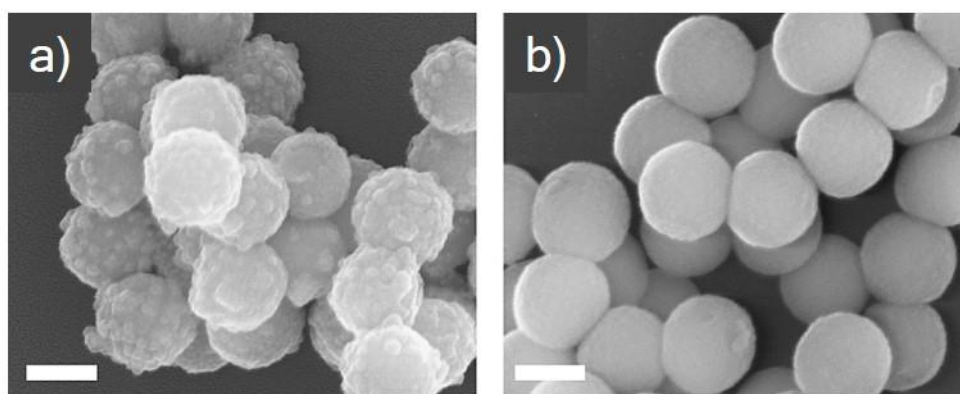
Table 3. Statistical details of AuNPs calculated using TEM micrographs and of bare SPs, CalB-SPos and AuNPs-CalB-SPos calculated using SEM micrographs.

	d (nm) $\pm \sigma$	Polydispersity index (PDI)	N. particles measured
AuNPs	18.1 ± 1.0	0.060	633
Bare SPs	283.7 ± 7.9	0.027	106
CalB-SP _{OS}	319.2 ± 12.0	0.037	106

On the shielding of AuNPs-βgal-SPs

A similar characterization study of the particles before and after shielding was performed when the enzyme used was βgal. The SEM characterization and the statistical analysis of the particles

(



c)	d (nm) ± σ	Polydispersity index	N. particles measured
		(PDI)	
Bare SPs	247.1 ± 7.0	0.028	103
βgal-SP _{Os}	280.2 ± 8.4	0.030	103
AuNPs-βgal-SP _{Os}	277.5 ± 12.6	0.045	103

Figure 39) displayed an increase of diameter from 247 nm, for the bare SPs, to 280 and 277 nm of the βgal-SP_{Os} and AuNPs-βgal-SP_{Os}, respectively. This increase of the particles diameters reflects the growth of a layer of 15.3 and 16.5 nm, respectively. As previously noticed in the SEM characterization of AuNPs-CalB-SP_{Os} (**Figure 37**), the AuNPs immobilized on the surface of the SPs are no longer visible on the shielded particles. However, the presence of the AuNPs within the layer can be suggested from the presence of a rougher surface on the AuNPs-βgal-SP_{Os} in comparison to the βgal-SP_{Os}.

The PDI values of the initial bare SPs and of the AuNPs- β gal-SP_{OS} were 0.028 and 0.045, respectively. Considering that the difference between the PDI values, was limited we can conclude that the organosilica layer did not influence the particles monodispersity, similarly to the conclusion achieved when the enzyme used was the CalB.

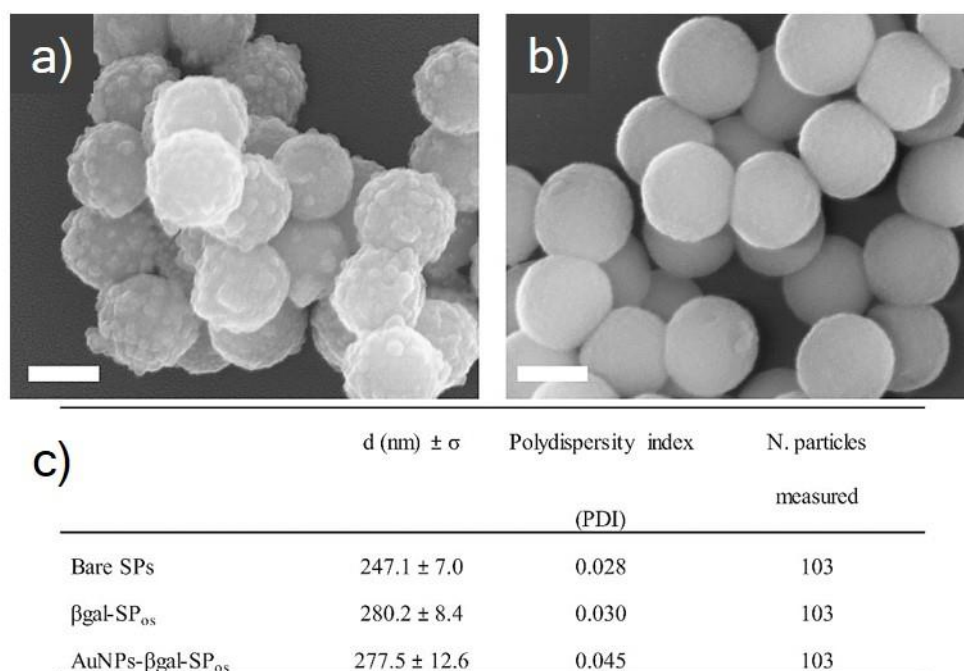


Figure 39. AuNPs- β gal-SP_{OS} and β gal-SP_{OS} characterization. SEM micrographs of (a) AuNPs- β gal-SP_{OS} and (b) β gal-SP_{OS} used for control experiments. Scale bars represent 200 nm. (c) Statistical analysis of SPs, AuNPs- β gal-SP_{OS} and β gal-SP_{OS} diameter.

Enzymes Activity characterization

An activity study of the AuNPs-CalB-SPOs and AuNPs- β gal-SPOs was performed at temperatures lower than the optimal temperatures of the corresponding soluble enzymes (T_{optimum}) of 37°C and 40°C, respectively. The aim of those experiments was to measure the activity of the enzyme co-immobilized in the vicinity of the AuNPs upon irradiation of the AuNPs. It is expected that, upon laser irradiation at the SPR (535 nm), the AuNPs convert the light into heat, thus increasing the temperature in the nearby area. As a consequence, the enzyme would experience a higher temperature in its local environment while being placed inside a bulk solution at low temperature.

The CalB activity was determined using *p*-nitrophenyl butyrate (*p*NPB) and the β -galactosidase activity was characterized using *o*-nitrophenyl β -D-galactopyranoside (*o*NPG). An extensive study of the activity at different temperatures was performed in dark conditions and under laser irradiation using the experimental set-up shown in **Figure 40**.

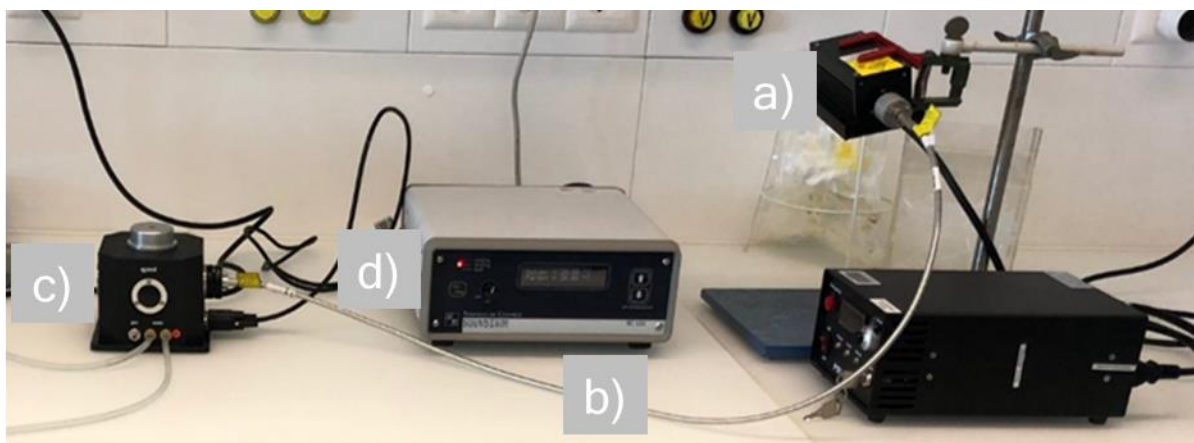


Figure 40. Experimental set-up used for laser irradiation at controlled temperature. (a) A laser (MGL-H-532nm-500mW-17111070) was connected through (b) an optical fiber (diameter 600 μm) to (c) a cuvette holder where the sample was stirred during the assay. The cuvette holder was maintained at a fixed temperature by means of (d) a temperature controller.

The activities of the shielded AuNPs-CalB/ β gal-SP_{OS} were compared to the activities of the unshielded AuNPs-CalB/ β gal-SPs in order to test the effect of the organosilica layer on the enzymatic activity upon irradiation (**Figure 41**).

On the photothermal activation of immobilized and protected CalB

Regarding CalB, the temperature was initially fixed at 10°C due to the interest in the application of lipases in clothes treatment and detergents industry.¹⁵⁶ Afterwards, the activity of the biocatalyst at lower temperatures than 10°C was studied.

In **Figure 41**, it can be seen that the activity of the immobilized enzyme, in the absence of AuNPs (CalB-SPs and CalB SP_{OS}) is not affected by the laser irradiation. When AuNPs are added, an activity increase of 118% is observed for the soluble enzyme upon irradiation. This increase is more pronounced when the enzyme is co-immobilized with AuNPs (AuNPs-CalB-SPs) with a U increase of 137% when irradiated. These results confirm the photothermal activation of the enzyme when immobilized in the vicinity of AuNPs. Remarkably, this photothermal activation is greater when both CalB and AuNPs are shielded in the organosilica layer, with an increase in activity of more than 2 U representing as much as 207% of enzyme activity activation. The broadening/lowering of the optimal working temperature range of the enzyme after shielding suggests that the heat is effectively confined in the enzyme environment by the organosilica shield. Indeed, due to its properties as insulator, the organosilica layer was expected to reduce the heat exchange with the bulk solution.²⁰²

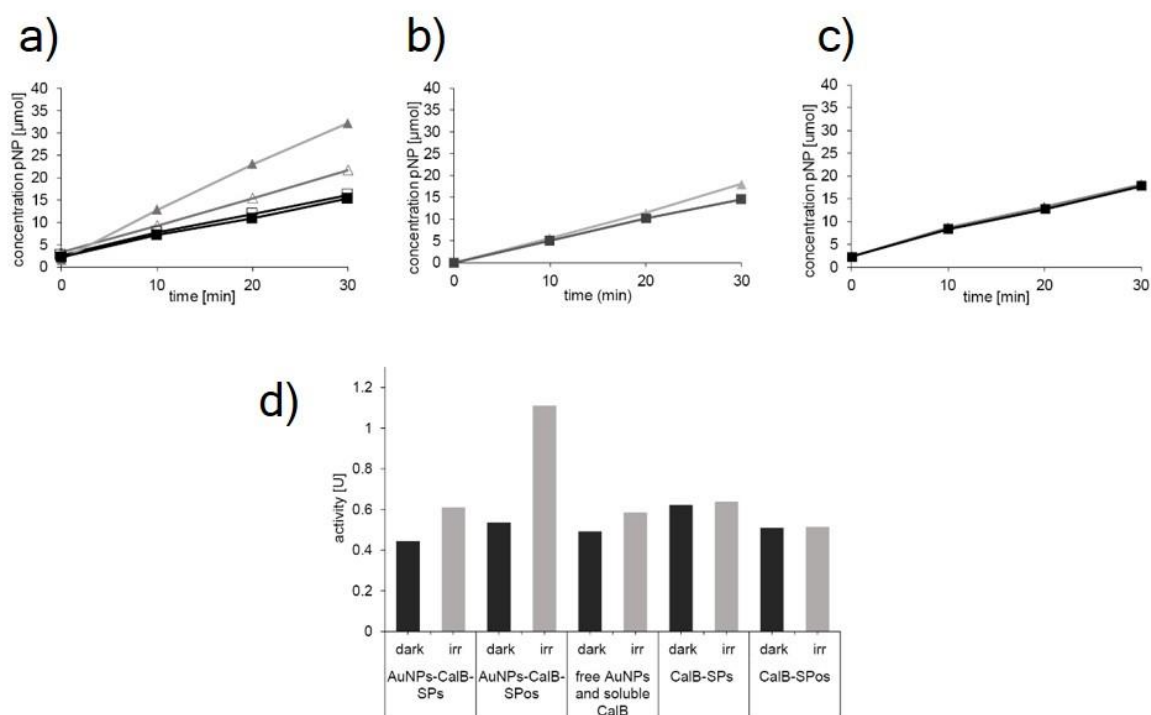


Figure 41. Activity study. Concentration of *p*-nitrophenol (*p*NP) produced by (a) AuNPs-CalB-SPs (empty symbols) and by AuNPs-CalB-SP_{os} (filled symbols); (b) a solution of soluble CalB and free AuNPs present at the same concentration than in the immobilized and protected system and by (c) CalB-SPs and CalB-SP_{os}. All kinetics were measured in dark condition (black squares) and upon laser irradiation (grey triangles) using 615 mW laser power. (d) Activities [U] calculated from the linear fits on (a), (b) and (c).

A similar activity study was performed at temperatures as lower as 0, -5, and -10°C. The activity of the AuNPs-CalB-SP_{os} biocatalyst, measured in the dark and upon irradiation at different temperatures, are reported in **Figure 42**.

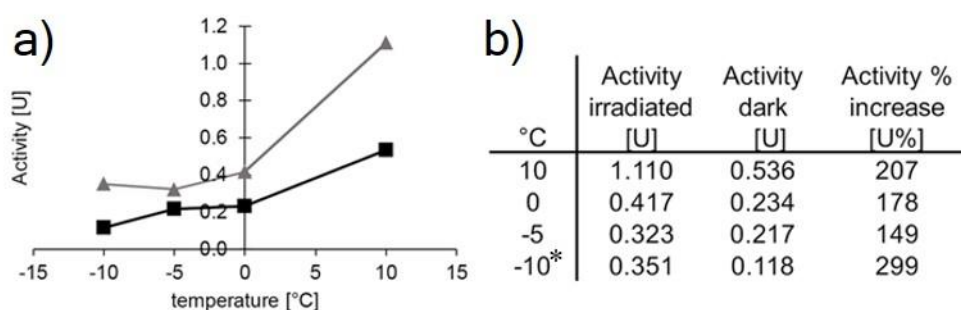


Figure 42. Activity test on CalB-AuNPs-SP_{os} at different temperatures. (a) Activity [U] of CalB-AuNPs-SP_{os} measured in the dark (black squares) and upon laser irradiation at 615 mW (grey triangles); (b) summary of activities [U] measured at different temperatures and activities % increase upon

irradiation. *the activity assay at 10°C was performed for 20 min due to the freezing of the solution, samples were tested for 30 min at the other temperatures.

As expected, the enzyme activity dropped by decreasing the temperature. However, at low temperatures the activity drop is less pronounced under irradiation. The increase of enzymatic activity upon irradiation was reduced from 207% to 149% by lowering the temperatures from 10°C to -5°C. This result was expected due to the decrease of the thermal diffusivity of the whole system. Nevertheless, in no case herein reported, the increase of activity upon irradiation was lower than 1.5 U corresponding to 149% of enzyme activation. This result confirms that the conversion of the laser light into heat, by the AuNPs, occurs at any of the temperatures reported.

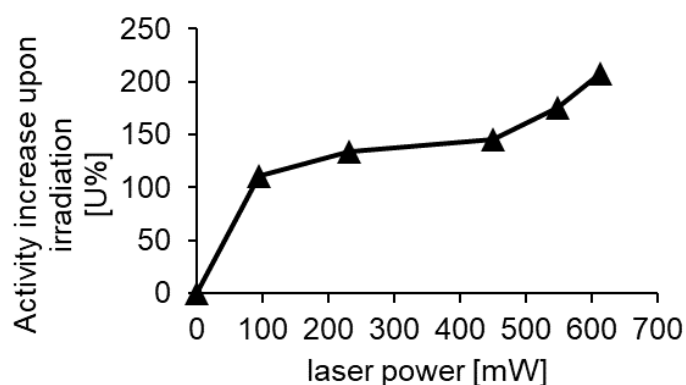


Figure 43. Activity increase [U%] upon irradiation vs laser power. Study of the AuNPs-CalB-SP_{Os} activity at 10°C using different laser power values 94, 231, 451, 548, 613 mW.

In order to study the influence of the laser power in the enzyme photothermal activation, we have measured the enzymatic activity of AuNPs-CalB-SP_{Os}, using five different laser power values. In

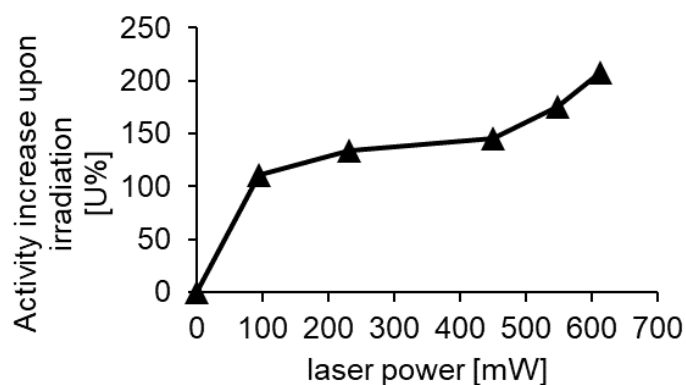


Figure 43, the percentage activity increase upon irradiation vs. the laser power is reported. As expected, the photothermal activation of the enzyme was reduced by lowering the laser power due to a lower number of photons reaching the AuNPs. Consequently, a lower amount of heat is produced and the photoactivation of the enzyme is less pronounced.

On the photothermal activation of immobilized and protected β -galactosidase

A similar activity study on the enzyme photothermal activation at low temperatures upon irradiation was performed using β gal. Similarly, the activities of the AuNPs- β gal-SPs and of AuNPs- β gal-SP_{OS} were studied in the dark and under laser irradiation conditions at 20°C and lower temperatures (15, 10, 5, 0, and -2°C). Additionally, as reported for CalB, a mixture of AuNPs and β gal as well as β gal-SPs and β gal-SP_{OS} as control experiments were tested.

In **Figure 44**, it is shown that no increase of the activity of the enzyme upon irradiation was observed when AuNPs were omitted in β gal-SPs and β gal-SP_{OS}, as previously reported for CalB. When AuNPs are added, an activity increase corresponding to 124% photothermal activation is observed for the soluble enzyme upon irradiation. This increase is more pronounced when the enzyme is co-immobilized with AuNPs (AuNPs- β gal-SPs) with a U increase of 176% when irradiated. This last set of results is in agreement to the outcomes of the CalB study previously reported. Therefore, the approach used in this work was proven to be versatile by assessing a proof of concept for both enzymes.

In contrast to what observed using CalB, the photothermal activation was lower when both β gal and AuNPs were shielded in the organosilica layer than for the unshielded counterpart, with an increase in activity of less than 1.5 U representing as much as 133% of enzyme activation.

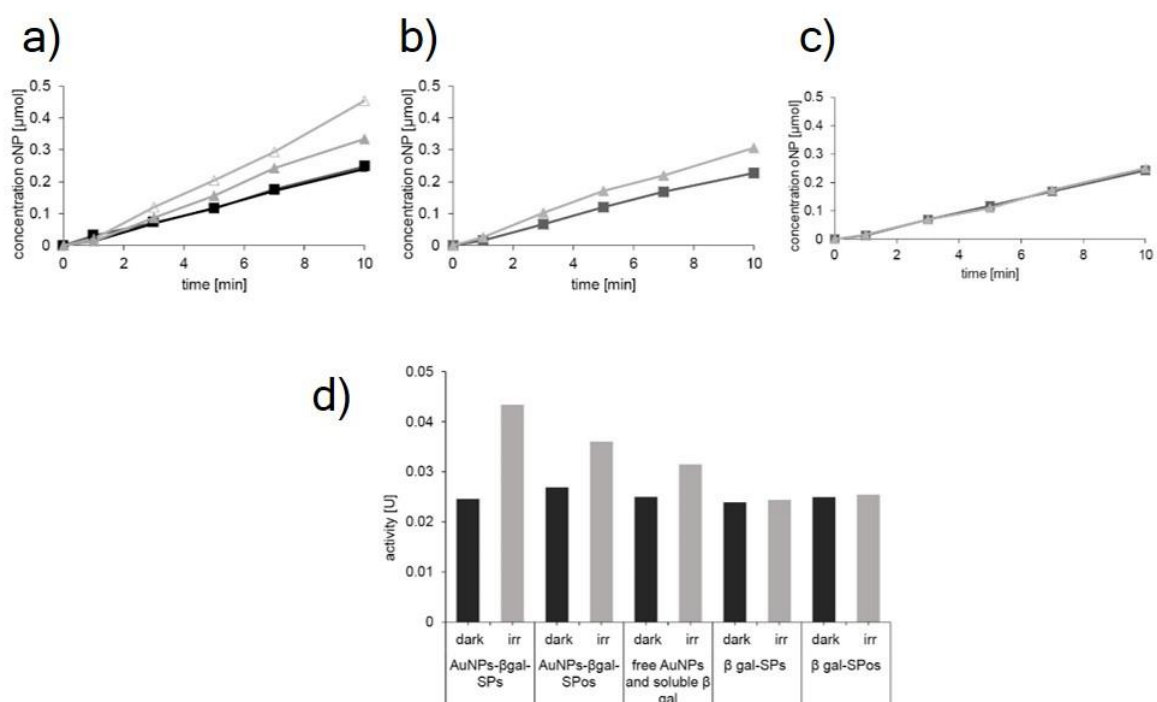


Figure 44. Activity study. Concentration of *o*-NP produced by (a) AuNPs- β gal-SPs (empty symbols) and by AuNPs- β gal-SP_{OS} (filled symbols); (b) a solution of soluble β gal and free AuNPs present at the same concentration than in the immobilized and protected particles and by (c) β gal-SPs and β gal-SP_{OS}. All kinetics were measured in dark condition (black squares) and upon laser irradiation (grey triangles) at 615 mW laser power. (d) Activities [U] calculated from the linear fit of (a), (b) and (c).

The lower photothermal enzyme activation obtained by shielding β gal in AuNPs- β gal-SP_{OS} (133%) in comparison to the one of 207% measured for the AuNPs-CalB-SP_{OS}, brings us to propose a possible hypothesis. Considering its bigger size in comparison to the CalB (

Figure 27), the β gal might be spatially closer to the AuNPs surface, in the co-immobilized system. It was proven that the surface of the AuNPs upon irradiation is a hot spot where the heat is generated and then dissipated in the surrounding environment.²⁰³ Therefore, the areas

closer to the surface of the AuNPs are the warmer spots. The hypothesis is that the vicinity of the β gal to the AuNPs surface along with the confinement of the heat by the layer might increase the temperature, in the enzyme environment, to values over 40°C, thus leading to the enzyme unfolding.²⁰⁴

To test the validity of our hypothesis, we have compared the increase of activity of AuNPs- β gal-SPs and AuNPs- β gal-SP_{OS} upon irradiation at different laser power values (**Figure 45**). It was expected that by reducing the laser power, a lower amount of heat would be released into the enzyme environment. Consequently, the temperature increase in the enzyme environment could be controlled to avoid the inactivation of the enzyme.

By reducing the laser power, the photothermal activation of the enzyme was reduced, which is in agreement with the results obtained with the CalB (**Figure 45**). Remarkably, this reduction was less pronounced when the β gal was shielded, showing 133%, 115%, and 119% of the activity increase with laser powers of 615 mW, 223 mW, and 94 mW, respectively. In contrast, the activity increase of the unshielded AuNPs- β gal-SPs upon irradiation was 94% setting the laser power at 94 mW, thus counting the 25% less enzyme photothermal activation in comparison to the shielded counterpart.

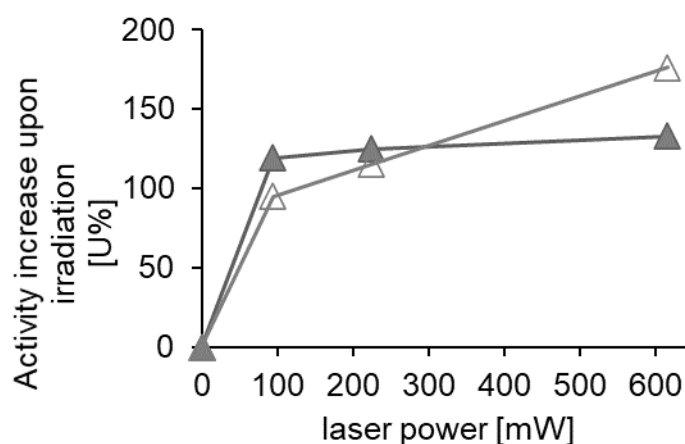


Figure 45. U% increase of AuNPs- β gal-SPs and AuNPs- β gal-SP_{os} upon irradiation vs. laser power. The activity study was performed using 94, 223 and 615 mW laser power. AuNPs- β gal-SPs (empty symbols) and AuNPs- β gal-SP_{os} (filled symbols).

Therefore, the best result in terms of higher activity increase were achieved with laser powers of 615 mW for the unshielded AuNPs- β gal-SPs and of 94 mW for the shielded AuNPs- β gal-SP_{os}. This result supports the hypothesis for which the irradiation of the AuNPs leads to the partial inactivation of the β gal when the enzyme is shielded. It was expected indeed, that by reducing the laser power the heat produced would have been restricted, thus avoiding hindering of the protein activity upon laser irradiation.

As the highest photoactivation of β gal upon irradiation was measured at 20°C and 615 mW laser power with the AuNPs- β gal-SPs, we decided to use this biocatalyst to investigate its activity at lower temperatures upon laser irradiation (**Figure 46**).

As previously observed using CalB, the activities measured are higher upon irradiation than in dark conditions, proving that the photothermal activation of the enzyme occurs at any of the temperatures investigated. Interestingly, the activity increase at different temperatures seems to be constant with an average of 186%, in contrast to the CalB study where the photoactivation of the enzyme was reduced by lowering temperatures. This result was unexpected considering that the thermal diffusivity of the whole system is reduced at lower temperatures. A possible explanation might be that the β gal was immobilized closer to the AuNPs surface, in comparison to CalB, therefore the reduced thermal diffusivity was not a limiting factor in the range of temperatures investigated.

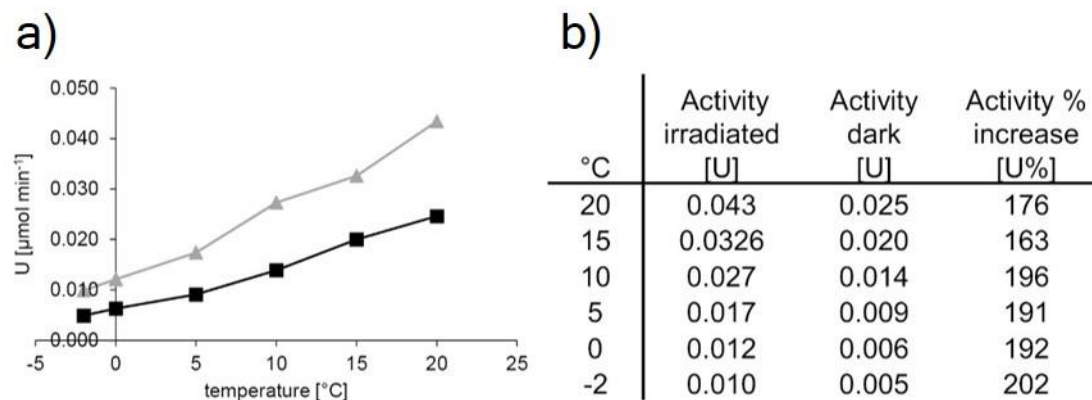


Figure 46. Activity test on AuNPs- β gal-SPs at different temperatures. (a) Comparison of activity [U] of AuNPs- β gal-SPs measured in the dark (black squares) and upon laser irradiation at 615 mW (grey triangles); (b) summary of activities [U] measured at different temperatures and activities % increase upon irradiation.

4 CONCLUSIONS

The covalent immobilization of the AuNPs was optimized. The AuNPs were uniformly co-immobilized with CalB or β gal on the surface of SPs and shielded with an organosilica layer. The full coverage of AuNPs was maintained during all synthetic steps showing no AuNPs leaching, as confirmed by the cryo-EM characterization and UV-vis spectroscopy.

The proof of concept was assessed with two different enzymes: CalB and β gal. The CalB and β gal activity were increased via irradiation of AuNPs at 10°C and 20°C, respectively, endowing the enzymes with two-fold the activity that their soluble counterparts show at these temperatures. Differences in the enzyme photothermal activation were noticed when the co-immobilized AuNPs-enzyme-SPs were shielded with an organosilica layer. The presence of the organosilica layer increased the activity of the CalB up to 1.4-fold, in comparison to the unshielded counterpart, upon irradiation with 615 mW laser power. A similar result was obtained with the shielded β gal by reducing the laser power to 94 mW. Thus, we can assume that the organosilica protection layer thermally insulated the whole system. Interestingly, activations of CalB and β gal down to -10°C and -2°C respectively, were reported.

This work contributes to the implementation of methods aimed to empower enzymes at low temperature. The methods reported in this chapter were proven to be versatile for two structurally different enzymes opening new prospects for the development of the Aurozyme with other enzymes of interest.

CHAPTER 5

CONCLUSIONS AND OUTLOOK

1 CONCLUSION

The research work of this PhD thesis allowed the development of a synthetic strategy to produce new nanobiocatalysts showing remarkable enantioselectivity, high substrate promiscuity and outstanding stability in organic solvent. This synthetic strategy additionally enabled the production of the Aurozyme; a biocatalyst with increased stability at low temperatures. The core of the strategy, herein described, lies in the modification of the enzyme environment by enzyme immobilization and, in its encapsulation in a protective shell, which is chemically and physically tuneable.

The encapsulation of different, supramolecularly engineered, supported enzymes with an organosilica layer allowed establishing a nano-environment in which the investigated enzymes were endowed with enantioselectivity and enhanced stability when biocatalysis was performed in organic solvents or at low temperatures. The rational design of diverse encapsulating layers was expected to affect differently the above-mentioned enzyme properties. This hypothesis was confirmed from the differences in enantioselectivity enhancement measured upon shielding of an esterase with a material showing both hydrophobic and hydrophilic moieties. Including hydrophobic moieties in the shielding material, such as benzyl and butyl functional groups, has led to a remarkable enhancement of the enantioselectivity. In contrast, the increase of the hydrophilicity of the shield material resulted in limited changes in the enantioselectivity of the enzyme. Those results lead to the conclusion that different nano-environments were

created upon diverse interactions of the enzyme with the shielding layers. Specifically, the author speculates that the presence of hydrophobic moieties in the protection layer contributed on establishing a more favourable conformation of the enzyme. Additionally, the biocatalysts displaying the highest enantioselectivity values were also shown to be the most stable in organic solvent as well. To justify this result, it is hypothesized that multipoint interactions of the enzyme surface with the surface of the shielding material endorsed the enzyme with enantioselectivity and also contributed to its rigidification thus reducing the risk of enzyme denaturation, which typically occurs in organic solvent. Moreover, the encapsulation of immobilized enzymes was showed to be the method of choice to improve enzyme stability at low process temperatures (from 20 to -10°C) establishing a warmer enzyme environment upon AuNPs light activation.

In the frame of this doctoral research work, the versatility and the reproducibility of the strategy based on enzyme environment modification, herein reported, were established and validated. The findings of this doctoral research work further support the use of this approach as an alternative to other methods (including protein engineering and chemical enzyme modification) aimed at the modification of enzyme properties (i.e., enantioselectivity, stability in organic solvents and at low temperature).

2 OUTLOOK

The design of novel supported biocatalysts demands the investigation of the changes in the enzyme structure under different and confined environmental conditions. The development of novel techniques that allow full characterization of the active site of the supported enzymes is needed. The availability of such analytical tools would contribute for a better understanding of the modification of the enzyme structure upon immobilization, opening new routes for the optimization of immobilization processes. In this context, cryo-EM, which recently came to

the fore for protein structure determination, could be applied for the determination of the enzyme structure upon immobilization. The usage of support materials displaying high transparency, and compatible with enzyme immobilization, would support image acquisition of the supported enzyme conformation, thus contributing for the generation of valuable knowledge on modification of enzyme properties by means of bioconjugation methods. To address this potential, hollow silica nanoparticles are currently under investigation in the laboratory where this PhD research was carried out. Along with the information on the supported enzyme structure, the investigation of the local environment at the enzyme-support interface (e.g., temperature, pH) is of significant importance for the development of novel materials pertinent to enzyme immobilization. To this aim, immobilization of probe molecules on the surface of the silica particles or into the organosilica layer, and responding to environmental changes, should be addressed. Regarding further development of Aurozyme, the co-immobilization of thermosensitive molecules with the enzyme and AuNPs on the surface of the SPs could be used as a nanothermometer upon AuNPs activation. By applying this strategy, the increase of temperature in the local proximity of the enzyme could be monitored and fine-tuned to improve the performance of the Aurozyme. Finally, the activation of AuNPs by means of more cost-effective light sources, such as light-emitting diodes (LEDs), would further trigger the implementation of the Aurozyme for industrial applications (e.g., food industry for reducing microbial contamination, or detergent industry to overcome issues coming from enzyme inactivation at low temperatures).

CHAPTER 6

EXPERIMENTAL METHODS

MATERIALS SYNTHESIS

Materials and methods related to Chapter 3 are provided in the Annex as Supporting Information of the submitted manuscript titled “*Tuning the Properties of Natural Promiscuous Enzymes by Engineering their Nano-Environment*”. Next sections report the materials and characterization methods used in Chapter 4.

1 SILICA PARTICLES SYNTHESIS (SPs)

Silica Nanoparticles were synthesized by adapting the procedure described by Stöber.⁹³ Ethanol (345 mL) and ammonium hydroxide (40 mL, 28-30%) were mixed in a round bottom flask (1 L) and equilibrated under stirring (20°C, 600 rpm, 1h). TEOS (1) (15 mL) was added to the solution and kept under stirring (18 h). The produced suspension was centrifuged (3220 x g, 10 min), the supernatant was discarded, and the white pellet was resuspended in ethanol. This operation (hereinafter called “washing cycle”) was repeated two additional times in water. The resulting SPs suspension was then stored at 4°C prior to further use. The concentration of the SPs was determined by measuring the weight of the pellet after freeze-drying.

2 GOLD NANOPARTICLES SYNTHESIS (AuNPs)

Gold Nanoparticles were synthesized following the Turkevich method.¹⁶⁷ Briefly, water (100 mL) was warmed up (90°C) under reflux. A solution of sodium citrate tribasic dihydrate (2.5

mL, 34 mM) was added to the warm water and let to equilibrate (90°C, 5 min). A solution of gold (III) chloride hydrate (1mL, 25 mM) was added into the citrate solution and let to react (17 min) until the colour of the solution changed from yellow to red wine. Finally, the solution was left to cool down at room temperature prior to further use.

Sucrose (5% (w/v)) was added To the AuNPs solution and let to solubilize under stirring. The solution was freeze-dried (17 h) and the AuNPs were then resuspended in water (10 mL) and stored at room temperature. The AuNPs prior and after freeze drying where analysed via UV-vis.

3 GOLD NANOPARTICLES IMMOBILIZATION ON SPs

In order to electrostatically absorb the AuNPs, the surface of the SPs was chemically modified introducing primary amino functions. The silica particles (18 mL, 3.2 mg mL⁻¹, diameter of 284 ± 8 nm) where reacted during 90 min with (3-aminopropyl)triethoxysilane (APTES) (2) at increasing concentrations (0.047, 0.141, 0.470 mmol). After removing unreacted APTES, the amino-modified nanoparticles were further incubated with 0.310 mg mL⁻¹ of AuNPs for 15 h and characterized by SEM. An aliquot of the solution was taken (1.5h, 3.5 h and 15h), centrifuged (3220 x g, 5 min) and the supernatant was analysed via UV-vis in order to calculate the AuNPs immobilization yield.

For the covalent immobilization of AuNPs, SPs (18 mL, 3.2 mg mL⁻¹, diameter of 284 ± 8 nm) were incubated under stirring (20°C, 400 rpm) with the MPTES (11) (0.47 mmol, 10 min), then the APTES (2) (0.42 mmol) was added into the SPs solution and left to react (1.5 h). The so modified SPs were then centrifuged (3220 x g, 10 min), the supernatant was discarded, and the white pellet was resuspended in ethanol. After two washing cycles in ethanol, the modified SPs were washed and resuspended in water (18 mL). The suspension was then stored in a water bath (20°C, 20 h) prior use. The mercapto- and amino-modified SPs suspension (10 mL) was

incubated with the AuNPs solution (0.310 mg mL^{-1}) in a glass vial under stirring at room temperature (100 rpm, 20h). The AuNPs-SPs solution was then centrifuged ($3220 \times g$, 5 min), the supernatant was kept for determining the AuNPs immobilization yield via UV-vis measurement and the particles were resuspended in water (10 mL). The washing cycle in water was repeated three times in total.

4 B-GALACTOSIDASE AND CALB IMMOBILIZATION ON AuNPs-SPs

β -galactosidase was co-immobilized on the AuNPs-SPs by means of glutaraldehyde as cross-linker. Thus, AuNPs-SPs (10 mL) were reacted with glutaraldehyde (0.1% (v/v)) in a water bath under stirring (20°C , 30 min, 400rpm). The suspension was then centrifuged ($3220 \times g$, 5 min), the supernatant was discarded, and the pellet was resuspended in water. After two washing cycles in water the particles were resuspended in 2-(N-morpholino)ethanesulfonic acid (MES) buffer (9 mL, 10 mM, pH 6.2) with MgCl_2 (5mM). A solution of β -galactosidase (1 mL , $500 \mu\text{g mL}^{-1}$) was added to the AuNPs-SPs and incubated under stirring (20°C , 1h, 400 rpm). After enzyme immobilization an aliquot (1 mL) was removed from the solution, centrifuged ($350 \times g$, 10 min), and the supernatant was kept for protein quantification assay by means of BCA assay. The pellet was resuspended in potassium phosphate buffer (1mL, 100 mM, pH 6.5) and MgCl_2 (5 mM) and used for enzyme activity characterization (see Characterization Methods). The concentration of the unbound enzyme was extrapolated from the BSA calibration curve.

Similar procedure was used for the immobilization of the CalB (1 mg mL^{-1}) using potassium phosphate buffer (10 mM, pH 6) and polysorbate 80 (8 mg L^{-1}).

5 AuNPs-ENZYME-SPs SHIELDING

β gal ($38 \mu\text{g mL}^{-1}$) and CalB ($63 \mu\text{g mL}^{-1}$) were immobilized according to the procedures described above. Consequently, the shielding was performed following a method previously

reported.¹²¹ β gal-SPs and CalB-SPs were incubated with TEOS (1) (0.360 mmol, 0.450 mmol respectively) and allowed to react in a water bath (20°C, 1h, 400 rpm). Subsequently, the aminosilane (2) (0.090 mmol) was added. The polycondensation reaction was stopped after 18h by washing the particles three times in the potassium phosphate buffer (100 mM, pH 6.5, 5 mM MgCl₂ for β gal-SPs and 10 mM, pH 7.4 for CalB-SPs) and stored at 20°C for 18 h. The particles were finally stored (4°C) for further analysis.

CHARACTERIZATION METHODS

6 SCANNING ELECTRON MICROSCOPY AND PARTICLE SIZE MEASUREMENT

Particles were imaged using a Zeiss SUPRA® 40VP scanning electron microscope. A drop (2 μL) of sample was spread on silicon wafer substrates previously cleaned with ethanol, dried (37°C), and sputter-coated with a gold-platinum alloy (15s, 15 mA). Micrographs were acquired using the InLens mode with an accelerating voltage of 10kV. Particle sizes were measured on micrographs acquired at a magnification of $150,000\times$ using the $\text{\textcircled{R}}$ AnalySIS software package. At least one hundred measurements were carried out for each sample

7 CRYO-TRANSMISSION ELECTRON MICROSCOPY (cryo-TEM)

An aliquot ($4\mu\text{L}$) of sample was adsorbed onto holey carbon-coated grid (Lacey, USA), blotted (3 s) with filter paper and plunge-frozen into liquid ethane (-180°C) using a vitrobot (FEI, USA). Frozen grids were transferred onto a CM200 FEG microscope (Philips, Netherlands) using a Gatan 626 cryo-holder (Gatan, USA). Electron micrographs were recorded at an accelerating voltage of 200 KV using low-dose system (20 to $30\text{ e}^-/\text{\AA}^2$, -175°C). Defocus values were $-4\text{ }\mu\text{m}$. Micrographs were recorded on $4\text{K} \times 4\text{K}$ TemCam-F416 CMOS based camera (TVIPS, Germany).

8 ENZYME ACTIVITY ASSAY AND IRRADIATION OF GOLD NANOPARTICLES

The enzymatic activity of β -galactosidase was tested via colorimetric assay using *o*-nitrophenyl- β -D-galactopyranoside (ONPG) as substrate. A solution of *o*NPG (21 mM, 900 μL) in phosphate buffer (100 mM, pH 6.5 with MgCl_2) was added inside a poly(methyl methacrylate) (PMMA) cuvette. The *o*NPG solution was left to equilibrate, at the chosen

temperature (5 min at 20, 10, 5, 0, and -2°C), under stirring inside a cuvette holder (Ocean Optics, qpod Temperature-Controlled Sample Compartment for Fiber Optic Spectroscopy) connected with a temperature controller. Afterward the enzyme solution (38 $\mu\text{g mL}^{-1}$, 100 μL) was added in the cuvette. Simultaneously, the laser (MGL-H-532nm-500mW-17111070) irradiation was started using different laser power (94, 223 and 615 mW) for the duration of the entire activity assay (10 min). The reaction was stopped (after 1, 3, 5, 7 and 10 min) by adding an aliquot of the reaction solution (100 μL) to a solution of Na_2CO_3 (1M, 200 μL). After centrifugation (16100 x g, 1 min), the amount of produced *o*-nitrophenol (*o*NP) was determined by measuring the absorbance of the solution (420nm, 200 μL) in a 96 well-plate using a Synergy H1 (BioTek). The catalytic activities were calculated using the molar extinction coefficient of *o*-nitrophenol ($\epsilon_{420\text{nm}} = 4300 \text{ M}^{-1} \text{ cm}^{-1}$) measured by preparing a standard curve using the same buffer.

Similarly, the enzymatic activity of the CalB activity was determined using a colorimetric assay as reported by Sigma (Enzymatic Assay of lipoprotein lipase (EC 3.1.1.34)) with some modifications. A solution of *p*-nitrophenyl butyrate (*p*NPB) (30 mM, 900 μL) in phosphate buffer (10 mM, pH 7.4), Triton X-1000 (5% (v/v)) and isopropanol (10% (v/v)) was added inside a PMMA cuvette and incubated at the chosen temperatures (5 min at 10, 0, -5, -10°C) under stirring. Afterwards the enzyme solution (63 $\mu\text{g mL}^{-1}$, 100 μL) was added to the substrate solution, the laser (MGL-H-532nm-500mW-17111070) irradiation was started using different laser power (94, 231, 451, 548, 613 mW) for the duration of the entire activity assay (30 min). The reaction was stopped (every 10 min) by centrifugation (16100 x g, 1 min, 200 μL). The amount of produced *p*-nitrophenol (*p*NP) was determined by measuring the absorbance of the solution (410nm, 200 μL) in a 96 well-plate using a Synergy H1 (BioTek). The catalytic activities were calculated using the molar extinction coefficient of *p*-nitrophenol ($\epsilon_{410\text{nm}} = 4469 \text{ M}^{-1} \text{ cm}^{-1}$) measured by preparing a standard curve using the same buffer.

The activity of the soluble enzymes, of the immobilized and of the protected enzymes were tested as described under laser irradiation and in dark conditions (without laser irradiation) as control experiments using the same reaction conditions. For the reactions carried at lower T than 0°C the qpod holder was connected to a flux of air in order to avoid humidity formation on the walls of the cuvette. Additionally, the temperature of the solution was previously measured with a thermocouple (type K) before to add the enzyme solution.

CHAPTER 7

ANNEX

Supporting Information

Tuning the Properties of Natural Promiscuous Enzymes by Engineering their Nano-Environment

Carolina I. Giunta, Isabel Cea-Rama, Sandra Alonso, Manon L. Briand, Rafael Bargiela, Cristina Coscolín, Philippe F.-X. Corvini, Manuel Ferrer, Julia Sanz-Aparicio*, and Patrick Shahgaldian**

Keywords: nanoparticles, supramolecular engineering, enzymes, organosilica, biocatalytic promiscuity.

Table of Contents

<u>Methods</u>	117
<u>Materials</u>	117
<u>Enzyme production</u>	117
<u>Enzyme immobilization optimization</u>	118
<u>Enzyme shielding</u>	119
<u>Scanning electron microscopy and particle size measurement</u>	119
<u>Cryo-transmission electron microscopy (Cryo-TEM)</u>	119
<u>Ester bond hydrolysis activity assessment</u>	120
<u>Gas chromatography (GC) analysis for determination of chiral selectivity</u>	121
<u>Stability tests and HPLC conditions</u>	122
<u>Crystallization and X-ray structure determination of EH₃ and EH₃ complexed with a derivative of butyl 4-nitrophenyl hexylphosphonate</u>	123
<u>Accession codes</u>	124
<u>Supporting figures</u>	125
<u>Supporting Tables</u>	132

Methods

Materials

Tetraethyl orthosilicate [TEOS (T), $\geq 99\%$], (3-aminopropyl)triethoxysilane [APTES (A), $\geq 98\%$], ammonium hydroxide (ACS grade, 28–30%), ethanol (ACS grade, anhydrous), glutaraldehyde (grade I, 25% in water) from Sigma-Aldrich (Switzerland). Protein assay dye reagent concentrate was purchased from Bio-Rad. *n*-butyltriethoxysilane (Bu) 95%, benzyltriethoxysilane (Bz) 95%, hydroxymethyltriethoxysilane (Hm) 50% in ethanol and 1-[3-(trimethoxysilyl)propyl]urea (Ur) 97% were purchased from ABCR (Germany). All chemicals were used without further purification. Silica nanoparticles (SPs) were prepared using the previously published procedure.²⁰⁵

Enzyme production

The vector pBXNH3 and the host *Escherichia coli* MC1061 were the source of the His₆-tag serine ester hydrolase EH₃. The vector pET46 Ek/LIC and the host *Escherichia coli* BL22 were the source of the His₆-tag EH_{1A1} and EH₇.¹²⁸ All the recombinant proteins were expressed with His-tags and purified as follows. Briefly, selected *E. coli* clones were grown at 37°C on solid Luria Bertani (LB) agar medium supplemented with ampicillin (100 $\mu\text{g mL}^{-1}$). A single colony was picked and used to inoculate (10 mL) of LB broth supplemented with (100 $\mu\text{g mL}^{-1}$) ampicillin in a 0.25 L flask, followed by cultivation at 37°C and 200 rpm overnight. Subsequently, a volume of 10 mL of this culture was used to inoculate LB medium (0.5 L) supplemented with ampicillin, which was then incubated at 37°C until the culture reaches an OD_{600nm} of ca. 0.7 (ranging from 0.55 to 0.75). Protein expression was induced by adding L-arabinose to a final concentration of approx. 0.1% (in case of vector pBXNH3) or isopropyl β -D-1-thiogalactopyranoside to a final concentration of approx. 1 mM (in case of vector pET46 Ek/LIC), followed by incubation for 16 h at 16°C. The cells were harvested by centrifugation at 5000 \times g for 15 min to yield a pellet of 2-3 g (wet weight). The wet cell pellet was frozen at -86°C overnight, thawed and resuspended in sodium phosphate (15 mL, 50 mM, pH 8.0,

imidazole 10 mM and NaCl 300 mM). Lysonase Bioprocessing Reagent (Novagen, Germany) was added to $4 \mu\text{l g}^{-1}$ wet cells and incubated for 60 min on ice submitted to rotating mixing. The cell suspension was sonicated (5 min) and centrifuged ($15000 \times g$ for 15 min at 4°C), and the supernatant was retained. The soluble His-tagged protein was purified at 4°C after binding to a Ni-NTA His-Bind resin (Sigma) and elution with sodium phosphate (50 mM, pH 8.0, imidazole 250 mM and NaCl, 300 mM). Eluted protein was subjected to ultra-filtration through low-adsorption hydrophilic 10,000 nominal molecular weight limit cutoff membranes (regenerated cellulose, Amicon) to concentrate the protein solution. An extensive dialysis of protein solutions against (4-(2-hydroxyethyl)-1-piperazineethanesulfonic acid (HEPES) buffer (40 mM, pH 7.0) was then performed using Pur-A-Lyzer™ Maxi 1200 dialysis kit (Sigma Chemical, USA), as follows. Five mL concentrated protein solution was dialyzed against (2 L) buffer during 1 hour at room temperature, after which the buffer was changed by other (2 L) buffer and maintained 1 hour more. Then, the buffer was changed, and the dialysis was kept overnight at 4°C . The dialyzed protein solution was recovered and concentrated. Purity was assessed as $>98\%$ using SDS-PAGE analysis in a Mini PROTEAN electrophoresis system (Bio-Rad).

Enzyme immobilization optimization

All reactions were carried out in glass vials (20 mL) under moderate magnetic stirring (400 rpm). To a suspension of SPs (3.2 mg mL^{-1} , 18 mL), was added APTES (11 μL , 0.047 mmol) at 20°C under stirring (400 rpm). After 90 min of reaction, the suspension was centrifuged ($3220 \times g$, 10 min), the resulting pellet was suspended in water. This operation (hereinafter referred to as “washing cycle”) was repeated twice. The so-modified SPs were then incubated with an aqueous solution of glutaraldehyde (30 min, 18 mL of 0.1% (v/v)) and subsequently submitted to two washing cycles in water. The resulting pellet was suspended in potassium phosphate buffer (18 mL, 50 mM KPi, pH 7.5) and reacted, at 20°C , with different EH_3

concentration (**Figure 49** Annex) for 1 h to produce EH₃-SPs. The particles were centrifuged at 350 x g for 10 min and resuspended in potassium phosphate buffer (50 mM KPi, pH 7.5). The supernatant was used for the quantification of the unbound EH₃ by means of BCA assay. The concentration of the unbound enzyme was extrapolated from the EH₃ calibration curve.

Enzyme shielding

In order to produce the samples called EH₃-T/A_[1/1], EH₃-T/A_[4/1], EH₃-T/A_[6/1], EH₃-T/A_[10/1], EH₃-TBz/A_[4/1], EH₃-TUr/A_[4/1], EH₃-TBu/A_[4/1], EH₃-THm/A_[4/1], and EH₃-TBzUrBuHm/A_[4/1], the EH₃ (100 µg mL⁻¹) was immobilized according to the procedure described above. Consequently, the shielding was performed following the method previously published.⁷⁶ TEOS and all the other silanes were added to the reaction mixture according to the quantities reported in **Table 5** and allowed to react under moderate stirring (1h, 20°C, 400 x g). Subsequently, APTES (0.090 mmol) was added. The polycondensation reaction was stopped after 3h by washing the particles three times in the same buffer than that used for the immobilization and stored (20°C, 14 h). The sample was finally stored (4°C) for further analysis.

Scanning electron microscopy and particle size measurement

Particles were imaged using a Zeiss SUPRA[®] 40VP scanning electron microscope. A drop (2 µL) of each sample was spread on freshly cleaved mica substrates, dried (37°C), and sputter-coated with a gold-platinum alloy (15 s, 15 mA). Micrographs were acquired using the InLens mode with an accelerating voltage of 10 kV. Particle size measurement was carried out on micrographs acquired at a magnification of 150 000 X using the [®]AnalySIS software package. One hundred measurements were carried out for each sample.

Cryo-transmission electron microscopy (Cryo-TEM)

A 4 µl aliquot of sample was adsorbed onto holey carbon-coated grid (Lacey), blotted 3 seconds with filter paper and plunge-frozen into liquid ethane (-180°C) using a vitrobot (FEI). Frozen

grids were transferred onto a CM200 FEG microscope (Philips) using a Gatan 626 cryo-holder (Gatan). Electron micrographs were recorded at an accelerating voltage of 200 KV using low-dose system (20 to 30 $e^-/\text{Å}^2$) and keeping the sample at -175°C . Defocus values were $-4\ \mu\text{m}$. Micrographs were recorded on 4K x 4K TemCam-F416 CMOS based camera (TVIPS, Germany).

Ester bond hydrolysis activity assessment

Hydrolytic activity of soluble and immobilized preparations was assayed using a pH indicator assay at 550 nm using 98 structurally diverse esters in 384-well plates as previously described.¹⁴⁴ Briefly, reactions (total volume of 44 μL) were performed in HEPES buffer (5 mM, pH 8.0) containing each ester (10 mg mL^{-1}) and phenol red (0.45 mM) used as pH indicator, and the immobilized preparation (2 μL , corresponding to 0.5 mg of enzyme, per mL of 40 mM HEPES buffer pH 7.0) or soluble enzyme solution (0.5 mg mL^{-1} in 40 mM HEPES buffer pH 7.0) were immediately added to each well using an Repeater M4 pipette (Eppendorf, Germany). The total reaction volume was 44 μL . Note that a fixed concentration of each ester (10 mg mL^{-1}) was used, so that the substrate saturation was ensured for activity tests. After incubation under shaking (30°C , 150 rpm) in a Synergy HT Multi-Mode Microplate Reader, ester hydrolysis was measured spectrophotometrically in continuous mode at 550 nm over 24 h. One unit (U) of enzyme activity was defined as the amount of soluble enzyme or enzyme bound to the carrier required to transform 1 μmol of substrate in 1 min under the assay conditions using the reported extinction coefficient (Phenol red: $\epsilon_{550\ \text{nm}} = 8,450\ \text{M}^{-1}\ \text{cm}^{-1}$). All values were corrected for non-enzymatic transformation using as controls the support without immobilized enzyme. Note that, using those control materials, no appreciable (below detection limit)²² hydrolysis was detected for any of the tested esters. For K_m determination we have used the following conditions: [enzyme]: 5 $\mu\text{g mL}^{-1}$; [ester]: 0-100 mM; reaction volume: 44 μL ; T: 30°C ; pH: 8.0. For k_{cat} determination the following conditions were used: [protein]: 0-5 $\mu\text{g mL}^{-1}$

¹; [ester]: 100 mM; reaction volume: 44 μL ; T: 30°C; pH: 8.0. All K_m and k_{cat} values, were measured in triplicates and corrected for non-enzymatic transformation. Kinetic parameters were calculated by fitting the data fit with Sigma Plot 13.0.

Gas chromatography (GC) analysis for determination of chiral selectivity

Enantioselectivity was evaluated (at 30°C) by using kinetic resolution of methyl (2*R*)-2-phenylpropanoate and methyl (2*S*)-2-phenylpropanoate, as described previously.¹⁴⁴ Briefly, the racemic mixture (2 μL from a stock solution of 200 mg mL⁻¹ in acetonitrile) was added to HEPES buffer (96 μL , 40 mM, pH 7.0). Subsequently, the immobilized preparation (2 μL corresponding to 1 mg mL⁻¹ enzyme in 40 mM HEPES buffer pH 7.0) or soluble enzyme solution (1 mg mL⁻¹) were added. Reactions with racemic mixtures were stopped at different time points by adding 1 800 μL HPLC-grade methanol and the reaction products analyzed by GC. Prior to the analysis the samples (100 μL) were vigorously mixed (3 minutes) with the internal standard (20 μL), H₂O (100 μL) and NaCl (3g/L) and subsequently extracted twice by the addition of ethyl acetate (100 μL) by vigorously mixing (5 min), followed by centrifugation (16 000 x g, 3 min, 4°C). GC system (Agilent Technologies 7890A) consisted in an auto sampler (Agilent Technologies 7693) and an inert MSD with Quadrupole (Agilent Technologies 5975). A volume of the sample (1 μL) was injected through a GC-Column CP-Chirasil-Dex CB (25 m length, 0.25 μm internal diameter, 0.25 μm film) (Agilent J&W GC Columns). The flow rate of the helium carrier gas (1 mL min⁻¹), the split ratio (1:25) and the temperature gradient (80°C min⁻¹, 10°C min⁻¹ to 150°C, 8 minutes total analysis time) were optimized for the separation of the chiral mixture. After each injection, the column was cleaned up (2 minutes at 200°C, 1.5 mL min⁻¹ flow rate). The elution order was previously validated with a standards mixture. The semi-quantification of each analyte was performed using MassHunter Qualitative Analysis software (B.08.00, Agilent), reporting the area for the

individual peaks in arbitrary units. In order to monitor the extraction procedure and the analytical variability, an internal standard, ethyl (*S*)-lactate (200 mg L⁻¹), was added.

Stability tests and HPLC conditions

Stability was assayed in Eppendorf (2 mL) with constant mixing in a shaker with controlled temperature. Before an assay, stock solutions of HEPES (40 mM, pH 7.0) with solvent (10, 20, 30, 45 and 60% (v/v) were prepared) were prepared. These stock solutions were prepared extemporaneously. The immobilized preparation (2 μL, 1 mg mL⁻¹ enzyme) or soluble enzyme solution in HEPES buffer (40 mM, pH 7.0) were added to the desired HEPES: solvent solutions (196 μL, pH 7.0, 40 mM). Suspensions were kept at 30°C for 2 hours, after which α-naphthyl acetate (2 μL from a stock solution 200 mg mL⁻¹ in acetonitrile) was added. After 1 h, reactions were stopped by adding HPLC-grade methanol (1,800 μL). The progress of the reactions was followed by HPLC, as described elsewhere.¹⁴⁴ Prior to the analysis, samples were filtered through a 0.45 μm filter and the presence of the substrate 1-naphthylacetate and the reaction product 1-naphthol were quantified by HPLC analysis, performed using a quaternary pump (model 600, Waters) coupled to an autosampler (Varian ProStar, model 420). The injection volume was 10 μL. The temperature of the column was kept constant (40°C). The detection of peaks was carried out using a photodiode array detector (ProStar, Varian) and integration was carried out using the Varian Star LC workstation 6.41. The column was a Zorbax Eclipse Plus C-18 (4.6 x 100 mm, 3.5 μm, Agilent Technologies) and the mobile phase was acetonitrile/H₂O (65:35 (v/v)) degassed with helium in gradient during 4 minutes in isocratic mode. Both solvents contained formic acid (0.1% (v/v)) degassed with helium. The flow rate was 0.8 mL min⁻¹. The peak area corresponding to 1-naphthylacetate and 1-naphthol was extracted from chromatograms and the conversion and the relative activity compared to a control reaction in the absence of solvents was quantified. Note that calibration curves for both 1-naphthylacetate

and 1-naphthol (concentration ranging from 0 to 0.4 mg mL⁻¹) were performed and used to extract exact concentrations in reaction mixtures.

Crystallization and X-ray structure determination of EH₃ and EH₃ complexed with a derivative of butyl 4-nitrophenyl hexylphosphonate

Initial crystallization conditions were explored by high-throughput techniques with a NanoDrop robot (Innovadyne Technologies), using 22 mg mL⁻¹ protein concentrations in HEPES (40 mM, pH 7, NaCl 50 mM), and commercial screens: JBScreen JCSG++ (Jena Bioscience), SaltRx (Hampton Research), Index (Hampton Research), PACT++ (Jena Bioscience), JBScreen Classic (Jena Bioscience) and Crystal Screen (Hampton Research). Further optimizations were carried out and thin plate-shaped crystals of EH₃ were grown by microseeding technique using the protein (1 μL, 20.80 mg mL⁻¹) in HEPES (40 mM, pH 7, NaCl 100 mM), seeds (0.2 μL, 1:1,000) and the precipitant solution (0.5 μL, 24% PEG PEG3000, 0.1 M BIS-TRIS pH 6.5, 0.2M MgCl₂). The complex with the suicide inhibitor butyl 4-nitrophenylhexyl phosphonate (B-4NHP), was obtained by soaking crystals of EH₃ in mother liquor supplemented with inhibitor (20 mM) for 1 hour.

For data collection, crystals were transferred to cryoprotectant solutions consisting of mother liquor and glycerol (18-22% (v/v)), before being cooled in liquid nitrogen. Diffraction data were collected using synchrotron radiation on the XALOC beamline at ALBA (Cerdanyola del Vallés, Spain). Diffraction images were processed with XDS²⁰⁶ and merged using AIMLESS from the CCP4 package.²⁰⁷ Both crystals were indexed in the C2 space group, with two molecules in the asymmetric unit and 40% solvent content within the unit cell. The data-collection statistics are given in **Table 4**. The structure of EH₃ was solved by Molecular Replacement with MOLREP²⁰⁸ using the coordinates from the homologue Est22 as template (PDB code 5HC0). The structure of the complex was solved by difference Fourier synthesis using the coordinates of the EH₃ native crystals. Crystallographic refinement was performed

using the program REFMAC²⁰⁹ within the CCP4 suite with local non-crystallographic symmetry (NCS). Free R-factor was calculated using a subset of 5% randomly selected structure-factor amplitudes that were excluded from automated refinement. Subsequently, ligands were manually built into the electron density maps with Coot8 and water molecules were included in the model, which, combined with more rounds of restrained refinement, reached the R factors listed in **Table 4**. For butyl 4-nitrophenylhexyl phosphonate, not present in the Protein Data Bank, a model was built using MacPyMOLX11Hybrid (The PyMOL Molecular Graphics System, Version 2.0 Schrödinger, LLC). The model was used to automatically generate coordinates and molecular topologies with eLBOW²¹⁰ suitable for REFMAC refinement. The figures were generated with PyMOL. The crystallographic statistics of EH₃ are listed in **Table 4**.

To extract dynamical details from the X-ray data, the coordinates of native EH₃ were first re-refined using PHENIX²¹¹, and then were used as input models for a time-averaged molecular dynamics refinement as implemented in the Phenix.ensemble-refinement routine, which was performed as described previously.²¹²

Accession codes

The atomic coordinates and structure factors for the EH₃ and EH₃-B-4NHP structures have been deposited in the RCSB Protein Data Bank with accession codes 6SXP and 6SYL.

Supporting figures

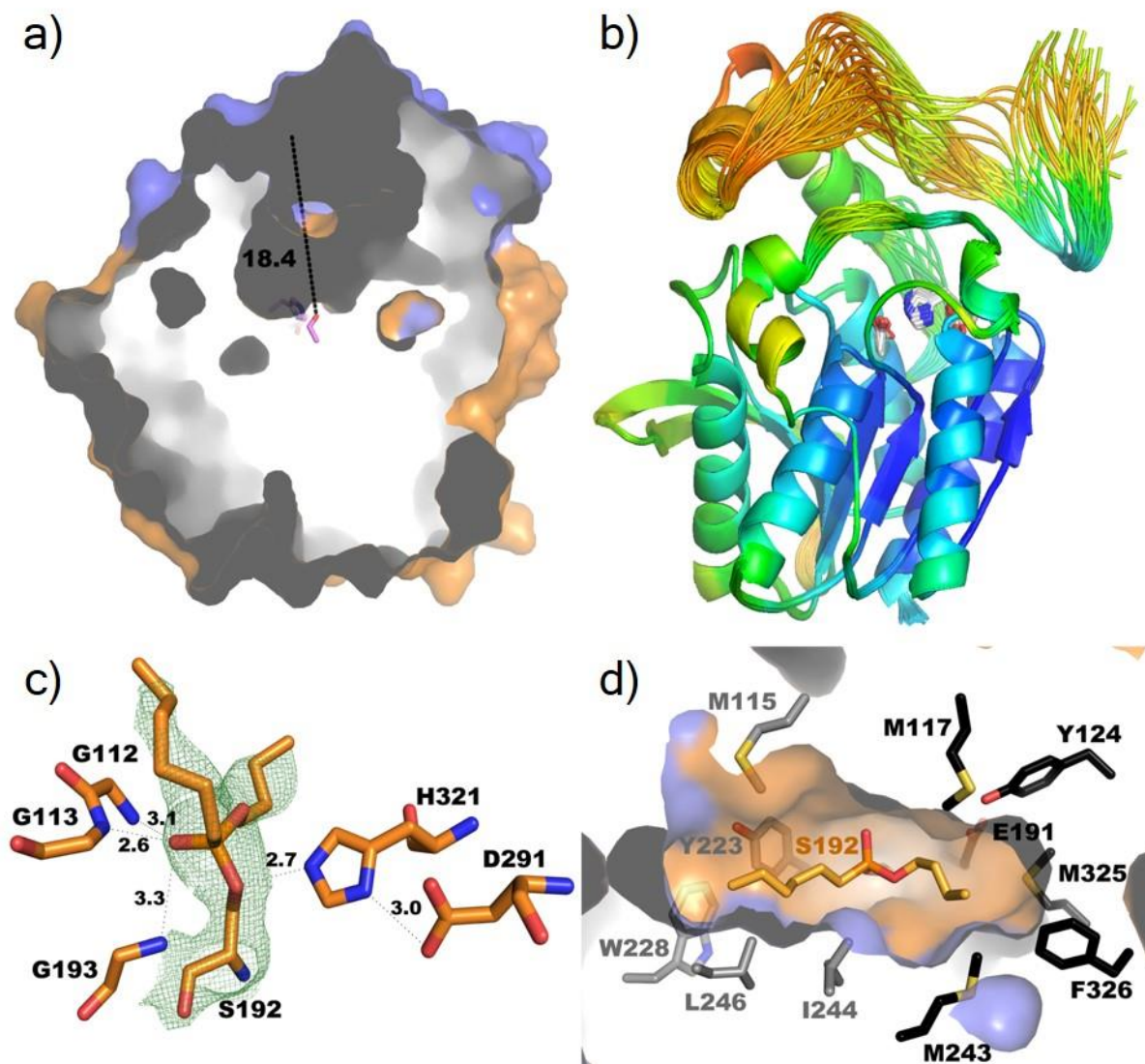


Figure 47. Active site of EH₃. (a) Molecular surface of the EH₃ monomer, in the same orientation to that in Figure 1, showing a tunnel 18 Å deep giving access to the catalytic triad formed by Ser192, Asp291 and His321, through the cap domain (EH₃ is coloured with the same code than in Figure 1). (b) Ensemble refinement performed with the EH₃ coordinates showing potential conformations of the N-terminal region comprising α 1 and α 2 (colour code gives chain mobility, from low in blue to high in red). The catalytic triad is shown as sticks. (c) A close view of the EH₃-butyl-hexyl phosphonate complex mimicking the tetrahedral intermediate of the hydrolytic reaction. The 2Fo-Fc electronic density map at the inhibitor contoured at 0.9 σ cut-off is shown in green. The catalytic Asp291 stabilizes His321, the proton donor/acceptor, which deprotonates the hydroxyl of serine (situated at the “nucleophilic elbow” between β 5 and α 6) enabling its role as nucleophile. Then, it attacks the ester carbonyl resulting in a tetrahedral intermediate, where the oxygen is hydrogen bonded to glycine at the oxoanion hole (Gly112, Gly113 and Gly193). Hydrogen bonds network is shown as dashed lines. (d) A cross-section of the molecular surface of EH₃ showing the catalytic pocket occupied by the phosphonate inhibitor, and the residues bordering the alcohol (black) and acyl (grey) binding sites.

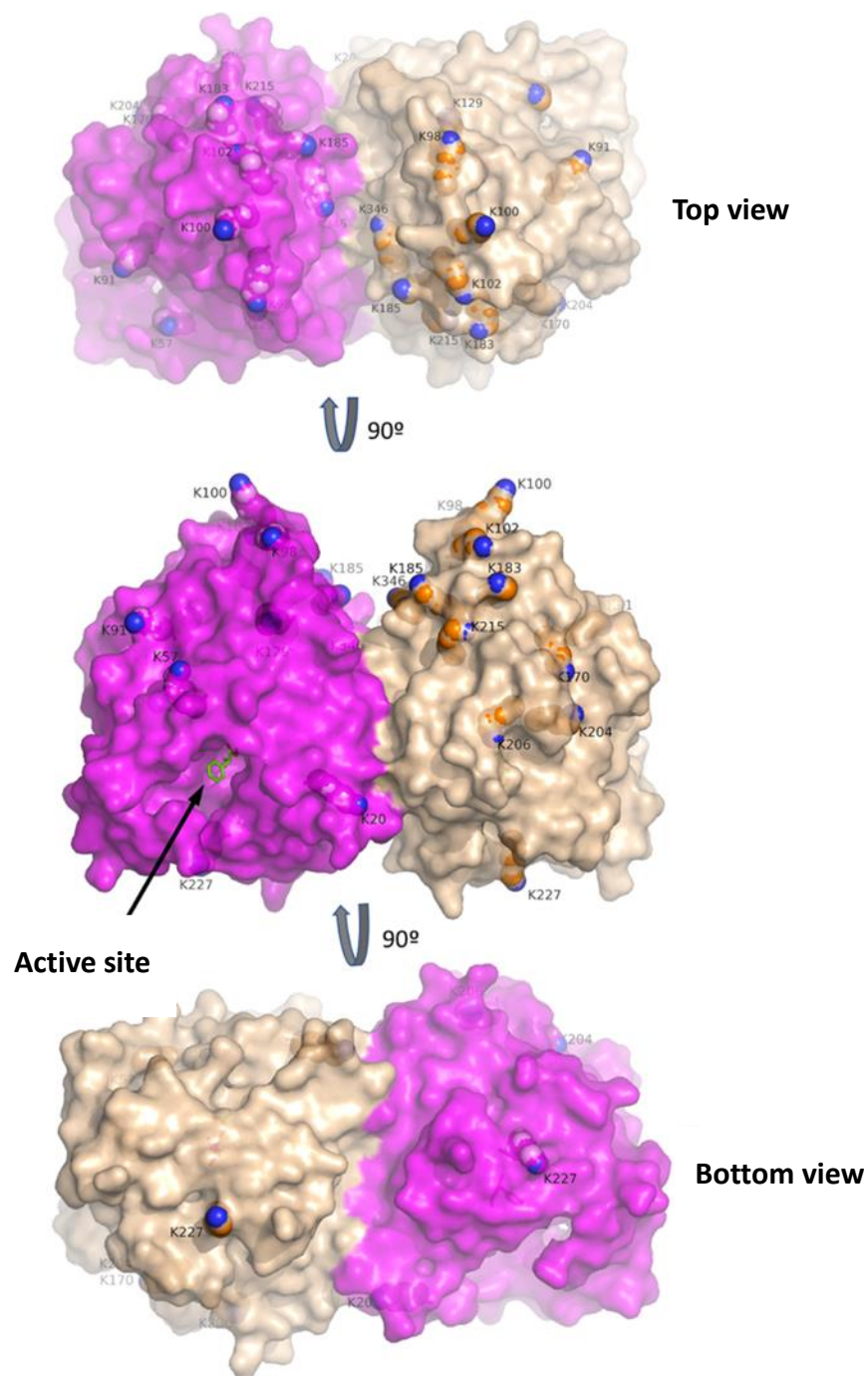


Figure 48. Lys residues on the surface of EH₃. Molecular surface of the two molecules (pink and beige) of the EH₃ dimer showing the position of the Lys residues represented as spheres, with the amine nitrogen atom colored in blue. The phosphonate inhibitor is shown as green sticks in the active site of one of the monomers, while the other active site is hidden at the opposite face of the dimer. Two 90° opposite sense rotations display the top/bottom views of the central picture. Most of the Lys residues are on the “top hemisphere”, which is the putative region involved in immobilization of EH₃ to the support.

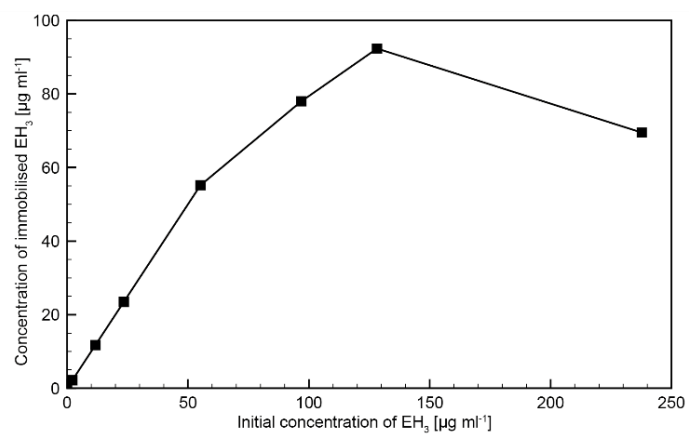


Figure 49. Enzyme immobilization optimization. Different concentration of EH₃ have been tested (x axis). After immobilization, the supernatant was recovered and the concentration (in $\mu\text{g mL}^{-1}$) of unbound enzyme was measured by means of BCA assay.

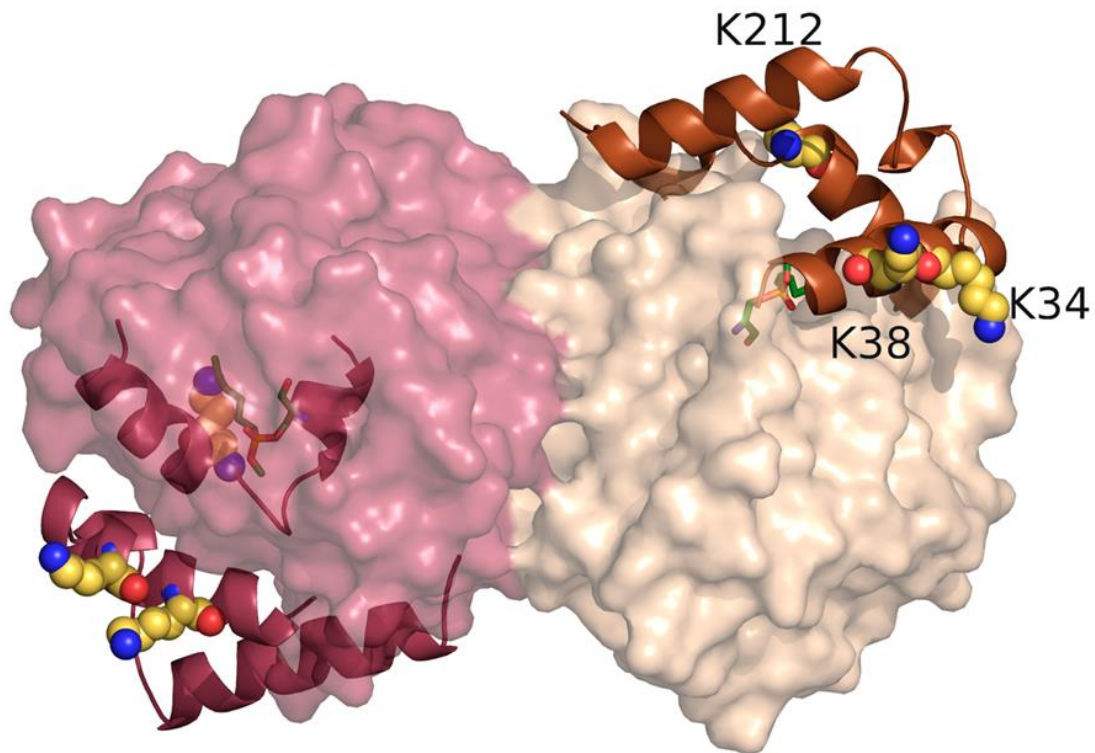


Figure 50. Lys residues at the surface of EH_{1A1} (PDB code 6RB0). Molecular envelope of the two monomers (raspberry and beige) within the dimer, showing their flexible cap domains as cartoon. The superficial Lys residues are represented as yellow spheres, with their amine nitrogen atom colored in blue. A phosphonate inhibitor is shown as green sticks to highlight the active site within each monomer.

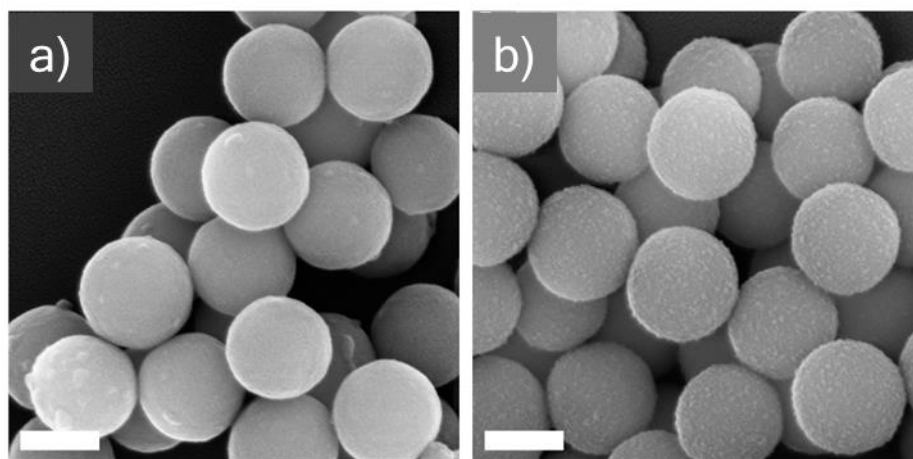


Figure 51. EH_{1A1} and EH₇ scanning electron microscopy (SEM) characterization. Micrographs of (a) EH_{1A1}-TBu/A_[4/1] and (b) EH₇-TBu/A_[4/1]. Scale bars represent 200 nm.

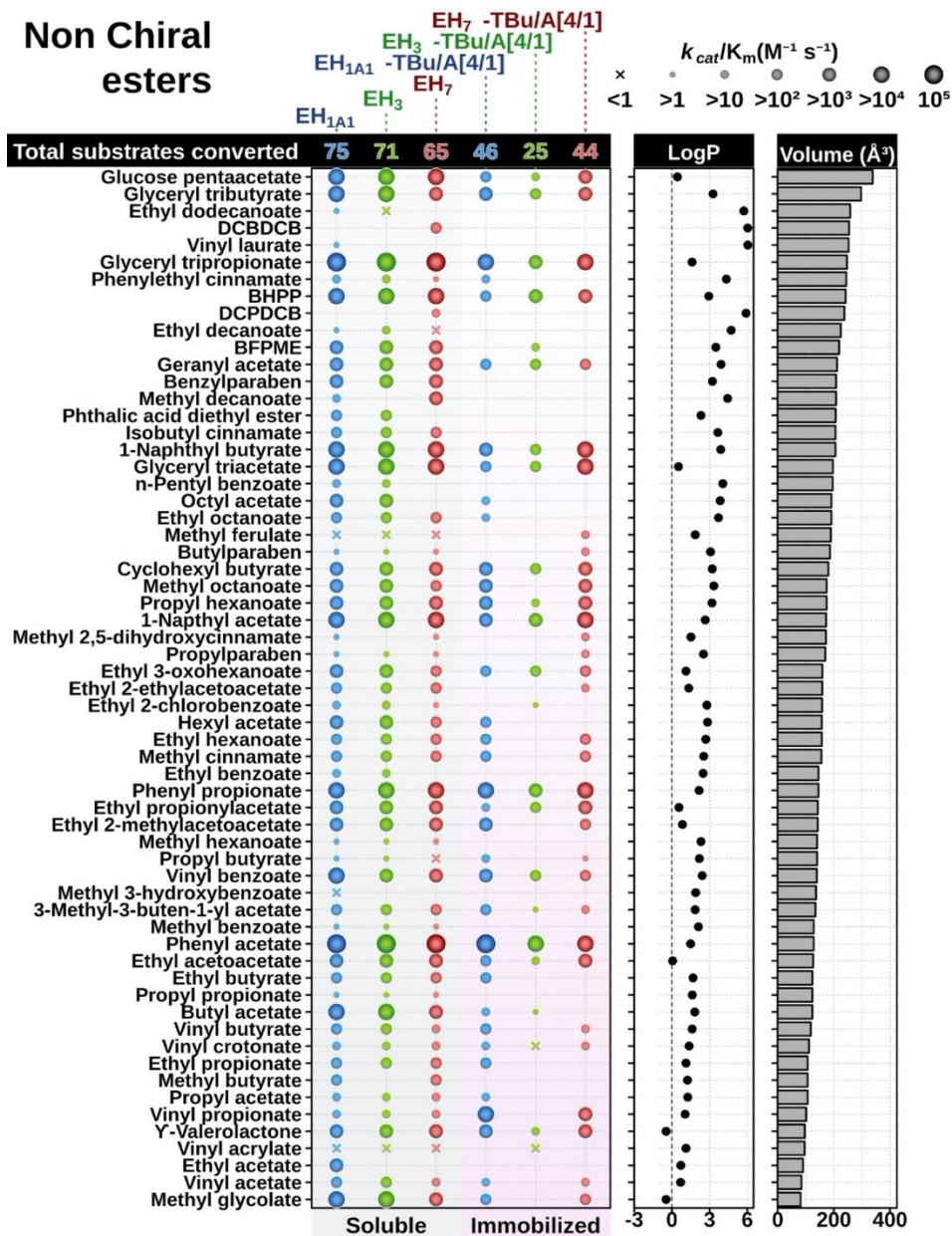


Figure 52. EH_{1A1} and EH_7 Selectivity study. k_{cat}/K_m study of EH_{1A1} , EH_{1A1} -TBu/A_[4/1], EH_3 and EH_3 -TBu/A_[4/1], EH_7 and EH_7 -TBu/A_[4/1] sub-enzymes measured for a set of esters found to be hydrolysed by any of the preparations (shown at the left side of a panel). Hydrophobicity ($\log P$) and volume (\AA^3) of each of the esters are specifically indicated in the columns on the right. For activity determination, calculated on a continuous pH indicator assay.¹⁴⁴ The k_{cat}/K_m values are indicated by the size of the circles, according to the scale shown at right (for raw data, see **Table 9** Annex). Abbreviations as follows: BFPME: benzoic acid, 4-formyl-, phenylmethyl ester; BHPP: benzyl (*R*)-2-hydroxy-3-phenylpropionate. The substrates are ranked based on their volume (\AA^3). The panel was created as described in **Figure 18**.

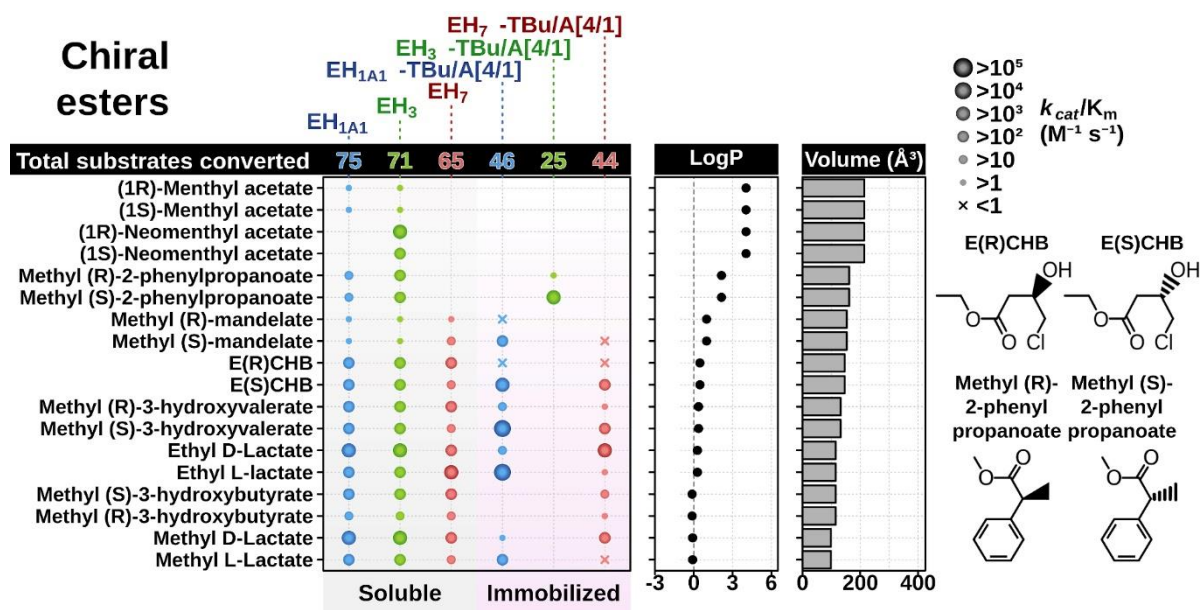


Figure 53. EH_{1A1} and EH₇ Enantioselectivity study. (a) Diagram of the k_{cat}/K_m values of EH_{1A1}, EH_{1A1}-TBu/A_[4/1], EH₃ and EH₃-TBu/A_[4/1], EH₇ and EH₇-TBu/A_[4/1] preparations tested, with nine pairs of chiral substrates shown as a function of their hydrophobicity ($\log P$) and volume (\AA^3). The k_{cat}/K_m values are indicated by the size of the circles, according to the scale shown at right (for raw data, see **Table 9**). The panel was created as described in **Figure 18**.

Supporting Tables

Table 4. Crystallographic statistics of EH₃.

Values in brackets are for the high-resolution shell		
Crystal data	EH ₃	EH ₃ - B-4NHP
Space group	C2	C2
Unit cell parameters		
a (Å)	183.30	183.62
b (Å)	51.62	51.32
c (Å)	70.25	70.40
β (°)	93.86	93.89
Data collection		
Beamline	XALOC(ALBA)	XALOC (ALBA)
Temperature (K)	100	100
Wavelength (Å)	1.072180	0.979240
Resolution (Å)	45.72-2.15 (2.22-2.15)	45.80-2.95 (3.13-2.95)
Data processing		
Total reflections	197240 (17149)	78343 (12899)
Unique reflections	36003 (3087)	13962 (2236)
Multiplicity	5.5 (5.6)	5.6 (5.8)
Completeness (%)	100.0 (99.9)	99.3 (99.9)
Mean I/σ (I)	8.6 (3.4)	6.3 (3.9)
R _{merge} [†] (%)	15.0 (64.8)	24.3 (64.1)
R _{pim} ^{††} (%)	6.8 (29.4)	11.1 (28.9)
Molecules per ASU	2	2
Refinement		
R _{work} / R _{free} ^{†††} (%)	20.2/22.8	25.2/30.5
N° of atoms/average B (Å ²)	5444/26.18	5197/25.42
Macromolecule	5112/25.94	5136/25.47
Ligands	20/44.65	38/29.12
Solvent	312/28.89	23/8.28
Ramachandran plot (%)		
Favoured	94.3	94.7
Outliers	0.9	0.9
RMS deviations		
Bonds (Å)	0.005	0.004
Angles (°)	1.389	1.492
PDB accession codes	6SXP	6SYL

[†]R_{merge} = $\sum_{hkl} \sum_i |I_i(hkl) - [I(hkl)]| / \sum_{hkl} \sum_i I_i(hkl)$, where $I_i(hkl)$ is the i th measurement of reflection hkl and $[I(hkl)]$ is the weighted mean of all measurements.

^{††}R_{pim} = $\sum_{hkl} [1/(N - 1)]^{1/2} \sum_i |I_i(hkl) - [I(hkl)]| / \sum_{hkl} \sum_i I_i(hkl)$, where N is the redundancy for the hkl reflection.

^{†††}R_{work} / R_{free} = $\sum_{hkl} |F_o - F_c| / \sum_{hkl} |F_o|$, where F_c is the calculated and F_o is the observed structure factor amplitude of reflection hkl for the working / free (5%) set, respectively.

Table 5. Silanes used for the production of protective shields.

	A (mmol)	T (mmol)	Bz (mmol)	Ur (mmol)	Bu (mmol)	Hm (mmol)
EH ₃ -T/A _[1/1]	0.09	0.09				
EH ₃ -T/A _[4/1]	0.09	0.392				
EH ₃ -T/A _[6/1]	0.09	0.540				
EH ₃ -T/A _[10/1]	0.09	0.900				
EH ₃ -TBz/A _[4/1]	0.09	0.242	0.150			
EH ₃ -TUr/A _[4/1]	0.09	0.242		0.150		
EH ₃ -TBu/A _[4/1]	0.09	0.242			0.150	
EH ₃ -THm/A _[4/1]	0.09	0.242				0.150
EH ₃ -TBzUrBuHm/A _[4/1]	0.09	0.242	0.037	0.037	0.037	0.037

Table 6. List of carboxyl esters substrates found to be converted by EH₃. The table reports the k_{cat} values for a number of non-chiral (a) and chiral (b) esters. The following information are provided: name of ester, $LogP$ value of the ester calculated using the ACD/ChemSketch 2015.2.5 software, molecular volume of the ester calculated as described in <http://www.molinspiration.com/cgi-bin/properties>, and average k_{cat} in s⁻¹. The assays were performed at 30°C and pH 8.0. The data shown in this table, correspond to average values of three technical assays using one immobilized preparation per each enzyme. The standard deviation was less than 1% for all measurements.

Table 6a. k_{cat} for non-chiral esters and EH ₃ preparations.				k_{cat} (s ⁻¹)										
Substrate	Log P	Volume [Å ³]	Mw [g/mol]	EH ₃	EH ₃ -SPs	EH ₃ -T/A [1/1]	EH ₃ -T/A [4/1]	EH ₃ -T/A [6/1]	EH ₃ -T/A [10/1]	EH ₃ -TBz/A [4/1]	EH ₃ -TUr/A [4/1]	EH ₃ -TBu/A [4/1]	EH ₃ -THm/A [4/1]	EH ₃ -TBzUr BuHm/A [4/1]
1-Naphthyl acetate	2.65	172.56	186.21	17.527	10.743	13.509	16.207	20.683	16.460	1.944	31.457	1.730	17.790	0.780
1-Naphthyl butyrate	3.88	206.17	214.26	2.478	1.447	2.242	2.790	4.368	3.023	0.458	10.627	0.549	7.946	1.480
Glyceryl triacetate	0.52	196.65	218.20	24.598	4.831	5.540	7.220	15.433	6.755	0.455	22.916	0.383	6.368	18.062
Glyceryl tripropionate	1.6	247.06	260.28	28.838	18.579	31.011	36.307	51.029	13.047	3.282	44.463	2.668	24.290	44.351
Glyceryl tributyrate	3.27	297.46	302.36	25.068	20.149	12.563	12.155	12.164	10.935	0.986	26.697	1.052	7.928	3.268
Hexyl acetate	2.83	157.73	144.21	1.904	0	0	0.004	0.013	0.007	0	0	0	0	0
Octyl acetate	3.84	191.34	172.26	2.850	0.101	1.157	1.469	2.242	1.258	0	0.326	0	0.075	0
Ethyl propionate	1.12	107.33	102.13	0.382	0	0	0	0.188	0.072	0	0	0	0	0
Ethyl butyrate	1.68	124.13	116.16	0.340	0	0	0.049	0.853	0.593	0	0.412	0	0.119	0
Ethyl hexanoate	2.69	157.73	144.21	0.964	0	0	0.018	0.651	0.376	0	0	0	0	0
Ethyl octanoate	3.70	191.34	172.26	1.512	0.009	0.043	0.114	0.564	0.203	0	1.108	0	0.132	0
Ethyl decanoate	4.71	224.94	200.32	0.151	0.010	0	0	0	0	0	0	0	0	0
Ethyl dodecanoate	5.72	258.55	228.37	0.010	0.003	0	0	0	0	0	0	0	0	0
Ethyl benzoate	2.48	145.37	150.17	2.523	0.009	0	0	0	0	0	0	0	0	0
Benzoic acid, 4-formyl-,	3.49	219.21	240.25	4.387	0.174	0.897	1.588	2.965	1.258	0.074	8.508	0.114	2.499	3.187

phenylmethyl ester [BFPME]														
Propylparaben	2.51	170.19	180.20	1.039	0	0	0.018	0.043	0.004	0	0.206	0	0	0
Butylparaben	3.07	187.00	194.23	1.643	0	0	0.033	0.101	0.087	0	1.237	0	0	0
Phthalic acid diethyl ester	2.31	206.71	222.24	4.065	0.029	0.058	0.074	0.391	0.087	0	2.249	0	0.207	0
Benzyl (<i>R</i>)-2-hydroxy-3-phenylpropionate [BHPP]	2.93	241.87	256.30	10.796	10.761	17.950	18.747	20.857	11.586	0.575	19.982	0.686	8.303	15.022
Benzylparaben	3.22	208.24	228.24	1.147	0	0	0	0.087	0.058	0	0	0	0	0
Methyl benzoate	2.11	128.57	136.15	1.187	0.015	0	0	0	0	0	0	0	0	0
Methyl hexanoate	2.31	140.93	130.18	1.089	0.007	0	0	0	0	0	0	0	0	0
Methyl octanoate	3.33	174.54	158.24	2.020	0.013	0.033	0.042	0.145	0.029	0	0	0	0	0
Propyl propionate	1.62	124.13	116.16	0.128	0.003	0	0	0	0	0	0	0	0	0
Propyl butyrate	2.18	140.93	130.18	0.138	0.013	0	0	0	0	0	0	0	0	0
Propyl hexanoate	3.19	174.54	158.24	2.697	0.265	0.312	0.719	1.446	0	0.117	10.105	0.114	5.899	0
Phenylethyl cinnamate	4.33	244.44	252.31	0.548	0.009	0	0	0	0	0	0	0	0	0
Isobutyl cinnamate	3.65	206.18	204.26	1.376	0.004	0	0	0	0	0	0	0	0	0
Methyl cinnamate	2.53	155.99	162.19	2.694	0.010	0	0	0	0	0	0	0	0	0
Methyl ferulate	1.86	189.55	208.21	0.420	0	0	0	0	0	0	0	0	0	0
Vinyl acetate	0.69	84.89	86.09	0.219	0.010	0	0	0	0	0	0	0	0	0
Vinyl propionate	1.05	101.70	100.12	0.048	0.007	0	0	0	0	0	0	0	0	0
Vinyl butyrate	1.61	118.50	114.14	1.230	0.006	0	0	0	0	0	0	0	0	0
Vinyl benzoate	2.41	139.74	148.16	5.771	1.026	1.157	1.245	1.273	0.333	0.169	11.116	0.103	5.767	1.138
Vinyl crotonate	1.37	112.31	112.13	4.483	1.099	0.216	0.075	0.005	0	0.017	9.030	0.012	4.001	0
Vinyl acrylate	1.12	96.06	98.10	0.033	0.029	0.021	0.009	0	0	0.032	11.800	0.032	3.438	0.585
Geranyl acetate	3.91	212.09	196.29	3.537	0.111	0.130	0.651	2.242	0.825	0.463	19.689	0.346	8.510	12.128
3-Methyl-3-buten-1-yl acetate	1.85	135.06	128.17	8.683	0.012	0.015	0.023	0.174	0.058	0.100	5.770	0.080	4.396	3.056

Ethyl 2-ethylacetoacetate	1.34	159.70	158.19	3.753	0.006	0.012	0.023	0.043	0.043	0	2.445	0	0.620	0
Ethyl 2-methylacetoacetate	0.84	142.90	144.17	4.264	0.012	0.015	0.098	0.116	0.015	0	3.129	0	0.676	1.301
Ethyl 3-oxohexanoate	1.12	159.92	158.19	8.316	2.072	2.228	3.215	9.011	4.007	0.512	27.056	0.486	10.013	14.794
Ethyl acetoacetate	0.06	126.31	130.14	8.769	0.090	0.130	0.976	2.141	0.651	0.106	9.649	0.103	4.246	11.315
Ethyl propionylacetate	0.56	143.11	144.17	8.724	1.226	2.430	8.136	10.038	4.614	0.269	16.820	0.217	7.965	14.924
γ -Valerolactone	-0.46	96.75	100.12	0.916	0.297	0.333	0.900	1.013	0.680	0.083	6.650	0.049	2.029	4.064
Methyl glycolate	-0.46	81.98	90.08	4.815	0.202	0.232	0.924	1.114	0.622	0	1.695	0	0.263	2.601
Ethyl 2-chlorobenzoate	2.78	158.91	184.62	7.743	0.211	0.246	0.575	2.705	0.463	0.037	4.857	0.032	1.371	2.081
Cyclohexyl butyrate	3.21	180.76	170.25	4.943	11.080	5.080	3.466	3.407	2.398	0.317	15.940	0.821	11.704	0.715
n-Pentyl benzoate	4.05	195.78	192.26	1.104	0.009	0.015	0.040	0.275	0.010	0	0.619	0	0	0
Propyl acetate	1.26	107.33	102.13	25.249	0.004	0.006	0.016	0.012	0.007	0	0.782	0	0.075	0.683
Butyl acetate	1.82	124.13	116.16	25.964	0.010	0.029	0.119	0.203	0.159	0.026	1.500	0.012	0.470	1.366
Phenyl acetate	1.49	128.57	136.15	25.702	47.066	50.479	51.362	51.520	47.731	8.005	104.181	4.454	62.951	82.848
Phenyl propionate	2.16	145.37	150.17	25.043	45.340	45.908	49.336	49.843	42.755	8.551	104.931	5.464	63.834	32.678
Glucose pentaacetate	0.44	338.38	390.34	25.838	1.823	1.526	1.439	1.281	0.955	0.074	8.345	0.020	2.254	2.829

Table 6b. k_{cat} for chiral esters and EH_3 preparations.						k_{cat} (s^{-1})								
Substrate	Log P	Volume [\AA^3]	Mw [g/mol]	EH_3	$\text{EH}_3\text{-SPs}$	$\text{EH}_3\text{-T/A}$ [1/1]	$\text{EH}_3\text{-T/A}$ [4/1]	$\text{EH}_3\text{-T/A}$ [6/1]	$\text{EH}_3\text{-T/A}$ [10/1]	$\text{EH}_3\text{-TBz/A}$ [4/1]	$\text{EH}_3\text{-TUr/A}$ [4/1]	$\text{EH}_3\text{-TBu/A}$ [4/1]	$\text{EH}_3\text{-THm/A}$ [4/1]	$\text{EH}_3\text{-TBzUrBuHm/A}$ [4/1]
(1 <i>R</i>)-Menthyl acetate	4.04	213.72	198.30	1.409	0.029	0.347	0.598	0.752	0.260	0	0.098	0	0.041	0
(1 <i>S</i>)-Menthyl acetate	4.04	213.72	198.30	0.964	0.003	0	0	0.072	0.045	0	0	0	0	0
Methyl (<i>R</i>)-mandelate	0.99	153.42	166.17	3.572	0.072	0.072	0.159	0.232	0.159	0	0.587	0	0	0

Methyl (<i>S</i>)-mandelate	0.99	153.42	166.17	2.360	0.058	0.047	0.015	0.001	0.087	0	0.652	0	0	0
Ethyl (<i>R</i>)-4-chloro-3-hydroxybutyrate [E(<i>R</i>)CHB]	0.47	145.95	166.60	3.099	0	0.015	0.081	0.145	0.101	0	2.477	0	0.188	0.683
Ethyl (<i>S</i>)-4-chloro-3-hydroxybutyrate [E(<i>S</i>)CHB]	0.47	145.95	166.60	3.725	0.019	0.020	0.130	0.434	0.159	0	2.640	0	0.676	1.723
Ethyl <i>D</i> -Lactate	0.28	115.37	118.13	5.303	0.043	0.072	0.121	0.911	0.188	0	4.727	0	0.507	2.341
Ethyl <i>L</i> -lactate	0.28	115.37	118.13	5.408	0.058	0.087	0.115	0.984	0.203	0	4.270	0	0.376	1.512
Methyl (<i>S</i>)-3-hydroxybutyrate	-0.13	115.37	118.13	0.106	0.004	0	0	0	0	0	0	0	0	0
Methyl (<i>R</i>)-3-hydroxybutyrate	-0.13	115.37	118.13	0.644	0.012	0	0	0	0	0	0	0	0	0
(<i>1R</i>)-Neomenthyl acetate	4.04	213.72	198.30	2.820	0.345	0.420	0.663	0.738	0.203	0	0.098	0	0.057	0
(<i>1S</i>)-Neomenthyl acetate	4.04	213.72	198.30	0.624	0.167	0	0	0.015	0.009	0	0	0	0	0
Methyl (<i>R</i>)-3-hydroxyvalerate	0.37	132.17	132.16	2.156	0	0	0.023	0.058	0.210	0	0.359	0	0.038	0
Methyl (<i>S</i>)-3-hydroxyvalerate	0.37	132.17	132.16	0.991	0	0	0.006	0.012	0	0	0.163	0	0.019	0
Methyl <i>D</i> -Lactate	-0.09	98.57	104.10	23.861	0.140	0.232	0.485	1.041	0.347	0	2.771	0	0.376	2.439
Methyl <i>L</i> -Lactate	-0.09	98.57	104.10	20.206	0.046	0.058	0.083	0.174	0.145	0	1.695	0	0.132	1.853
Methyl (<i>R</i>)-2-phenylpropanoate	2.14	161.96	164.2	1.859	0.039	0.043	0.058	0.072	0.001	0	2.242	0.022	1.700	0.434
Methyl (<i>S</i>)-2-phenylpropanoate	2.14	161.96	164.2	3.542	0.556	2.376	3.616	10.533	8.081	3.471	13.271	4.502	12.005	11.409

Table 7. k_{cat} ratio for preferred over non-preferred ester for 9 pairs of enantiomers as determined following hydrolysis of separate enantiomers using EH₃ preparations. average values of three technical assays using one immobilized preparation per each enzyme are reported.

Chiral substrate	k_{cat} ratio for preferred over non-preferred esters using EH ₃ preparations										
	EH ₃	EH ₃ -SPs	EH ₃ -T/A [1/1]	EH ₃ -T/A [4/1]	EH ₃ -T/A [6/1]	EH ₃ -T/A [10/1]	EH ₃ -TBz/A [4/1]	EH ₃ -TUr/A [4/1]	EH ₃ -TBu/A [4/1]	EH ₃ -THm/A [4/1]	EH ₃ -TBzUrBuHm/A [4/1]
Menthyl-acetate	1.5	10.0	Only (R) conv.	Only (R) conv.	10.4	5.8	n.d	Only (R) conv.	n.d	Only (R) conv.	n.d
Methyl-mandelate	1.5	1.3	1.5	10.5	200.0	1.8	n.d	1.1	n.d	n.d	n.d
Ethyl-4-chloro-3-hydroxybutyrate	1.2	52.3	1.4	1.6	3.0	1.6	n.d	1.1	n.d	3.6	2.5
Ethyl-lactate	1.0	1.3	1.2	1.0	1.1	1.1	n.d	1.1	n.d	1.4	1.5
Methyl-3-hydroxybutyrate	6.1	2.7	n.d.	n.d	n.d	n.d	n.d	n.d	n.d	n.d	n.d
Neomenthyl acetate	4.5	2.1	Only (R) conv.	Only (R) conv.	51.0	23.3	n.d	Only (R) conv.	n.d	Only (R) conv.	n.d
Methyl-3-hydroxyvalerate	2.2	n.d.	n.d	3.7	5.0	Only (R) conv.	n.d	2.2	n.d	2.0	n.d
Methyl-lactate	1.2	3.0	4.0	5.8	6.0	2.4	n.d	1.6	n.d	2.9	1.3
Methyl-2-phenylpropanoate	1.9	14.4	54.8	62.5	147.1	9312	Only (S) conv.	5.9	201.7	7.1	26.3

Table 8. *e.e%* for methyl (*R/S*)-2-phenylpropanoate as determined by GC following hydrolysis of a racemic mixture using EH₃ and the immobilized preparations. Results correspond to average values of three technical assays using one immobilized preparation per each enzyme.

Enantiomeric excess (%)										
EH ₃	EH ₃ -SPs	EH ₃ -T/A _[1/1]	EH ₃ -T/A _[4/1]	EH ₃ -T/A _[6/1]	EH ₃ -T/A _[10/1]	EH ₃ -TBz/A _[4/1]	EH ₃ -TU _r /A _[4/1]	EH ₃ -TBu/A _[4/1]	EH ₃ -THm/A _[4/1]	EH ₃ -TBzUrBuHm/A _[4/1]
41.70±0.48%	70.80±0.50%	83.50±1.17%	98.40±0.14%	99.80±0.44%	99.90±0.18%	99.99±0.23%	62.00±0.61%	99.90±0.80%	70.50±0.98%	87.80±0.83%

Table 9. List of carboxyl esters substrates found to be converted by EH_{1A1}, EH_{1A1}-Tbu/A_[4/1], EH₇ and EH₇-Tbu/A_[4/1]. Shown are the k_{cat} , K_m and k_{cat}/K_m values for a number of non-chiral (a) and chiral (b) esters. The following information is provided: name of ester, $LogP$ value of the ester calculated using the ACD/ChemSketch 2015.2.5 software, molecular volume of the ester calculated as described in <http://www.molinspiration.com/cgi-bin/properties>, and average k_{cat} , K_m and k_{cat}/K_m values. The assays were performed at 30°C and pH 8.0, the average values are given, and the standard deviation was less than 1% in all cases. For comparison, values for EH₃ and EH₃-Tbu/A_[4/1], are included. Assays consist in three technical (immobilized) replicates of three different enzymes independently prepared. The standard deviation of the linear fit of replicates is shown, as calculated with Sigma Plot 13.0.

Table 9a. k_{cat} , K_m and k_{cat}/K_m for non-chiral esters using EH _{1A1} , EH ₃ and EH ₇ preparations																					
Non-chiral esters	Log P	Volume [Å ³]	Mw [g/mol]	EH _{1A1}			EH _{1A1} -Tbu/A _[4/1]			EH ₃			EH ₃ -Tbu/A _[4/1]			EH ₇			EH ₇ -Tbu/A _[4/1]		
				k_{cat} (s ⁻¹)	K_m (mM)	k_{cat}/K_m (M ⁻¹ s ⁻¹)	k_{cat} (s ⁻¹)	K_m (mM)	k_{cat}/K_m (M ⁻¹ s ⁻¹)	k_{cat} (s ⁻¹)	K_m (mM)	k_{cat}/K_m (M ⁻¹ s ⁻¹)	k_{cat} (s ⁻¹)	K_m (mM)	k_{cat}/K_m (M ⁻¹ s ⁻¹)	k_{cat} (s ⁻¹)	K_m (mM)	k_{cat}/K_m (M ⁻¹ s ⁻¹)	k_{cat} (min ⁻¹)	K_m (mM)	k_{cat}/K_m (M ⁻¹ s ⁻¹)
1-Naphthyl acetate	2.65	172.56	186.21	16.933	0.420	40317.5	4.060	3.720	1091.4	17.527	0.520	33705.1	1.740	0.750	2320.0	13.018	0.450	28929.6	18.870	0.820	23012.2
1-Naphthyl butyrate	3.88	206.17	214.26	3.915	0.310	12629.0	1.385	1.280	1082.0	2.478	0.190	13043.9	0.558	0.620	900.5	6.203	0.550	11278.8	15.917	0.910	17490.8
Glyceryl triacetate	0.52	196.65	218.2	18.600	0.250	74400.0	2.110	5.850	360.7	24.598	0.460	53474.6	0.393	1.000	393.3	12.673	0.250	50693.3	13.962	0.880	15865.5
Glyceryl tripropionate	1.6	247.06	260.28	37.450	0.270	138703.7	17.638	1.250	14110.7	28.838	0.230	125384.1	2.693	0.520	5179.5	28.063	0.250	112253.3	26.753	0.610	43857.9
Glyceryl tributyrate	3.27	297.46	302.36	7.347	0.510	14405.2	5.642	1.290	4373.4	25.068	1.850	13550.5	1.078	2.220	485.7	27.337	3.060	8933.6	28.485	3.320	8579.8
Hexyl acetate	2.83	157.73	144.21	0.568	0.410	1386.2	0.450	0.980	459.2	1.905	1.640	1161.6	0	0	0.0	0.742	1.200	618.1	0	0	0.0
Octyl acetate	3.84	191.34	172.26	2.450	1.050	2333.3	0.303	5.610	54.1	2.850	1.310	2175.6	0	0	0.0	0	0	0.0	0	0	0.0
Ethyl acetate	0.71	90.53	88.11	3.487	0.590	5909.6	0	0	0.0	0	0	0.0	0	0	0.0	0	0	0.0	0	0	0.0
Ethyl propionate	1.12	107.33	102.13	3.465	7.030	492.9	2.110	7.550	279.5	0.382	0.850	449.0	0	0	0.0	1.833	7.090	258.6	0	0	0.0
Ethyl butyrate	1.68	124.13	116.16	1.368	8.860	154.4	2.060	7.040	292.6	0.340	2.370	143.5	0	0	0.0	0.648	5.400	120.1	0	0	0.0
Ethyl hexanoate	2.69	157.73	144.21	3.068	4.700	652.8	1.707	4.110	415.2	0.963	1.780	541.2	0	0	0.0	5.450	11.610	469.4	1.328	11.640	114.1
Ethyl octanoate	3.7	191.34	172.26	1.028	7.120	144.4	0.290	7.710	37.6	1.512	12.510	120.8	0	0	0.0	0.768	7.490	102.6	0	0	0.0
Ethyl decanoate	4.71	224.94	200.32	0.023	7.450	3.1	0	0	0.0	0.152	8.770	17.3	0	0	0.0	0.027	26.100	1.0	0	0	0.0
Ethyl dodecanoate	5.72	258.55	228.37	0.022	9.050	2.4	0	0	0.0	0.010	12.350	0.8	0	0	0.0	0	0	0.0	0	0	0.0

Ethyl benzoate	2.48	145.37	150.17	0.057	5.130	11.0	0	0	0.0	2.523	18.140	139.1	0	0	0.0	0	0	0.0	0	0	0.0
Benzoic acid, 4-formyl-, phenylmethyl ester [BFPME]	3.49	219.21	240.25	5.275	1.190	4432.8	0	0	0.0	4.387	1.070	4099.7	0.122	1.260	96.6	2.528	1.500	1685.6	0	0	0.0
Propylparaben	2.51	170.19	180.2	0.042	12.850	3.2	0	0	0.0	1.039	34.900	29.8	0	0	0.0	0.030	20.940	1.4	0.288	21.120	13.7
Butylparaben	3.07	187	194.23	0.062	15.850	3.9	0	0	0.0	1.643	38.850	42.3	0	0	0.0	0.040	27.110	1.5	0.485	27.540	17.6
Methyl 3-hydroxybenzoate	1.89	136.59	152.15	0.012	12.330	0.9	0	0	0.0	0	0	0.0	0	0	0.0	0	0	0.0	0	0	0.0
Phthalic acid diethyl ester	2.31	206.71	222.24	0.222	1.120	197.9	0	0	0.0	4.065	2.200	1847.7	0	0	0.0	0	0	0.0	0	0	0.0
Benzyl (R)-2-hydroxy-3-phenylpropionate [BHPP]	2.93	241.87	256.3	21.283	0.530	40157.2	5.338	6.440	828.9	10.797	0.280	38559.5	0.712	0.590	1206.2	2.740	0.180	15222.2	6.417	1.320	4861.1
Benzylparaben	3.22	208.24	228.24	1.278	0.490	2608.8	0	0	0.0	1.147	0.470	2439.7	0	0	0.0	4.923	4.100	1200.8	0	0	0.0
Methyl benzoate	2.11	128.57	136.15	0.057	6.670	8.5	0	0	0.0	0.187	22.190	8.4	0	0	0.0	0.118	29.990	3.9	0	0	0.0
Methyl butyrate	1.24	107.33	102.13	0.455	1.670	272.5	0	0	0.0	0	0	0.0	0	0	0.0	2.517	19.720	127.6	0	0	0.0
Methyl hexanoate	2.31	140.93	130.18	0.017	4.920	3.4	0	0	0.0	1.089	28.720	37.9	0	0	0.0	0.045	31.140	1.4	0	0	0.0
Methyl octanoate	3.33	174.54	158.24	1.787	0.930	1921.1	1.807	0.840	2150.8	2.020	1.090	1853.2	0	0	0.0	0.132	0.170	774.5	1.398	0.820	1705.3
Methyl decanoate	4.43	208.14	186.29	0.185	5.200	35.6	0	0	0.0	0	0	0.0	0	0	0.0	7.228	5.170	1398.1	0	0	0.0
Propyl propionate	1.62	124.13	116.16	0.033	8.070	4.1	0	0	0.0	0.112	29.710	3.8	0	0	0.0	0.013	10.520	1.3	0	0	0.0
Propyl butyrate	2.18	140.93	130.18	0.008	5.520	1.5	0.162	2.680	60.3	0.050	36.670	1.4	0	0	0.0	0.010	16.500	0.6	0.160	16.800	9.5
Propyl hexanoate	3.19	174.54	158.24	2.578	0.510	5055.6	2.768	1.730	1600.2	2.697	0.550	4903.0	0.122	1.250	97.3	4.507	2.010	2242.1	3.750	2.400	1562.5
Phenylethyl cinnamate	4.33	244.44	252.31	0.227	17.320	13.1	0.790	22.570	35.0	0.502	38.910	12.9	0	0	0.0	0.127	22.910	5.5	0	0	0.0
Isobutyl cinnamate	3.65	206.18	204.26	0.852	2.520	338.0	0	0	0.0	1.377	4.410	312.2	0	0	0.0	0.933	6.770	137.9	0	0	0.0
Methyl 2,5-dihydroxycinnamate	1.51	172.03	194.18	0.032	4.500	7.0	0	0	0.0	0	0	0.0	0	0	0.0	0.027	10.680	2.5	0.297	11.150	26.6
Methyl cinnamate	2.53	155.99	162.19	1.017	3.240	313.8	1.080	5.800	186.2	2.693	11.070	243.3	0	0	0.0	1.537	13.250	116.0	1.500	13.340	112.4

Methyl ferulate	1.86	189.55	208.21	0.015	35.370	0.4	0	0	0.0	0.420	48.600	8.6	0	0	0.0	0.003	20.770	0.2	1.503	20.970	71.7
Vinyl acetate	0.69	84.89	86.09	0.140	0.890	157.3	0.085	0.990	85.9	0.218	1.460	149.5	0	0	0.0	0.773	10.570	73.2	0.143	10.840	13.2
Vinyl propionate	1.05	101.7	100.12	0.057	0.930	60.9	17.348	1.360	12756.1	0.048	0.820	58.9	0	0	0.0	0.297	11.200	26.5	19.252	11.410	1687.3
Vinyl butyrate	1.61	118.5	114.14	0.185	0.840	220.2	0.212	0.970	218.2	1.230	5.580	220.4	0	0	0.0	0.868	8.800	98.7	0.525	9.310	56.4
Vinyl laurate	6.04	252.91	226.35	0.077	9.570	8.0	0	0	0.0	0	0	0.0	0	0	0.0	0	0	0.0	0	0	0.0
Vinyl benzoate	2.41	139.74	148.16	7.475	0.740	10101.4	13.065	2.310	5655.8	5.770	0.590	9779.7	0.110	1.060	103.8	20.337	4.710	4317.8	4.495	5.500	817.3
Vinyl crotonate	1.37	112.31	112.13	0.310	9.150	33.9	0.212	9.280	22.8	4.483	30.550	146.7	0.028	30.690	0.9	0.302	20.610	14.6	0.270	21.250	12.7
Vinyl acrylate	1.12	96.06	98.1	0.003	9.130	0.4	0	0	0.0	0.012	45.680	0.3	0.038	46.290	0.8	0.003	21.330	0.2	0	0	0.0
Geranyl acetate	3.91	212.09	196.29	0.923	0.590	1565.0	0.593	1.380	430.0	3.537	2.410	1467.5	0.358	2.710	132.2	1.548	1.200	1290.3	0.283	1.430	198.1
3-Methyl-3-buten-1-yl acetate	1.85	135.06	128.17	0.482	0.580	830.5	0.408	0.830	492.0	8.683	11.140	779.5	0.102	11.340	9.0	1.452	4.320	336.0	0.480	5.690	84.4
Ethyl 2-ethylacetoacetate	1.34	159.7	158.19	0.220	0.420	523.8	0	0	0.0	3.753	7.170	523.5	0	0	0.0	2.032	7.860	258.5	0.187	8.480	22.0
Ethyl 2-methylacetoacetate	0.84	142.9	144.17	1.420	0.320	4437.5	1.812	0.710	2551.6	4.263	1.020	4179.7	0	0	0.0	2.610	1.460	1787.7	1.437	1.900	756.1
Ethyl 3-oxohexanoate	1.12	159.92	158.19	5.767	0.730	7899.5	0.567	1.340	422.9	8.317	1.060	7845.9	0.510	1.470	346.9	26.822	51.470	521.1	14.790	51.810	285.5
Ethyl acetoacetate	0.06	126.31	130.14	5.493	0.710	7737.1	1.423	1.500	948.9	8.768	1.530	5730.9	0.112	1.880	59.4	24.033	6.530	3680.4	9.955	7.030	1416.1
Ethyl propionylacetate	0.56	143.11	144.17	8.245	1.030	8004.9	0.223	2.930	76.2	8.723	1.310	6659.0	0.227	1.760	128.8	27.602	7.160	3855.0	7.862	7.380	1065.3
γ-Valerolactone	-0.46	96.75	100.12	5.730	1.020	5617.6	8.463	1.700	4978.4	0.915	0.200	4575.0	0.057	0.900	63.0	2.402	0.960	2501.7	7.607	1.700	4474.5
Methyl glycolate	-0.46	81.98	90.08	7.847	0.600	13077.8	0.650	1.000	650.0	4.815	0.410	11743.9	0	0	0.0	2.773	0.290	9563.2	0.217	0.760	285.1
Ethyl 2-chlorobenzoate	2.78	158.91	184.62	0.252	16.000	15.7	0	0	0.0	7.743	41.030	188.7	0.052	41.570	1.2	0.120	21.650	5.5	0	0	0.0
Cyclohexyl butyrate	3.21	180.76	170.25	6.943	1.210	5738.3	13.538	1.640	8255.1	4.943	0.910	5432.2	0.823	1.570	524.4	16.503	6.770	2437.7	8.362	7.310	1143.9
n-Pentyl benzoate	4.05	195.78	192.26	0.655	35.170	18.6	0	0	0.0	0.642	36.510	17.6	0	0	0.0	0	0	0.0	0	0	0.0
2,4-Dichlorophenyl 2,4-dichlorobenzoate [DCPDCB]	5.89	237.56	336	0	0	0.0	0	0	0.0	0	0	0.0	0	0	0.0	0.468	8.960	52.3	0	0	0.0

2,4-Dichlorobenzyl 2,4- dichlorobenzoate [DCBDCB]	6.03	254.37	350.031	0	0	0.0	0	0	0.0	0	0	0.0	0	0	0.0	0.818	3.040	269.2	0	0	0.0
Propyl acetate	1.26	107.33	102.13	0.228	3.230	70.7	0.282	3.650	77.2	25.249	40.150	628.9	0	0	0.0	0.742	22.910	32.4	0	0	0.0
Butyl acetate	1.82	124.13	116.16	7.762	0.500	15523.3	0.187	3.240	57.6	25.963	1.920	13522.6	0.020	2.250	8.9	2.330	0.330	7060.6	0	0	0.0
Phenyl acetate	1.49	128.57	136.15	21.833	0.080	272916.7	35.423	0.060	590388.9	25.702	0.100	257016.7	4.463	0.360	12398.1	26.532	0.120	221097.2	25.797	0.500	51593.3
Phenyl propionate	2.16	145.37	150.17	46.617	0.970	48058.4	33.023	1.540	21443.7	25.043	0.560	44720.2	5.472	0.650	8417.9	26.245	0.860	30517.4	26.700	1.270	21023.6
Glucose pentaacetate	0.44	338.38	390.34	13.235	0.550	24063.6	0.718	1.000	718.3	25.838	1.160	22274.4	0.030	2.370	12.7	27.980	2.040	13715.7	20.952	2.200	9523.5

Table 9b. k_{cat} , K_m and k_{cat}/K_m for chiral esters using EH_{1A1}, EH₃ and EH₇ preparations

Chiral esters	Log P	Volume [Å ³]	Mw [g/mol]	EH _{1A1}			EH _{1A1} -TBu/A[4/1]			EH ₃			EH ₃ -TBu/A[4/1]			EH ₇			EH ₇ -TBu/A[4/1]		
				k_{cat} (s ⁻¹)	K_m (mM)	k_{cat}/K_m (M ⁻¹ s ⁻¹)	k_{cat} (s ⁻¹)	K_m (mM)	k_{cat}/K_m (M ⁻¹ s ⁻¹)	k_{cat} (s ⁻¹)	K_m (mM)	k_{cat}/K_m (M ⁻¹ s ⁻¹)	k_{cat} (s ⁻¹)	K_m (mM)	k_{cat}/K_m (M ⁻¹ s ⁻¹)	k_{cat} (s ⁻¹)	K_m (mM)	k_{cat}/K_m (M ⁻¹ s ⁻¹)	k_{cat} (s ⁻¹)	K_m (mM)	k_{cat}/K_m (M ⁻¹ s ⁻¹)
(1R)-Menthyl acetate	4.04	213.72	198.3	0.017	6.550	2.6	0	0	0	1.409	22.710	62.0	0	0	0	0	0	0	0	0	0
(1S)-Menthyl acetate	4.04	213.72	198.3	0.010	6.750	1.5	0	0	0	0.964	9.080	106.2	0	0	0	0	0	0	0	0	0
Methyl (R)- mandelate	0.99	153.42	166.17	0.009	5.220	1.6	0	8.660	0	3.572	20.970	170.3	0	0	0	0.217	34.570	6.3	0	0	0
Methyl (S)- mandelate	0.99	153.42	166.17	0.025	6.600	3.8	0.245	2.020	121.1	2.360	9.060	260.5	0	0	0	0.266	23.610	11.3	0.023	24.260	1.0
Ethyl (R)-4- chloro-3- hydroxybutyrate [E(R)CHB]	0.47	145.95	166.6	1.766	4.710	374.9	0.006	16.210	0.4	3.099	8.960	345.9	0	0	0	2.543	20.400	124.6	0.021	21.230	1.0
Ethyl (S)-4- chloro-3- hydroxybutyrate [E(S)CHB]	0.47	145.95	166.6	1.812	7.500	241.6	25.733	7.300	3525.1	3.725	17.070	218.2	0	0	0	1.856	21.320	87.1	4.298	23.380	183.8
Ethyl D-Lactate	0.28	115.37	118.13	2.181	0.690	3160.1	0.030	0.650	45.4	5.303	1.710	3100.9	0	0	0	2.569	10.710	239.9	4.664	2.260	2063.9
Ethyl L-lactate	0.28	115.37	118.13	0.406	0.640	634.9	2.128	0.200	10640.8	5.408	1.000	5408	0	0	0	2.559	1.920	1332.6	0.051	11.130	4.6
Methyl (S)-3- hydroxybutyrate	-0.13	115.37	118.13	0.164	0.710	231.0	0	0	0	0.106	0.490	215.3	0	0	0	2.327	22.130	105.1	0.769	22.890	33.6

Methyl (<i>R</i>)-3-hydroxybutyrate	-0.13	115.37	118.13	0.090	0.930	97.0	0	0	0	0.644	2.250	286.2	0	0	0	0.701	16.700	42.0	0.065	17.050	3.8
(1 <i>R</i>)-Neomenthyl acetate	4.04	213.72	198.3	0	0	0	0	0	0	2.820	1.910	1476.3	0	0	0	0	0	0	0	0	0
(1 <i>S</i>)-Neomenthyl acetate	4.04	213.72	198.3	0	0	0	0	0	0	0.624	2.930	212.9	0	0	0	0	0	0	0	0	0
Methyl (<i>R</i>)-3-hydroxyvalerate	0.37	132.17	132.16	0.151	0.630	239.4	0.023	0.920	25.2	2.156	10.760	200.3	0	0	0	2.425	22.550	107.5	0.107	28.230	3.8
Methyl (<i>S</i>)-3-hydroxyvalerate	0.37	132.17	132.16	0.104	0.460	226.8	3.032	0.140	21658.3	0.991	4.840	204.8	0	0	0	2.703	27.900	96.9	3.421	22.900	149.4
Methyl <i>D</i> -Lactate	-0.09	98.57	104.1	1.045	0.800	1306.7	0.008	1.170	7.1	23.861	20.170	1183.0	0	0	0	2.748	2.750	999.2	1.158	3.370	343.7
Methyl <i>L</i> -Lactate	-0.09	98.57	104.1	0.435	2.250	193.3	1.411	2.100	671.7	20.206	40.150	503.3	0	0	0	1.831	25.050	73.1	0.025	25.140	1.0
Methyl (<i>R</i>)-2-phenylpropanoate	2.14	161.96	164.2	1.083	21.100	51.3	0	0	0	1.859	4.780	388.9	0.028	5.080	5.4	0	0	0.0	0	0	0
Methyl (<i>S</i>)-2-phenylpropanoate	2.14	161.96	164.2	1.050	22.400	46.9	0	0	0	3.542	4.110	861.8	5.287	4.660	1134.5	0	0	0.0	0	0	0

Table 10. Kinetic parameters, E_{app} and $e.e.$ % for EH₃ and EH₃-TBu/A_[4/1] against methyl-(*R*)-2-phenylpropanoate and methyl-(*S*)-2-phenylpropanoate. Assays consist in three technical (immobilized) replicates of three different enzymes independently prepared. The standard deviation of the linear fit of replicates is shown, as calculated with Sigma Plot 13.0.

Ester	EH ₃					EH ₃ -TBu/A _[4/1]				
	k_{cat} (s ⁻¹)	K_m (mM)	k_{cat}/K_m (M ⁻¹ s ⁻¹)	E_{app} ¹	$e.e.$ % ²	k_{cat} (s ⁻¹)	K_m (mM)	k_{cat}/K_m (M ⁻¹ s ⁻¹)	E_{app} ¹	$e.e.$ % ²
Methyl-(<i>R</i>)-2-phenylpropanoate	1.859±0.163	4.78±0.18	388.9	2.21	41.70±0.48	0.028±0.00	5.08±0.3	5.51	213	99.9±1.8
Methyl-(<i>S</i>)-2-phenylpropanoate	3.542±0.062	4.11±0.32	861.6			5.287±0.20	4.66±0.7	1134.5		

¹Calculated by following the hydrolysis of separate enantiomers.

²Calculated by HPLC using a racemic mixture as previously reported.¹⁴⁴

Table 11. Kinetic parameters, E_{app} and $e.e.$ % for for EH_{1A1}, EH_{1A1}-TBu/A_[4/1], EH₇ and EH₇-TBu/A_[4/1] against ethyl (*R*)-4-chloro-3-hydroxybutyrate and ethyl (*S*)-4-chloro-3-hydroxybutyrate. The assays, in triplicates, were performed as for EH3. The standard deviation of the linear fit of triplicates is shown, as calculated with Sigma Plot 13.0.

Ester	EH _{1A1}					EH _{1A1} -TBu/A _[4/1]				
	k_{cat} (s ⁻¹)	K_m (mM)	k_{cat}/K_m (M ⁻¹ s ⁻¹)	E_{app} ¹	$e.e.$ % ²	k_{cat} (s ⁻¹)	K_m (mM)	k_{cat}/K_m (M ⁻¹ s ⁻¹)	E_{app} ¹	$e.e.$ % ²
Ethyl (<i>R</i>)-4-chloro-3-hydroxybutyrate	1.765±0.030	4.71±0.06	374.7	1.6	50±1.2	0.006±0.01	16.21±0.08	0.37	ca. 14700	99.7±0.3 (S)
Ethyl (<i>S</i>)-4-chloro-3-hydroxybutyrate	1.812±0.037	7.50±0.08	241.6			37.73±0.08	7.30±0.34	5168.5		

¹Calculated by following the hydrolysis of separate enantiomers (see data in **Table 9**).

²Calculated by HPLC using a racemic mixture as previously reported.¹⁴⁴

Ester	EH ₇					EH ₇ -TBu/A _[4/1]				
	k_{cat} (s ⁻¹)	K_m (mM)	k_{cat}/K_m (M ⁻¹ s ⁻¹)	E_{app} ¹	$e.e.$ % ²	k_{cat} (s ⁻¹)	K_m (mM)	k_{cat}/K_m (M ⁻¹ s ⁻¹)	E_{app} ¹	$e.e.$ % ²
Ethyl (<i>R</i>)-4-chloro-3-hydroxybutyrate	2.543±0.062	20.4±0.49	124.7	1.4	52.2±2.3	0.021±0.003	21.23±0.15	0.99	186	98.5±1.2 (S)
Ethyl (<i>S</i>)-4-chloro-3-hydroxybutyrate	1.857±0.037	21.32±0.2	87.1			4.298±0.053	23.38±0.13	183.8		

¹Calculated by following the hydrolysis of separate enantiomers (see data in **Table 9**).

²Calculated by HPLC using a racemic mixture as previously reported.¹⁴⁴

REFERENCES

1. Chapman, J.; Ismail, A. E.; Dinu, C. Z., Industrial Applications of Enzymes: Recent Advances, Techniques, and Outlooks. *Catalysts* **2018**, *8*, 238.
2. Zdarta, J.; Meyer, A. S.; Jesionowski, T.; Pinelo, M., A General Overview of Support Materials for Enzyme Immobilization: Characteristics, Properties, Practical Utility. *Catalysts* **2018**, *8*, 92.
3. Sheldon, R. A.; van Pelt, S., Enzyme Immobilisation in Biocatalysis: Why, What and How. *Chem. Soc. Rev.* **2013**, *42*, 6223-6235.
4. Packer, M. S.; Liu, D. R., Methods for the Directed Evolution of Proteins. *Nat. Rev. Genet.* **2015**, *16*, 379-394.
5. Spicer, C. D.; Davis, B. G., Selective Chemical Protein Modification. *Nat Commun* **2014**, *5*, 4740.
6. Arnold, F. H., Innovation by Evolution: Bringing New Chemistry to Life (Nobel Lecture). *Angew. Chem. Int. Ed.* **2019**, *58*, 14420-14426.
7. Porebski, B. T.; Buckle, A. M., Consensus Protein Design. *Prot. Eng. Des. Sel.* **2016**, *29*, 245-251.
8. Li, C.; Zhang, R.; Wang, J.; Wilson, L. M.; Yan, Y., Protein Engineering for Improving and Diversifying Natural Product Biosynthesis. *Trends Biotechnol.* **2020**, *38*, 729-744.
9. Berman, H. M.; Vallat, B.; Lawson, C. L., The Data Universe of Structural Biology. *IUCrJ* **2020**, *7*, 630-638.
10. Tranter, G. E., Protein Structure Analysis by Cd, Ftir, and Raman Spectroscopies. In *Encyclopedia of Spectroscopy and Spectrometry (Third Edition)*, Lindon, J. C.; Tranter, G. E.; Koppenaal, D. W., Eds. Academic Press: Oxford, 2017; pp 740-758.
11. Di Trani, J. M.; De Cesco, S.; O'Leary, R.; Plescia, J.; do Nascimento, C. J.; Moitessier, N., *et al.*, Rapid Measurement of Inhibitor Binding Kinetics by Isothermal Titration Calorimetry. *Nat. Commun.* **2018**, *9*, 893.
12. Opella, S. J., Solid-State Nmr and Membrane Proteins. *J. Magn. Reson.* **2015**, *253*, 129-137.
13. Mueller, L. J.; Dunn, M. F., Nmr Crystallography of Enzyme Active Sites: Probing Chemically Detailed, Three-Dimensional Structure in Tryptophan Synthase. *Acc. Chem. Res.* **2013**, *46*, 2008-2017.
14. Kan, S. B. J.; Lewis, R. D.; Chen, K.; Arnold, F. H., Directed Evolution of Cytochrome C for Carbon-Silicon Bond Formation: Bringing Silicon to Life. *Science* **2016**, *354*, 1048-1051.
15. Boutureira, O.; Bernardes, G. J. L., Advances in Chemical Protein Modification. *Chem. Rev.* **2015**, *115*, 2174-2195.
16. Hermanson, G. T., Chapter 1 - Introduction to Bioconjugation. In *Bioconjugate Techniques (Third Edition)*, Hermanson, G. T., Ed. Academic Press: Boston, 2013; pp 1-125.
17. Köhler, V.; Wilson, Y. M.; Dürrenberger, M.; Ghislieri, D.; Churakova, E.; Quinto, T., *et al.*, Synthetic Cascades Are Enabled by Combining Biocatalysts with Artificial Metalloenzymes. *Nature Chem.* **2013**, *5*, 93-99.
18. Jeschek, M.; Panke, S.; Ward, T. R., Artificial Metalloenzymes on the Verge of New-to-Nature Metabolism. *Trends Biotechnol.* **2018**, *36*, 60-72.

19. Schwizer, F.; Okamoto, Y.; Heinisch, T.; Gu, Y.; Pellizzoni, M. M.; Lebrun, V., *et al.*, Artificial Metalloenzymes: Reaction Scope and Optimization Strategies. *Chem. Rev.* **2018**, *118*, 142-231.
20. Renata, H.; Wang, Z. J.; Arnold, F. H., Expanding the Enzyme Universe: Accessing Non-Natural Reactions by Mechanism-Guided Directed Evolution. *Angew. Chem. Int. Ed.* **2015**, *54*, 3351-67.
21. Wingard, L. B.; Pye, E. K., Enzyme Engineering. *Science* **1974**, *184*, 189-191.
22. Nelson, J. M.; Griffin, E. G., Adsorption of Invertase. *J. Am. Chem. Soc.* **1916**, *38*, 1109-1115.
23. Reis, C.; Sousa, E.; Serpa, J.; Oliveira, R.; Oliveira, R.; Santos, J., Design of Immobilized Enzyme Biocatalysts: Drawbacks and Opportunities. *Quim. Nova* **2019**, *42*, 768-783.
24. Vranish, J. N.; Ancona, M. G.; Walper, S. A.; Medintz, I. L., Pursuing the Promise of Enzymatic Enhancement with Nanoparticle Assemblies. *Langmuir* **2018**, *34*, 2901-2925.
25. Hettiarachchy, N. S.; Feliz, D. J.; Edwards, J.; Horax, R., The Use of Immobilized Enzymes to Improve Functionality. In *Protein in Food Processing* (Second edition) 2018; pp 569-597.
26. Kunamneni, A.; Ghazi, I.; Camarero, S.; Ballesteros, A.; Plou, F. J.; Alcalde, M., Decolorization of Synthetic Dyes by Laccase Immobilized on Epoxy-Activated Carriers. *Process Biochem.* **2008**, *43*, 169-178.
27. Britton, J.; Majumdar, S.; Weiss, G. A., Continuous Flow Biocatalysis. *Chem. Soc. Rev.* **2018**, *47*, 5891-5918.
28. Böhmer, W.; Volkov, A.; Engelmark Cassimjee, K.; Mutti, F. G., Continuous Flow Bioamination of Ketones in Organic Solvents at Controlled Water Activity Using Immobilized Ω -Transaminases. *Adv. Synth. Catal.* **2020**, *362*, 1858-1867.
29. Saranya, P.; Ramani, K.; Sekaran, G., Biocatalytic Approach on the Treatment of Edible Oil Refinery Wastewater. *RSC. Adv.* **2014**, *4*, 10680-10692.
30. Hanefeld, U.; Gardossi, L.; Magner, E., Understanding Enzyme Immobilisation. *Chem. Soc. Rev.* **2009**, *38*, 453-468.
31. Fernandez-Lafuente, R.; Armisen, P.; Sabuquillo, P.; Fernández-Lorente, G.; M. Guisán, J., Immobilization of Lipases by Selective Adsorption on Hydrophobic Supports. *Chem. Phys. Lipids* **1998**, *93*, 185-197.
32. Mateo, C.; Palomo, J. M.; Fernandez-Lorente, G.; Guisan, J. M.; Fernandez-Lafuente, R., Improvement of Enzyme Activity, Stability and Selectivity Via Immobilization Techniques. *Enzyme Microb. Technol.* **2007**, *40*, 1451-1463.
33. Fernandez-Lorente, G.; Rocha-Martín, J.; Guisan, J. M., Immobilization of Lipases by Adsorption on Hydrophobic Supports: Modulation of Enzyme Properties in Biotransformations in Anhydrous Media. In *Immobilization of Enzymes and Cells: Methods and Protocols*, Guisan, J. M.; Bolivar, J. M.; López-Gallego, F.; Rocha-Martín, J., Eds. Springer US: New York, NY, 2020; pp 143-158.
34. Rodrigues, R. C.; Virgen-Ortíz, J. J.; dos Santos, J. C. S.; Berenguer-Murcia, Á.; Alcantara, A. R.; Barbosa, O., *et al.*, Immobilization of Lipases on Hydrophobic Supports: Immobilization Mechanism, Advantages, Problems, and Solutions. *Biotechnol. Adv.* **2019**, *37*, 746-770.
35. Khan, F. I.; Lan, D.; Durrani, R.; Huan, W.; Zhao, Z.; Wang, Y., The Lid Domain in Lipases: Structural and Functional Determinant of Enzymatic Properties. *Front. Bioeng. Biotechnol.* **2017**, *5*.
36. Stauch, B.; Fisher, S. J.; Cianci, M., Open and Closed States of Candida Antarctica Lipase B: Protonation and the Mechanism of Interfacial Activation. *J. Lipid Res.* **2015**, *56*, 2348-2358.

37. Fernández-Lorente, G.; Cabrera, Z.; Godoy, C.; Fernandez-Lafuente, R.; Palomo, J. M.; Guisan, J., Interfacially Activated Lipases against Hydrophobic Supports: Effect of the Support Nature on the Biocatalytic Properties. *Process Biochem.* **2008**, *43*, 1061-1067.
38. Tacias-Pascacio, V. G.; Peirce, S.; Torrestiana-Sanchez, B.; Yates, M.; Rosales-Quintero, A.; Virgen-Ortíz, J. J., *et al.*, Evaluation of Different Commercial Hydrophobic Supports for the Immobilization of Lipases: Tuning Their Stability, Activity and Specificity. *RSC. Adv.* **2016**, *6*, 100281-100294.
39. Bastida, A.; Sabuquillo, P.; Armisen, P.; Fernández-Lafuente, R.; Huguet, J.; Guisán, J. M., A Single Step Purification, Immobilization, and Hyperactivation of Lipases Via Interfacial Adsorption on Strongly Hydrophobic Supports. *Biotechnol. Bioeng.* **1998**, *58*, 486-493.
40. Jonkheijm, P.; Weinrich, D.; Schröder, H.; Niemeyer, C. M.; Waldmann, H., Chemical Strategies for Generating Protein Biochips. *Angew. Chem. Int. Ed.* **2008**, *47*, 9618-9647.
41. Hermanson, G. T., Chapter 2 - Functional Targets for Bioconjugation. In *Bioconjugate Techniques (Third Edition)*, Hermanson, G. T., Ed. Academic Press: Boston, 2013; pp 127-228.
42. Vantourout, J. C.; Adusumalli, S. R.; Knouse, K. W.; Flood, D. T.; Ramirez, A.; Padial, N. M., *et al.*, Serine-Selective Bioconjugation. *J. Am. Chem. Soc.* **2020**, *142*, 17236–17242.
43. Novick, S. J.; Rozzell, J. D., Immobilization of Enzymes by Covalent Attachment. In *Microbial Enzymes and Biotransformations*, Barredo, J. L., Ed. Humana Press: Totowa, NJ, 2005; pp 247-271.
44. Hermanson, G. T., Chapter 5 - Homobifunctional Crosslinkers. In *Bioconjugate Techniques (Third Edition)*, Hermanson, G. T., Ed. Academic Press: Boston, 2013; pp 275-298.
45. Marochkin, I. I.; Dorofeeva, O. V., Amide Bond Dissociation Enthalpies: Effect of Substitution on Nc Bond Strength. *Comput. Theor. Chem.* **2012**, *991*, 182-191.
46. Homaei, A. A.; Sariri, R.; Vianello, F.; Stevanato, R., Enzyme Immobilization: An Update. *Journal of Chemical Biology* **2013**, *6*, 185-205.
47. Rivero, C. W.; De Benedetti, E. C.; Gallego, F. L.; Pessela, B. C.; Guisán, J. M.; Trelles, J. A., Biosynthesis of an Antiviral Compound Using a Stabilized Phosphopentomutase by Multipoint Covalent Immobilization. *J. Biotechnol.* **2017**, *249*, 34-41.
48. Purushottam, L.; Adusumalli, S. R.; Singh, U.; Unnikrishnan, V. B.; Rawale, D. G.; Gujrati, M., *et al.*, Single-Site Glycine-Specific Labeling of Proteins. *Nat. Commun.* **2019**, *10*, 2539.
49. Khoo, K. K.; Galleano, I.; Gasparri, F.; Wieneke, R.; Harms, H.; Poulsen, M. H., *et al.*, Chemical Modification of Proteins by Insertion of Synthetic Peptides Using Tandem Protein Trans-Splicing. *Nat. Commun.* **2020**, *11*, 2284.
50. Gilis, D.; Massar, S.; Cerf, N. J.; Rooman, M., Optimality of the Genetic Code with Respect to Protein Stability and Amino-Acid Frequencies. *Genome Biology* **2001**, *2*, 1-12.
51. Koniev, O.; Wagner, A., Developments and Recent Advancements in the Field of Endogenous Amino Acid Selective Bond Forming Reactions for Bioconjugation. *Chem. Soc. Rev.* **2015**, *44*, 5495-5551.
52. Li, Y.; Ogorzalek, T. L.; Wei, S.; Zhang, X.; Yang, P.; Jasensky, J., *et al.*, Effect of Immobilization Site on the Orientation and Activity of Surface-Tethered Enzymes. *Phys. Chem. Chem. Phys.* **2018**, *20*, 1021-1029.
53. Luckarift, H. R.; Spain, J. C.; Naik, R. R.; Stone, M. O., Enzyme Immobilization in a Biomimetic Silica Support. *Nat. Biotechnol.* **2004**, *22*, 211-213.

54. Naik, R. R.; Tomczak, M. M.; Luckarift, H. R.; Spain, J. C.; Stone, M. O., Entrapment of Enzymes and Nanoparticles Using Biomimetically Synthesized Silica. *Chem. Commun.* **2004**, *4*, 1684-1685.
55. Chen, S.-Y.; Lo, W.-S.; Huang, Y.-D.; Si, X.; Liao, F.-S.; Lin, S.-W., *et al.*, Probing Interactions between Metal–Organic Frameworks and Freestanding Enzymes in a Hollow Structure. *Nano Lett.* **2020**, *20*, 6630-6635.
56. Park, B.-W.; Yoon, D.-Y.; Kim, D.-S., Recent Progress in Bio-Sensing Techniques with Encapsulated Enzymes. *Biosens. Bioelectron.* **2010**, *26*, 1-10.
57. Pierre, A. C., The Sol-Gel Encapsulation of Enzymes. *Biocatal. Biotransform.* **2004**, *22*, 145-170.
58. Livage, J.; Coradin, T., Encapsulation of Enzymes, Antibodies, and Bacteria. In *Handbook of Sol-Gel Science and Technology*, Klein, L.; Aparicio, M.; Jitianu, A., Eds. Springer International Publishing: Cham, 2017; pp 1-23.
59. Chen, Q.; Kenausis, G. L.; Heller, A., Stability of Oxidases Immobilized in Silica Gels. *J. Am. Chem. Soc.* **1998**, *120*, 4582-4585.
60. Zhao, Z. Y.; Liu, J.; Hahn, M.; Qiao, S.; Middelberg, A. P. J.; He, L., Encapsulation of Lipase in Mesoporous Silica Yolk–Shell Spheres with Enhanced Enzyme Stability. *RSC. Adv.* **2013**, *3*, 22008-22013.
61. Kim, S.; Kwon, K.; Cha, J.; Yoo, S.; Han, M. S.; Tae, G., *et al.*, Pluronic-Based Nanocarrier Platform Encapsulating Two Enzymes for Cascade Reactions. *ACS Appl. Bio Mater.* **2020**, *3*, 5126-5135.
62. Skaalure, S. C.; Akalp, U.; Vernerey, F. J.; Bryant, S. J., Tuning Reaction and Diffusion Mediated Degradation of Enzyme-Sensitive Hydrogels. *Adv. Healthc. Mater.* **2016**, *5*, 432-438.
63. Sotiropoulou, S.; Chaniotakis, N. A., Tuning the Sol–Gel Microenvironment for Acetylcholinesterase Encapsulation. *Biomaterials* **2005**, *26*, 6771-6779.
64. Varlas, S.; Foster, J. C.; Georgiou, P. G.; Keogh, R.; Husband, J. T.; Williams, D. S., *et al.*, Tuning the Membrane Permeability of Polymersome Nanoreactors Developed by Aqueous Emulsion Polymerization-Induced Self-Assembly. *Nanoscale* **2019**, *11*, 12643-12654.
65. Jamtveit B., M. P., Growth, Dissolution and Pattern Formation in Geosystems. In: *Growth, Dissolution and Pattern Formation in Geosystems*. Springer: Dordrecht., 1999; p 291.
66. Dror, Y.; Kuhn, J.; Avrahami, R.; Zussman, E., Encapsulation of Enzymes in Biodegradable Tubular Structures. *Macromolecules* **2008**, *41*, 4187-4192.
67. Schachschal, S.; Adler, H.-J.; Pich, A.; Wetzels, S.; Matura, A.; van Pee, K.-H., Encapsulation of Enzymes in Microgels by Polymerization/Cross-Linking in Aqueous Droplets. *Colloid Polym. Sci.* **2011**, *289*, 693-698.
68. Cuomo, F.; Ceglie, A.; Leonardis, A. D.; Lopez, F., Polymer Capsules for Enzymatic Catalysis in Confined Environments. *Catalysts* **2018**, *9*, 1.
69. Bucatariu, F.; Simon, F.; Bellmann, C.; Fundueanu, G.; Dragan, E. S., Stability under Flow Conditions of Trypsin Immobilized onto Poly(Vinyl Amine) Functionalized Silica Microparticles. *Colloids Surf. A* **2012**, *399*, 71-77.
70. Hartmann, M., Ordered Mesoporous Materials for Bioadsorption and Biocatalysis. *Chem. Mater.* **2005**, *17*, 4577-4593.
71. You, C.-C.; De, M.; Han, G.; Rotello, V. M., Tunable Inhibition and Denaturation of A-Chymotrypsin with Amino Acid-Functionalized Gold Nanoparticles. *J. Am. Chem. Soc.* **2005**, *127*, 12873-12881.

72. Cunha, M. N. M.; Felgueiras, H. P.; Gouveia, I.; Zille, A., Synergistically Enhanced Stability of Laccase Immobilized on Synthesized Silver Nanoparticles with Water-Soluble Polymers. *Colloids Surf. B* **2017**, *154*, 210-220.
73. Petkova, G. A.; Záruba, K.; Žvátora, P.; Král, V., Gold and Silver Nanoparticles for Biomolecule Immobilization and Enzymatic Catalysis. *Nanoscale Res. Lett.* **2012**, *7*, 287.
74. Wei, Y.; Xu, J.; Feng, Q.; Dong, H.; Lin, M., Encapsulation of Enzymes in Mesoporous Host Materials Via the Nonsurfactant-Templated Sol–Gel Process. *Mater. Lett.* **2000**, *44*, 6-11.
75. Correro, M. R.; Moridi, N.; Schützinger, H.; Sykora, S.; Ammann, E. M.; Peters, E. H., *et al.*, Enzyme Shielding in an Enzyme-Thin and Soft Organosilica Layer. *Angew. Chem. Int. Ed.* **2016**, *55*, 6285-6289.
76. Correro, M. R.; Takacs, M.; Sykora, S.; Corvini, P. F. X.; Shahgaldian, P., Supramolecular Enzyme Engineering in Complex Nanometer-Thin Biomimetic Organosilica Layers. *RSC. Adv.* **2016**, *6*, 89966-89971.
77. Hwang, S. Y.; Kim, H. K.; Choo, J.; Seong, G. H.; Hien, T. B. D.; Lee, E. K., Effects of Operating Parameters on the Efficiency of Liposomal Encapsulation of Enzymes. *Colloids Surf. B* **2012**, *94*, 296-303.
78. Sanabria, J. C.; Muro Urista, C. R.; Ortega Aguilar, R. E.; Illescas, J.; Nava, M. d. C. D.; Carbajal Franco, G., Encapsulation of Active Fractions of Whey Proteins with Antioxidant Potential in Pectin-Collagen and Pectin-Gelatin Microparticles. *MRS Advances* **2018**, *3*, 3853-3860.
79. Feng, Q.; Hou, D.; Zhao, Y.; Xu, T.; Menkhous, T. J.; Fong, H., Electrospun Regenerated Cellulose Nanofibrous Membranes Surface-Grafted with Polymer Chains/Brushes Via the Atom Transfer Radical Polymerization Method for Catalase Immobilization. *ACS Appl. Mater. Interfaces* **2014**, *6*, 20958-20967.
80. Lee, E.-H.; Tsujimoto, T.; Uyama, H.; Sung, M.-H.; Kim, K.; Kuramitsu, S., Enhancement of Enzyme Activity and Stability by Poly(Γ -Glutamic Acid). *Polym. J.* **2010**, *42*, 818-822.
81. Hoarau, M.; Badiéyan, S.; Marsh, E. N. G., Immobilized Enzymes: Understanding Enzyme – Surface Interactions at the Molecular Level. *Org. Biomol. Chem.* **2017**, *15*, 9539-9551.
82. Zhao, D.; Peng, C.; Zhou, J., Lipase Adsorption on Different Nanomaterials: A Multi-Scale Simulation Study. *Phys. Chem. Chem. Phys.* **2015**, *17*, 840-850.
83. Orrego, A. H.; Ghobadi, R.; Moreno-Perez, S.; Mendoza, A. J.; Fernandez-Lorente, G.; Guisán, J. M., *et al.*, Stabilization of Immobilized Lipases by Intense Intramolecular Cross-Linking of Their Surfaces by Using Aldehyde-Dextran Polymers. *Int J Mol Sci* **2018**, *19*, 553.
84. Aubin-Tam, M.-E.; Hamad-Schifferli, K., Gold Nanoparticle–Cytochrome C Complexes: The Effect of Nanoparticle Ligand Charge on Protein Structure. *Langmuir* **2005**, *21*, 12080-12084.
85. Haupt, B.; Neumann, T.; Wittemann, A.; Ballauff, M., Activity of Enzymes Immobilized in Colloidal Spherical Polyelectrolyte Brushes. *Biomacromolecules* **2005**, *6*, 948-955.
86. Shang, W.; Nuffer, J. H.; Muñoz-Papandrea, V. A.; Colón, W.; Siegel, R. W.; Dordick, J. S., Cytochrome C on Silica Nanoparticles: Influence of Nanoparticle Size on Protein Structure, Stability, and Activity. *Small* **2009**, *5*, 470-476.
87. Talbert, J. N.; Goddard, J. M., Enzymes on Material Surfaces. *Colloids Surf. B* **2012**, *93*, 8-19.
88. Asuri, P.; Karajanagi, S. S.; Yang, H.; Yim, T.-J.; Kane, R. S.; Dordick, J. S., Increasing Protein Stability through Control of the Nanoscale Environment. *Langmuir* **2006**, *22*, 5833-5836.
89. Matsuno, H.; Nagasaka, Y.; Kurita, K.; Serizawa, T., Superior Activities of Enzymes Physically Immobilized on Structurally Regular Poly(Methyl Methacrylate) Surfaces. *Chem. Mater.* **2007**, *19*, 2174-2179.

90. Draghici, C.; Kowal, J.; Darjan, A.; Meier, W.; Palivan, C. G., "Active Surfaces" Formed by Immobilization of Enzymes on Solid-Supported Polymer Membranes. *Langmuir* **2014**, *30*, 11660-11669.
91. Zdarta, J.; Meyer, A.; Jesionowski, T.; Pinelo, M., A General Overview of Support Materials for Enzyme Immobilization: Characteristics, Properties, Practical Utility. *Catalysts* **2018**, *8*, 92.
92. Febriyanti, E.; Suendo, V.; Mukti, R. R.; Prasetyo, A.; Arifin, A. F.; Akbar, M. A., *et al.*, Further Insight into the Definite Morphology and Formation Mechanism of Mesoporous Silica Kcc-1. *Langmuir* **2016**, *32*, 5802-5811.
93. Stöber, W.; Fink, A.; Bohn, E., Controlled Growth of Monodisperse Silica Spheres in the Micron Size Range. *J. Colloid Interface Sci.* **1968**, *26*, 62-69.
94. Shimura, N.; Ogawa, M., Preparation of Surfactant Templated Nanoporous Silica Spherical Particles by the Stöber Method. Effect of Solvent Composition on the Particle Size. *J. Mater. Sci.* **2007**, *42*, 5299-5306.
95. Galliker, P.; Hommes, G.; Schlosser, D.; Corvini, P. F.; Shahgaldian, P., Laccase-Modified Silica Nanoparticles Efficiently Catalyze the Transformation of Phenolic Compounds. *J. Colloid Interface Sci.* **2010**, *349*, 98-105.
96. Möller, K.; Bein, T., Talented Mesoporous Silica Nanoparticles. *Chem. Mater.* **2017**, *29*, 371-388.
97. Li, D.; Zhu, Y.; Mao, C., One-Pot Synthesis of Surface Roughness Controlled Hollow Silica Spheres with Enhanced Drug Loading and Release Profiles under Ambient Conditions in Aqueous Solutions. *J. Mater. Chem. B* **2013**, *1*, 5515-5520.
98. Park, S. S.; Santha Moorthy, M.; Ha, C.-S., Periodic Mesoporous Organosilicas for Advanced Applications. *NPG Asia Materials* **2014**, *6*, e96-e96.
99. Wang, X.; Wang, H.; Tang, J.; Wang, S.; Shi, D.; Shen, H., Poly(Amino Acid) Multilayers Modified Dendritic Mesoporous Silica Nanoparticles Achieve Effective Enzyme Stability for Ultrasensitive Immunoassay. *ACS Appl. Mater. Interfaces* **2020**, *12*, 37906-37913.
100. Begum, G.; Swathi, P.; Bandarapu, A. K.; Nayak, J.; Rana, R. K., Spatial Confinement of Enzyme and Nanozyme in Silica-Based Hollow Microreactors. *ACS Appl. Mater. Interfaces* **2020**, *12*, 45476-45484.
101. Muñoz-Pina, S.; Ros-Lis, J. V.; Argüelles, Á.; Martínez-Máñez, R.; Andrés, A., Influence of the Functionalisation of Mesoporous Silica Material Uvm-7 on Polyphenol Oxidase Enzyme Capture and Enzymatic Browning. *Food Chem.* **2020**, *310*, 125741.
102. Jo, S.-M.; Wurm, F. R.; Landfester, K., Biomimetic Cascade Network between Interactive Multicompartmental Organized by Enzyme-Loaded Silica Nanoreactors. *ACS Appl. Mater. Interfaces* **2018**, *10*, 34230-34237.
103. Scodeller, P.; Catalano, P. N.; Salguero, N.; Duran, H.; Wolosiuk, A.; Soler-Illia, G. J. A. A., Hyaluronan Degrading Silica Nanoparticles for Skin Cancer Therapy. *Nanoscale* **2013**, *5*, 9690-9698.
104. Mirzaie, A.; Saadati, A.; Hassanpour, S.; Hasanzadeh, M.; Siahi-Shadbad, M.; Jouyban, A., Determination of Proline in Human Plasma Samples Using the Encapsulation of Proline Dehydrogenase Enzyme in Dendritic Silica: A New Platform for the Enzymatic Biosensing of Amino Acids. *Anal. Methods* **2019**, *11*, 4609-4619.
105. Li, M.; Cheng, F.; Xue, C.; Wang, H.; Chen, C.; Du, Q., *et al.*, Surface Modification of Stöber Silica Nanoparticles with Controlled Moiety Densities Determines Their Cytotoxicity Profiles in Macrophages. *Langmuir* **2019**, *35*, 14688-14695.

106. Tarn, D.; Ashley, C. E.; Xue, M.; Carnes, E. C.; Zink, J. I.; Brinker, C. J., Mesoporous Silica Nanoparticle Nanocarriers: Biofunctionality and Biocompatibility. *Acc. Chem. Res.* **2013**, *46*, 792-801.
107. Kim, I.-Y.; Joachim, E.; Choi, H.; Kim, K., Toxicity of Silica Nanoparticles Depends on Size, Dose, and Cell Type. *Nanomedicine* **2015**, *11*, 1407-1416.
108. Breznan, D.; Das, D. D.; MacKinnon-Roy, C.; Bernatchez, S.; Sayari, A.; Hill, M., *et al.*, Physicochemical Properties Can Be Key Determinants of Mesoporous Silica Nanoparticle Potency in Vitro. *ACS Nano* **2018**, *12*, 12062-12079.
109. Murugadoss, S.; Lison, D.; Godderis, L.; Van Den Brule, S.; Mast, J.; Brassinne, F., *et al.*, Toxicology of Silica Nanoparticles: An Update. *Arch. Toxicol.* **2017**, *91*, 2967-3010.
110. K uchler, A.; Yoshimoto, M.; Luginb uhl, S.; Mavelli, F.; Walde, P., Enzymatic Reactions in Confined Environments. *Nat. Nanotechnol.* **2016**, *11*, 409-420.
111. GM., C., The Central Role of Enzymes as Biological Catalysts. In *The Cell: A Molecular Approach* (2nd Edition). Sunderland (MA), 2000.
112. Bolivar, J. M.; Nidetzky, B., The Microenvironment in Immobilized Enzymes: Methods of Characterization and Its Role in Determining Enzyme Performance. *Molecules* **2019**, *24*.
113. Bru, R.; S anchez-Ferrer, A.; Garc ıa-Carmona, F., The Effect of Substrate Partitioning on the Kinetics of Enzymes Acting in Reverse Micelles. *BIJOAK* **1990**, *268*, 679-84.
114. Goldhahn, C.; Taut, J. A.; Schubert, M.; Burgert, I.; Chanana, M., Enzyme Immobilization inside the Porous Wood Structure: A Natural Scaffold for Continuous-Flow Biocatalysis. *RSC. Adv.* **2020**, *10*, 20608-20619.
115. You, C.-C.; Agasti, S. S.; De, M.; Knapp, M. J.; Rotello, V. M., Modulation of the Catalytic Behavior of A-Chymotrypsin at Monolayer-Protected Nanoparticle Surfaces. *J. Am. Chem. Soc.* **2006**, *128*, 14612-14618.
116. Rodrigues, R. C.; Ortiz, C.; Berenguer-Murcia,  . A.; Torres, R.; Fern andez-Lafuente, R., Modifying Enzyme Activity and Selectivity by Immobilization. *Chem. Soc. Rev.* **2013**, *42*, 6290-6307.
117. Illanes, A., Heterogeneous Enzyme Kinetic. In *Enzyme Biocatalysis: Principles and Applications* (First edition). Springer Netherlands: Dordrecht, 2008; pp 155-203.
118. Kawakami, K., Enhancement of Thermostability of Lipase by the Sol-Gel Entrapment into Methyl-Substituted Organic Silicates Formed on Diatomaceous Earth. *Biotechnol. Tech.* **1996**, *10*, 491-494.
119. Briand, M. L.; Gebleux, R.; Richina, F.; Corroero, M. R.; Grether, Y.; Dudal, Y., *et al.*, Partially Shielded Enzymes Capable of Processing Large Protein Substrates. *Chem. Commun.* **2020**, *56*, 5170-5173.
120. Reetz, M. T.; Zonta, A.; Simpelkamp, J., Efficient Immobilization of Lipases by Entrapment in Hydrophobic Sol-Gel Materials. *Biotechnol. Bioeng.* **1996**, *49*, 527-34.
121. Corroero, M. R.; Moridi, N.; Schutzingler, H.; Sykora, S.; Ammann, E. M.; Peters, E. H., *et al.*, Enzyme Shielding in an Enzyme-Thin and Soft Organosilica Layer. *Angew. Chem. Int. Ed.* **2016**, *55*, 6285-6289.
122. Devamani, T.; Rauwerdink, A. M.; Lunzer, M.; Jones, B. J.; Mooney, J. L.; Tan, M. A., *et al.*, Catalytic Promiscuity of Ancestral Esterases and Hydroxynitrile Lyases. *J. Am. Chem. Soc.* **2016**, *138*, 1046-56.
123. O'Brien, P. J.; Herschlag, D., Catalytic Promiscuity and the Evolution of New Enzymatic Activities. *Chem. Biol.* **1999**, *6*, R91-R105.

124. Copley, S. D., Shining a Light on Enzyme Promiscuity. *Curr. Opin. Struct. Biol.* **2017**, *47*, 167-175.
125. Jackson, C. J.; Foo, J.-L.; Kim, H.-K.; Carr, P. D.; Liu, J.-W.; Salem, G., *et al.*, In Crystallo Capture of a Michaelis Complex and Product-Binding Modes of a Bacterial Phosphotriesterase. *J. Mol. Biol.* **2008**, *375*, 1189-1196.
126. Honaker, M. T.; Acchione, M.; Sumida, J. P.; Atkins, W. M., Ensemble Perspective for Catalytic Promiscuity: Calorimetric Analysis of the Active Site Conformational Landscape of a Detoxification Enzyme. *J. Biol. Chem.* **2011**, *286*, 42770-6.
127. Yoshikuni, Y.; Ferrin, T. E.; Keasling, J. D., Designed Divergent Evolution of Enzyme Function. *Nature* **2006**, *440*, 1078-1082.
128. Martinez-Martinez, M.; Coscolin, C.; Santiago, G.; Chow, J.; Stogios, P. J.; Bargiela, R., *et al.*, Determinants and Prediction of Esterase Substrate Promiscuity Patterns. *ACS Chem. Biol.* **2018**, *13*, 225-234.
129. van Loo, B.; Jonas, S.; Babtie, A. C.; Benjdia, A.; Berteau, O.; Hyvonen, M., *et al.*, An Efficient, Multiply Promiscuous Hydrolase in the Alkaline Phosphatase Superfamily. *Proc. Natl. Acad. Sci. U.S.A.* **2010**, *107*, 2740-2745.
130. Albanese, D. C. M.; Gaggero, N., Albumin as a Promiscuous Biocatalyst in Organic Synthesis. *RSC Adv.* **2015**, *5*, 10588-10598.
131. Babtie, A.; Tokuriki, N.; Hollfelder, F., What Makes an Enzyme Promiscuous? *Curr. Opin. Chem. Biol.* **2010**, *14*, 200-207.
132. Lutz, S.; Lichter, J.; Liu, L., Exploiting Temperature-Dependent Substrate Promiscuity for Nucleoside Analogue Activation by Thymidine Kinase from *Thermotoga Maritima*. *J. Am. Chem. Soc.* **2007**, *129*, 8714-8715.
133. Khersonsky, O.; Tawfik, D. S., Enzyme Promiscuity: A Mechanistic and Evolutionary Perspective. *Ann. Rev. Biochem.* **2010**, *79*, 471-505.
134. Pandya, C.; Farelli, J. D.; Dunaway-Mariano, D.; Allen, K. N., Enzyme Promiscuity: Engine of Evolutionary Innovation. *J. Biol. Chem.* **2014**, *289*, 30229-30236.
135. Leveson-Gower, R. B.; Mayer, C.; Roelfes, G., The Importance of Catalytic Promiscuity for Enzyme Design and Evolution. *Nat. Rev. Chem.* **2019**, *3*, 687-705.
136. Brustad, E. M.; Arnold, F. H., Optimizing Non-Natural Protein Function with Directed Evolution. *Curr. Opin. Chem. Biol.* **2011**, *15*, 201-10.
137. Frushicheva, M. P.; Cao, J.; Chu, Z. T.; Warshel, A., Exploring Challenges in Rational Enzyme Design by Simulating the Catalysis in Artificial Kemp Eliminase. *Proc. Natl. Acad. Sci. U.S.A.* **2010**, *107*, 16869-74.
138. Packer, M. S.; Liu, D. R., Methods for the Directed Evolution of Proteins. *Nat. Rev. Genet.* **2015**, *16*, 379-94.
139. Zeymer, C., Directed Evolution of Selective Enzymes: Catalysts for Organic Chemistry and Biotechnology. By Manfred T. Reetz. *ChemBioChem* **2019**, *20*, 415-416.
140. van der Meer, J. Y.; Poddar, H.; Baas, B. J.; Miao, Y. F.; Rahimi, M.; Kunzendorf, A., *et al.*, Using Mutability Landscapes of a Promiscuous Tautomerase to Guide the Engineering of Enantioselective Michaelases. *Nat. Commun.* **2016**, *7*, 10911.
141. Xu, J. K.; Wang, C. L.; Cong, Z. Q., Strategies for Substrate-Regulated P450 Catalysis: From Substrate Engineering to Co-Catalysis. *Chem. Eur. J.* **2019**, *25*, 6853-6863.

142. Dietrich, J. A.; Yoshikuni, Y.; Fisher, K. J.; Woolard, F. X.; Ockey, D.; McPhee, D. J., *et al.*, A Novel Semi-Biosynthetic Route for Artemisinin Production Using Engineered Substrate-Promiscuous P450(Bm3). *ACS Chem. Biol.* **2009**, *4*, 261-267.
143. Nobili, A.; Tao, Y. F.; Pavlidis, I. V.; van den Bergh, T.; Joosten, H. J.; Tan, T. W., *et al.*, Simultaneous Use of in Silico Design and a Correlated Mutation Network as a Tool to Efficiently Guide Enzyme Engineering. *ChemBioChem* **2015**, *16*, 805-810.
144. Alonso, S.; Santiago, G.; Cea-Rama, I.; Fernandez-Lopez, L.; Coscolín, C.; Modregger, J., *et al.*, Genetically Engineered Proteins with Two Active Sites for Enhanced Biocatalysis and Synergistic Chemo- and Biocatalysis. *Nat. Catal.* **2019**, *3*, 319-328.
145. Lancaster, L.; Abdallah, W.; Banta, S.; Wheeldon, I., Engineering Enzyme Microenvironments for Enhanced Biocatalysis. *Chem. Soc. Rev.* **2018**, *47*, 5177-5186.
146. Emond, S.; Guieysse, D.; Lechevallier, S.; Dexpert-Ghys, J.; Monsan, P.; Remaud-Siméon, M., Alteration of Enzyme Activity and Enantioselectivity by Biomimetic Encapsulation in Silica Particles. *Chem. Commun.* **2012**, *48*, 1314-1316.
147. Jurcik, A.; Bednar, D.; Byska, J.; Marques, S. M.; Furmanova, K.; Daniel, L., *et al.*, Caver Analyst 2.0: Analysis and Visualization of Channels and Tunnels in Protein Structures and Molecular Dynamics Trajectories. *Bioinformatics* **2018**, *34*, 3586-3588.
148. Millard, C. B.; Kryger, G.; Ordentlich, A.; Greenblatt, H. M.; Harel, M.; Raves, M. L., *et al.*, Crystal Structures of Aged Phosphonylated Acetylcholinesterase: Nerve Agent Reaction Products at the Atomic Level. *Biochemistry* **1999**, *38*, 7032-7039.
149. Gober, J. G.; Rydeen, A. E.; Gibson-O'Grady, E. J.; Leuthaeuser, J. B.; Fetrow, J. S.; Brustad, E. M., Mutating a Highly Conserved Residue in Diverse Cytochrome P450s Facilitates Diastereoselective Olefin Cyclopropanation. *ChemBioChem* **2016**, *17*, 394-397.
150. Nath, A.; Atkins, W. M., A Quantitative Index of Substrate Promiscuity. *Biochemistry* **2008**, *47*, 157-166.
151. Chaubey, A.; Parshad, R.; Koul, S.; Taneja, S. C.; Qazi, G. N., Enantioselectivity Modulation through Immobilization of *Arthrobacter* Sp Lipase: Kinetic Resolution of Fluoxetine Intermediate. *J. Mol. Catal.* **2006**, *42*, 39-44.
152. Fernández-Lorente, G.; Terreni, M.; Mateo, C.; Bastida, A.; Fernández-Lafuente, R.; Dalmases, P., *et al.*, Modulation of Lipase Properties in Macro-Aqueous Systems by Controlled Enzyme Immobilization: Enantioselective Hydrolysis of a Chiral Ester by Immobilized *Pseudomonas* Lipase. *Enzyme Microb. Technol.* **2001**, *28*, 389-396.
153. Rocchietti, S.; Urrutia, A.; Pregnotato, M.; Tagliani, A.; Guisan, J.; Fernández-Lafuente, R., *et al.*, Influence of the Derivative Preparation and Substrate Structure on the Enantioselectivity of Penicillin G Acylase. *Enzyme Microb. Technol.* **2002**, *31*, 88-93.
154. Mangiagalli, M.; Brocca, S.; Orlando, M.; Lotti, M., The "Cold Revolution". Present and Future Applications of Cold-Active Enzymes and Ice-Binding Proteins. *New Biotechnol.* **2020**, *55*, 5-11.
155. Santiago, M.; Ramírez-Sarmiento, C. A.; Zamora, R. A.; Parra, L. P., Discovery, Molecular Mechanisms, and Industrial Applications of Cold-Active Enzymes. *Front. Microb.* **2016**, *7*, 1408-1408.
156. Al-Ghanayem, A. A.; Joseph, B., Current Prospective in Using Cold-Active Enzymes as Eco-Friendly Detergent Additive. *Appl. Microbiol. Biotechnol.* **2020**, *104*, 2871-2882.
157. Joseph, B.; Shrivastava, N.; Ramteke, P. W., Extracellular Cold-Active Lipase of *Microbacterium Luteolum* Isolated from Gangotri Glacier, Western Himalaya: Isolation, Partial Purification and Characterization. *J Genet Eng Biotechnol* **2012**, *10*, 137-144.

158. Sočan, J.; Isaksen, G. V.; Brandsdal, B. O.; Åqvist, J., Towards Rational Computational Engineering of Psychrophilic Enzymes. *Sci. Rep.* **2019**, *9*, 19147.
159. Khan, M.; Sathya, T. A., Extremozymes from Metagenome: Potential Applications in Food Processing. *Crit. Rev. Food Sci.* **2018**, *58*, 2017-2025.
160. Marx, J. C.; Blaise, V.; Collins, T.; D'Amico, S.; Delille, D.; Gratia, E., *et al.*, A Perspective on Cold Enzymes: Current Knowledge and Frequently Asked Questions. *Cell Mol Biol* **2004**, *50*, 643-55.
161. Struvay, C.; Feller, G., Optimization to Low Temperature Activity in Psychrophilic Enzymes. *Int J Mol Sci* **2012**, *13*, 11643-11665.
162. Roulling, F.; Piette, F.; Cipolla, A.; Struvay, C.; Feller, G., Psychrophilic Enzymes: Cool Responses to Chilly Problems. In *Extremophiles Handbook*, Horikoshi, K., Ed. Springer Japan: Tokyo, 2011; pp 891-913.
163. Faraday, M., X. The Bakerian Lecture. Experimental Relations of Gold (and Other Metals) to Light. *Philos. Trans. R. Soc. B* **1857**, *147*, 145-181.
164. Brongersma, M. L.; Halas, N. J.; Nordlander, P., Plasmon-Induced Hot Carrier Science and Technology. *Nat. Nanotechnol.* **2015**, *10*, 25-34.
165. Carattino, A.; Caldarola, M.; Orrit, M., Gold Nanoparticles as Absolute Nanothermometers. *Nano Lett.* **2018**, *18*, 874-880.
166. Kimling, J.; Maier, M.; Okenve, B.; Kotaidis, V.; Ballot, H.; Plech, A., Turkevich Method for Gold Nanoparticle Synthesis Revisited. *J. Phys. Chem. B* **2006**, *110*, 15700-15707.
167. Turkevich, J., Colloidal Gold. Part Ii. *Gold Bull.* **1985**, *18*, 125-131.
168. Daruich De Souza, C.; Ribeiro Nogueira, B.; Rostelato, M. E. C. M., Review of the Methodologies Used in the Synthesis Gold Nanoparticles by Chemical Reduction. *J. Alloys Compd.* **2019**, *798*, 714-740.
169. Barnes, W. L.; Dereux, A.; Ebbesen, T. W., Surface Plasmon Subwavelength Optics. *Nature* **2003**, *424*, 824-830.
170. Boselli, L.; Lopez, H.; Zhang, W.; Cai, Q.; Giannone, V. A.; Li, J., *et al.*, Classification and Biological Identity of Complex Nano Shapes. *Comm. Mater.* **2020**, *1*, 35.
171. Jans, H.; Huo, Q., Gold Nanoparticle-Enabled Biological and Chemical Detection and Analysis. *Chem. Soc. Rev.* **2012**, *41*, 2849-2866.
172. Huang, X.; El-Sayed, M. A., Gold Nanoparticles: Optical Properties and Implementations in Cancer Diagnosis and Photothermal Therapy. *J. Adv. Res.* **2010**, *1*, 13-28.
173. Hinman, J. G.; Stork, A. J.; Varnell, J. A.; Gewirth, A. A.; Murphy, C. J., Seed Mediated Growth of Gold Nanorods: Towards Nanorod Matryoshkas. *Faraday Discuss.* **2016**, *191*, 9-33.
174. Zijlstra, P.; Paulo, P. M. R.; Yu, K.; Xu, Q.-H.; Orrit, M., Chemical Interface Damping in Single Gold Nanorods and Its near Elimination by Tip-Specific Functionalization. *Angew. Chem. Int. Ed.* **2012**, *51*, 8352-8355.
175. Richardson, H. H.; Carlson, M. T.; Tandler, P. J.; Hernandez, P.; Govorov, A. O., Experimental and Theoretical Studies of Light-to-Heat Conversion and Collective Heating Effects in Metal Nanoparticle Solutions. *Nano Lett.* **2009**, *9*, 1139-1146.
176. Richardson, H. H.; Hickman, Z. N.; Govorov, A. O.; Thomas, A. C.; Zhang, W.; Kordesch, M. E., Thermo-optical Properties of Gold Nanoparticles Embedded in Ice: Characterization of Heat Generation and Melting. *Nano Lett.* **2006**, *6*, 783-788.

177. Kim, M.; Lee, J.-H.; Nam, J.-M., Plasmonic Photothermal Nanoparticles for Biomedical Applications. *Adv Sci* **2019**, *6*, 1900471.
178. Liu, F.; Wang, L.; Wang, H.; Yuan, L.; Li, J.; Brash, J. L., *et al.*, Modulating the Activity of Protein Conjugated to Gold Nanoparticles by Site-Directed Orientation and Surface Density of Bound Protein. *ACS Appl. Mater. Interfaces* **2015**, *7*, 3717-3724.
179. Hondred, J. A.; Breger, J. C.; Garland, N. T.; Oh, E.; Susumu, K.; Walper, S. A., *et al.*, Enhanced Enzymatic Activity from Phosphotriesterase Trimer Gold Nanoparticle Bioconjugates for Pesticide Detection. *Analyst* **2017**, *142*, 3261-3271.
180. Wang, Y.; van Asdonk, K.; Zijlstra, P., A Robust and General Approach to Quantitatively Conjugate Enzymes to Plasmonic Nanoparticles. *Langmuir* **2019**, *35*, 13356-13363.
181. Breger, J. C.; Oh, E.; Susumu, K.; Klein, W. P.; Walper, S. A.; Ancona, M. G., *et al.*, Nanoparticle Size Influences Localized Enzymatic Enhancement—a Case Study with Phosphotriesterase. *Bioconjugate Chem.* **2019**, *30*, 2060-2074.
182. Yu, S.; Wilson, A. J.; Heo, J.; Jain, P. K., Plasmonic Control of Multi-Electron Transfer and C-C Coupling in Visible-Light-Driven CO₂ Reduction on Au Nanoparticles. *Nano Lett.* **2018**, *18*, 2189-2194.
183. Tadepalli, S.; Yim, J.; Madireddi, K.; Luang, J. Y.; Naik, R. R.; Singamaneni, S., Gold Nanorod-Mediated Photothermal Enhancement of the Biocatalytic Activity of a Polymer-Encapsulated Enzyme. *Chem. Mater.* **2017**, *29*, 6308-6314.
184. Tadepalli, S.; Yim, J.; Cao, S.; Wang, Z.; Naik, R. R.; Singamaneni, S., Metal–Organic Framework Encapsulation for the Preservation and Photothermal Enhancement of Enzyme Activity. *Small* **2018**, *14*, 1702382.
185. Bokhimi, X.; Zanella, R.; Morales, A., Au/Rutile Catalysts: Effect of Support Dimensions on the Gold Crystallite Size and the Catalytic Activity for CO Oxidation. *J. Phys. Chem. C* **2007**, *111*, 15210-15216.
186. Ishida, T.; Kinoshita, N.; Okatsu, H.; Akita, T.; Takei, T.; Haruta, M., Influence of the Support and the Size of Gold Clusters on Catalytic Activity for Glucose Oxidation. *Angew. Chem. Int. Ed.* **2008**, *47*, 9265-9268.
187. Naya, S.; Teranishi, M.; Kimura, K.; Tada, H., A Strong Support-Effect on the Catalytic Activity of Gold Nanoparticles for Hydrogen Peroxide Decomposition. *Chem. Commun.* **2011**, *47*, 3230-3232.
188. Soares, J. M. C.; Morrall, P.; Crossley, A.; Harris, P.; Bowker, M., Catalytic and Noncatalytic CO Oxidation on Au/TiO₂ Catalysts. *J. Catal.* **2003**, *219*, 17-24.
189. Guzzi, L.; Beck, A.; Frey, K., Role of Promoting Oxide Morphology Dictating the Activity of Au/SiO₂ Catalyst in CO Oxidation. *Gold Bull.* **2009**, *42*, 5-12.
190. Lakshmanan, P.; Upare, P.; Le, N.-T.; Lee, K. Y.; Hwang, D.; Lee, U. H., *et al.*, Facile Synthesis of CeO₂-Supported Gold Nanoparticle Catalysts for Selective Oxidation of Glycerol into Lactic Acid. *Appl. Catal. A* **2013**, *468*, 260-268.
191. Lu, J.; Aydin, C.; Browning, N. D.; Gates, B. C., Imaging Isolated Gold Atom Catalytic Sites in Zeolite NaY. *Angew. Chem. Int. Ed.* **2012**, *51*, 5842-5846.
192. Chen, H. M.; Chen, C. K.; Chen, C. J.; Cheng, L. C.; Wu, P. C.; Cheng, B. H., *et al.*, Plasmon Inducing Effects for Enhanced Photoelectrochemical Water Splitting: X-Ray Absorption Approach to Electronic Structures. *ACS Nano* **2012**, *6*, 7362-7372.
193. Dong, Y. Y.; Su, Y. L.; Du, L. L.; Wang, R. F.; Zhang, L.; Zhao, D. B., *et al.*, Plasmon-Enhanced Deuteration under Visible-Light Irradiation. *ACS Nano* **2019**, *13*, 10754-10760.

194. Brusatin, G.; Della Giustina, G., Hybrid Organic–Inorganic Sol–Gel Materials for Micro and Nanofabrication. *J. Sol-Gel Sci. Technol.* **2011**, *60*, 299-314.
195. Pereira-Rodríguez, Á.; Fernández-Leiro, R.; González-Siso, M. I.; Cerdán, M. E.; Becerra, M.; Sanz-Aparicio, J., Structural Basis of Specificity in Tetrameric *Kluyveromyces Lactis* B-Galactosidase. *J. Struct. Biol.* **2012**, *177*, 392-401.
196. Uppenberg, J.; Hansen, M. T.; Patkar, S.; Jones, T. A., The Sequence, Crystal Structure Determination and Refinement of Two Crystal Forms of Lipase B from *Candida Antarctica*. *Structure* **1994**, *2*, 293-308.
197. Basso, A.; Serban, S., Industrial Applications of Immobilized Enzymes—a Review. *Molecular Catalysis* **2019**, *479*, 110607.
198. Splechtna, B.; Nguyen, T. H.; Zehetner, R.; Lettner, H. P.; Lorenz, W.; Haltrich, D., Process Development for the Production of Prebiotic Galacto-Oligosaccharides from Lactose Using Beta-Galactosidase from *Lactobacillus* Sp. *Biotechnol. J.* **2007**, *2*, 480-5.
199. Asadzadeh-Firouzabadi, A.; Zare, H. R., Application of Cysteamine-Capped Gold Nanoparticles for Early Detection of Lung Cancer-Specific Mirna (Mir-25) in Human Blood Plasma. *Analytical Methods* **2017**, *9*, 3852-3861.
200. Cappellari, P. S.; Buceta, D.; Morales, G. M.; Barbero, C. A.; Sergio Moreno, M.; Giovanetti, L. J., *et al.*, Synthesis of Ultra-Small Cysteine-Capped Gold Nanoparticles by Ph Switching of the Au(I)–Cysteine Polymer. *J. Colloid Interface Sci.* **2015**, *441*, 17-24.
201. Hayichelaeh, C.; Reuvekamp, L. A. E. M.; Dierkes, W. K.; Blume, A.; Noordermeer, J. W. M.; Sahakaro, K., Enhancing the Silanization Reaction of the Silica-Silane System by Different Amines in Model and Practical Silica-Filled Natural Rubber Compounds. *Polymers* **2018**, *10*, 584.
202. Zhang, H.; Gu, W.; Li, M. J.; Fang, W. Z.; Li, Z. Y.; Tao, W. Q., Influence of Environmental Factors on the Adsorption Capacity and Thermal Conductivity of Silica Nano-Porous Materials. *J. Nanosci. Nanotechnol.* **2015**, *15*, 3048-3054.
203. Howard, T. V.; Berry, K. R.; Roper, D. K., Initial Dynamic Thermal Dissipation Modes Enhance Heat Dissipation in Gold Nanoparticle–Polydimethylsiloxane Thin Films. *J. Therm. Anal. Calorim.* **2020**.
204. Jurado, E.; Camacho, F.; Luzón, G.; Vicaria, J. M., Kinetic Models of Activity for B-Galactosidases: Influence of Ph, Ionic Concentration and Temperature. *Enzyme Microb. Technol.* **2004**, *34*, 33-40.
205. Cumbo, A.; Lorber, B.; Corvini, P. F. X.; Meier, W.; Shahgaldian, P., A Synthetic Nanomaterial for Virus Recognition Produced by Surface Imprinting. *Nat. Commun.* **2013**, *4*.
206. Emsley, P.; Lohkamp, B.; Scott, W. G.; Cowtan, K., Features and Development of Coot. *Acta Cryst.* **2010**, *66*, 486-501.
207. Evans, P. R.; Murshudov, G. N., How Good Are My Data and What Is the Resolution? *Acta Cryst.* **2013**, *69*, 1204-1214.
208. Vagin, A.; Teplyakov, A., Molrep: An Automated Program for Molecular Replacement. *J. Appl. Crystallogr.* **1997**, *30*, 1022-1025.
209. Murshudov, G. N.; Vagin, A. A.; Dodson, E. J., Refinement of Macromolecular Structures by the Maximum-Likelihood Method. *Acta Cryst.* **1997**, *53*, 240-255.
210. Moriarty, N. W.; Grosse-Kunstleve, R. W.; Adams, P. D., Electronic Ligand Builder and Optimization Workbench (Elbow): A Tool for Ligand Coordinate and Restraint Generation. *Acta Cryst.* **2009**, *65*, 1074-1080.

211. Adams, P. D.; Afonine, P. V.; Bunkoczi, G.; Chen, V. B.; Davis, I. W.; Echols, N., *et al.*, Phenix: A Comprehensive Python-Based System for Macromolecular Structure Solution. *Acta Cryst.* **2010**, *66*, 213-221.
212. Burnley, B. T.; Afonine, P. V.; Adams, P. D.; Gros, P., Modelling Dynamics in Protein Crystal Structures by Ensemble Refinement. *elife* **2012**, *1*, 00311.